Title	Study on the Stability of Filter Units Armouring Rubble Mound under Wave Action
Author(s)	Mon, Aye Nyein
Citation	大阪大学, 2022, 博士論文
Version Type	VoR
URL	https://doi.org/10.18910/89632
rights	
Note	

Doctoral Dissertation

Study on the Stability of Filter Units Armouring Rubble Mound under Wave Action

AYE NYEIN MON

June 2022

Graduate School of Engineering,

Osaka University

Abstract

Natural rocks (armourstones) or artificial concrete armour units are usually used to provide protection of rubble mound breakwaters against wave action in coastal area. However, as the armourstones of sufficient size or quality are not readily available from nearby quarries and the concrete armour units are very expensive to fabricate and to install, the need for cost-effective, environmentally-friendly and protective armour unit type is an issue in the design of rubble mound breakwaters. Thus, researchers are keenly interested in finding alternatives to breakwater armour units.

Recently, filter units, fiber mesh bags of small stones, originally used in river protection works, have been proposed to apply in coastal area as well because of their high flexibility and porosity in comparison to armourstones, and these units have already been recognized as alternatives to subsea protection structures such as rock dumping and concrete mattresses. Moreover, a number of researches have already been carried out experimentally to study and improve the filter units' stability on rubble mound under various sea states. In this research not only experimental but also numerical investigations have been conducted focusing on damage mechanism of the filter units.

The thesis consists of five chapters. Chapter 1 concerns the background issues of conventional armour units of rubble mound breakwaters. Along with that, the armour units' stability and damage criteria adopted to the study of hydraulic model experiments are generally presented. Afterwards, the filter unit which is aimed at applying in the outer layer of rubble mound breakwaters is introduced including its previous studies. At the end research approach is presented.

Chapter 2 is allocated to explain the theoretical aspects applied in the research. Firstly, the hydraulic stability formula, widely used to approximate the required mass of armour unit, is described. Next, a numerical wave flume model (CADMAS-SURF/2D) is described which includes the governing equations, discretization methods, and model settings as well as selection of applicable wave theory and wave spectrum. Then, typical DEM (Discrete Element Method) commonly used in estimation of rubble mound structure deformation by waves and BPM (Bonded Particle Model), in which a bond model is added to the typical DEM, are explained. Finally, DEM calculation procedure within one-time step for simulation is described.

In chapter 3, two kinds of laboratory experiments performed to study hydraulic stability of filter units from the structure viewpoint are explained. In the first one, various models changing dimensions such as fiber bag size were tested individually on a flat surface of rubble mound under regular waves in order to compare their stability. In the latter experiment, filter unit models, belonging to the most stable structure in the first experiment, were tested on slope of rubble mound under irregular waves, and their movement and damage behaviors were analyzed with stability number estimation.

In chapter 4, two-dimensional numerical models simulated to reproduce flexible deformation of filter units on rubble mound under wave motion by coupling of two models: CADMAS-SURF and DEM are presented with a discussion based on some experimental results. In order to reproduce experimental models well, input parameters for simulation need to be calibrated effectively because the parameters have significant influence on simulated results. In the study, the parameters were determined based on relevant previous researches and some material properties available. In general, regardless of some imperfections, the presented models were found capable of modeling filter unit deformation on rubble mound due to waves. The main weak points of the models are the modeling with uniform size and shape particles and the less consideration of fluid-structure interaction.

In chapter 5, the conclusions of the experimental and numerical works shown in chapter 3 and chapter 4 are summarized, and some remarks on future research are added.

Acknowledgement

AYE NYEIN MON

Osaka, June 2022

Table of Contents

List of Figures

List of Tables

CHAPTER 1

Chapter 1

INTRODUCTION

OUTLINE

This chapter consists of four main sections. First of all, the background issues of conventional armour units of rubble mound breakwaters are discussed, which are followed by the overview of armour layer stability and damage estimation used in laboratory experiments. Then, filter unit (FU) is introduced as well as its previous studies, and present study approach is explained.

1.1 BACKGROUND

Rubble mound breakwaters covered by rock or concrete armour units, with or without wave wall superstructures, are one of the coastal engineering structures mostly used in coastal defense schemes. These structures are efficient at reducing wave action through the reflection and dissipation of incoming wave energy. Simply, it is a pile of stones (homogeneous structure) large enough to withstand ocean waves, more or less sorting in accord with their own weight. However, large stones are expensive and it is difficult to obtain large stones in a sufficient quantity because quarries yield mostly finer material (quarry run) and relatively small amount of large stones.

Hence, rubble mound breakwaters conventionally include finer material (locally available material: stone or sand) in the core and larger stones (or artificial concrete blocks) as an armour layer on the sea side to provide protection of the structure against wave forces, and to keep the finer material underneath, one or more filter layers (under-layers) are provided between the core and armour layer, then a toe berm is usually built on the sea side to provide stability of the slope. Figure 1.1 shows the cross-section of conventional-type rubble mound breakwater without superstructure. (CEM, 2002)

CONVENTIONAL MULTI LAYER RUBBLE-MOUND BREAKWATER
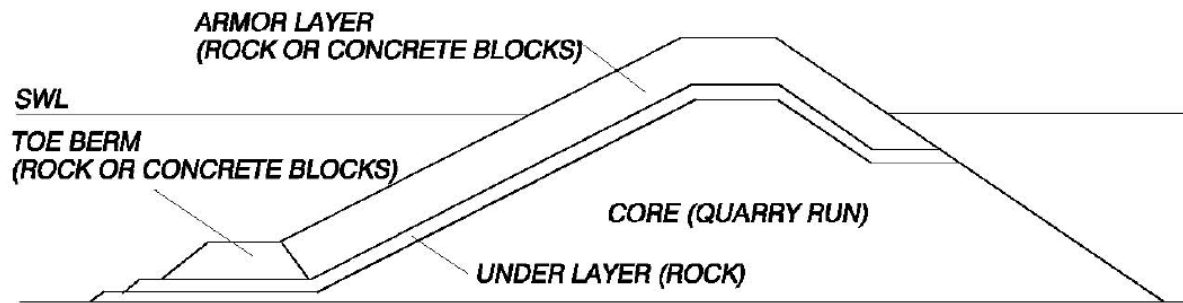
Figure 1. 1 Conventional type of rubble-mound breakwater (CEM, 2002)

Many failure modes that can reduce the structural performance and functionality of rubble mound breakwater below the minimum level expected by design were introduced by Burcharth (1993) (Figure 1.2). Among them, hydraulic instability of armour units is one of the most critical modes, in which generally the armour units around the sea water level are displaced first due to waves and subsequently under-layer and core become exposed to wave action and then extracted (eroded). Figure 1.3 and 1.4 illustrate a failure process due to armour unit displacement, and appropriately designed breakwaters usually undergo a gradual rather than rapid failure once the design conditions are exceeded.
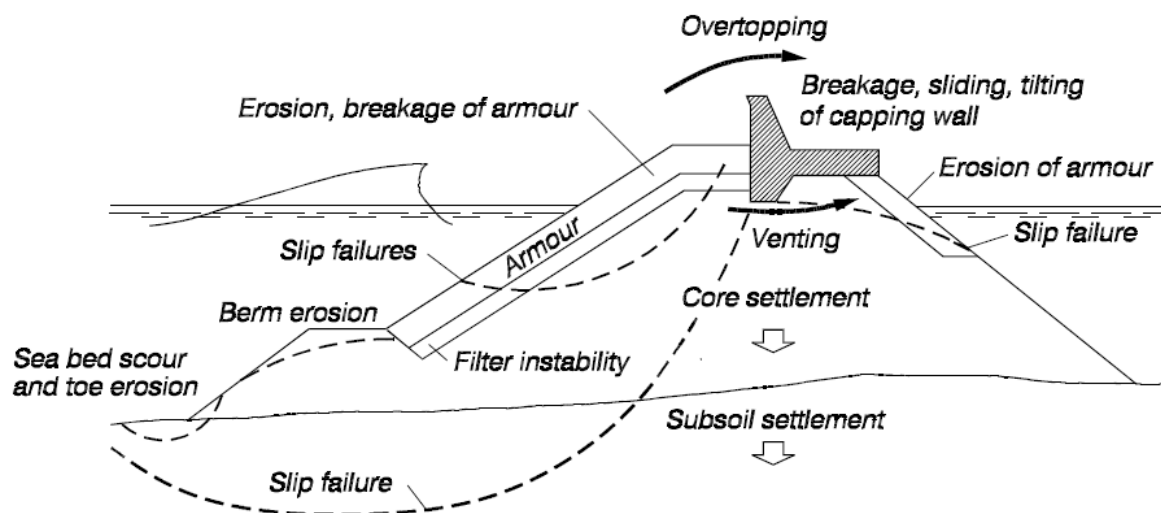
Figure 1. 2 Rubble-mound breakwater failure modes (Burcharth, 1993)

Hydraulic instability of main armor for a conventional multilayer structure

- Displacement of main armor around SWL.
- Subsequent erosion of underlayer and core, resulting in development of S - profile.
- Eventually wash-down of crest structure.

Usually a rather slow development of failure.
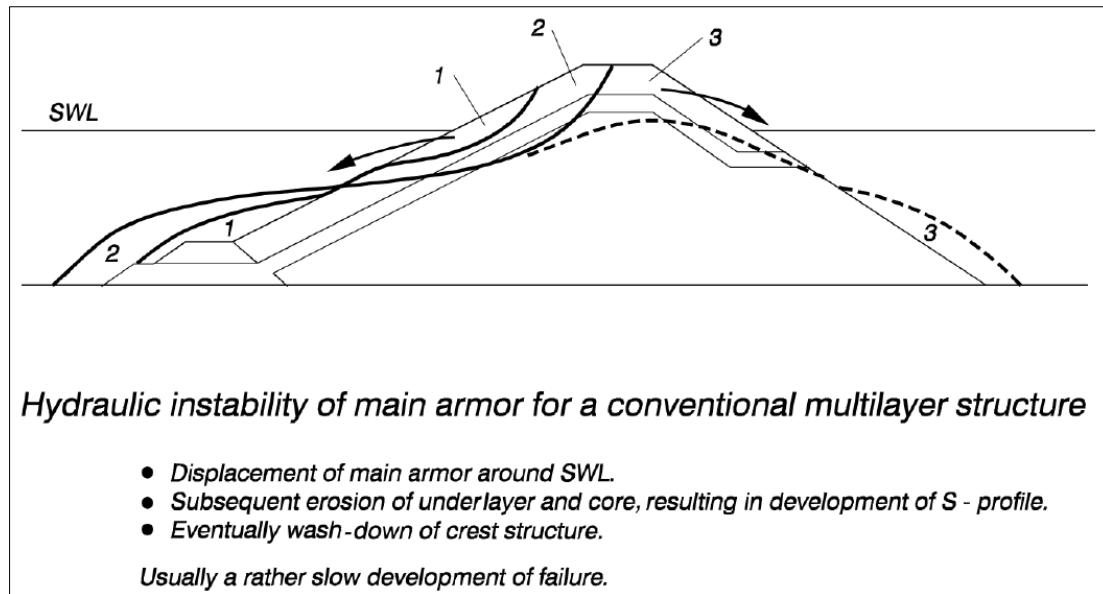
Figure 1. 3 Hydraulic instability of armour layer (CEM, 2002)

Hydraulic instability of single layer randomly placed armor units on rather steep slopes

- Sudden displacement of a large proportion of the main armor layer.
- Subsequent erosion of the exposed underlayer and cone.
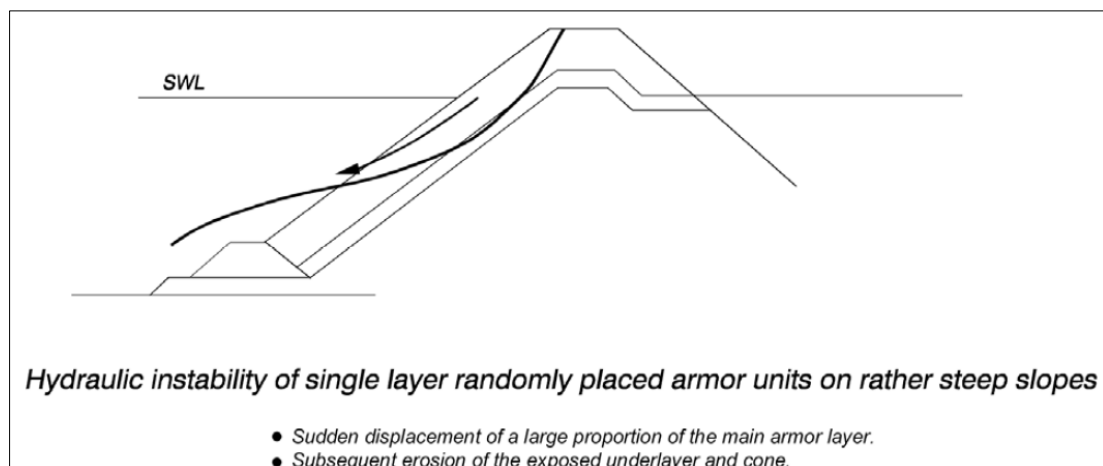
Figure 1. 4 Hydraulic instability of armor layer on steep slope (CEM, 2002)

Hence, armour layer plays an essential role in structural design of rubble mound breakwater. The most frequently used armour unit types around the world are armourstones and precast concrete armour units, and these units are arranged variously in single or double layer in order to attain effective interlocking and better stability. The armour layer which directly resists hydraulic forces needs not only enough hydraulic stability (resistance against displacements) but also enough structural integrity of individual units. Breakage can take place before the hydraulic stability of the units lowers the minimum expected level due to their mechanical and durability properties. The armour unit breakage reduces the stabilizing gravitational force of the unit and possibly reduces interlocking effect, and broken pieces can

be dislodged by incident waves easily, thereby causing armour layer erosion. Moreover, loss of strength and mass of armour units can cause because of weathering through chemical reactions, temperature variations and abrasion, and that can result in a higher risk of breakage and decrease hydraulic stability (CEM, 2002).

Precast concrete armour units (CAUs) have been used as an armouring material of rubble mound structures when large quarry stones are not readily available from local quarries, or under rough wave climates. Various shapes and configurations of CAUs have been developed in order to improve their hydraulic stability/performance and structural strength considering porosity, friction, interlocking effects, casting technology, concrete demand, simplicity of fabrication, and so on, and consequently, they are significantly more stable than armourstones under wave-induced loads.

However, fabrication of CAUs as well as handling of the units to construction site need to be carefully planned to ensure that units do not get damaged and thus overall project cost can be higher remarkably than expected with long construction period. Regarding structural integrity of CAUs, in addition to the stresses caused by mechanical and hydraulic loads, the thermal stress can occur inside the units because of the temperature differences generated by hydration process in curing (Burcharth, 1995). Concrete armour units will break when the stresses acting on the units exceed the strength of concrete, and the breakage of a considerable proportion of the units having complex shapes (say >15%) causes collapse of the armour layer (CEM, 2002).

If it is possible to quarry armourstones of sufficient size, quality and quantity from nearby quarries, armourstones are often more economical to use for the structure protection instead of concrete armour units (Ertas and Topal, 2008/Sigurdarson and Van der Meer, 2017). However, when armourstones are used, it is important to place armourstones on real structure carefully according to the design lines of the structure because leveling the surface after the placement can be tough as the armourstones are very irregular in shape, and it will not be possible to achieve a stable armour layer when the constructed surface mismatch the cross-sectional design line. (Sigurdarson and Van der Meer, 2017).

Therefore, even armourstone application requires not only much time for quarrying process of stones but also many (skilled) workers (excavator operators/divers) for setting up and leveling stones, thereby leading to cost increase (Akiyama, 2001), and larger sizes of

armourstones with increasing design wave loads cannot be economically transported to the site (Muttray & Reedijk, 2008). In addition, recently there has been a shortage of natural rock and consequently the considerable increase of construction and maintenance costs of conventional coastal structures, and then it becomes preferred to use the cheaper materials and systems in hydraulic and coastal structures (Shin, et al., 2019).

1.2 STABILITY AND DAMAGE OF ARMOUR UNITS

Armour layer stability estimation is usually assessed by identifying damage definition, armour unit type, sea state, and damage may define as partial collapse of a structure while the structure is still able to function at or above its minimum design level (CEM, 2002). In laboratory investigations, damage was defined as the amount of armour unit movement by wave forces (hydraulic instability), not of armour unit breakage considering the fact that the armour unit could not be able to break in its small scale model. As illustrated in Figure 1.5, typically armour unit movements can be unit rocking (a), rotation and subsequent displacement of unit out of the layer during down-rush (b) and during up-rush (c), and sliding of several units during down-rush (d) due to compaction or loss of support.

Armour units can displace in different ways due to the storm attacks, and any type of displacement can make a contribution to layer integrity and subsequently function of breakwater. During/after the displacement of units, some units cannot provide protection of the structure completely, although others can still protect the structure without major damage. Different damage definitions (parameters) have been proposed by many researchers, and the main methods to assess damage level are surface profiling and counting the number of displaced units within a specific area. Due to different breakwater designs and different damage definitions, the stability analysis results of armour units cannot be compared precisely.

Generally, surface profiling method estimates eroded area of structure by comparing its initial slope profile and its damaged profile after a specific sea state and duration, assuming that the slope profile can be changed through the erosion, not through the profile settlement, and it does not consider the unit displacement and armour layer porosity. Counting method considers all the armour units displaced from their initial positions by a certain distance (for example: one of or half of unit's length) within a specified area regardless of their displacement

to reach a stable condition. Therefore, it should be concluded that profiling method may cause damage underestimation and counting method can result in damage overestimation (Kamali and Hashim, 2009).

a) *Rocking of unit during up- and down-rush*

b) *Rotation and subsequent down-slope displacement of unit during down-rush*

Point of rotation

c) *Rotation and subsequent up-slope displacement of unit during up-rush*

d) *Sliding of several armor units (armor layer) during down-rush*

Point of rotation
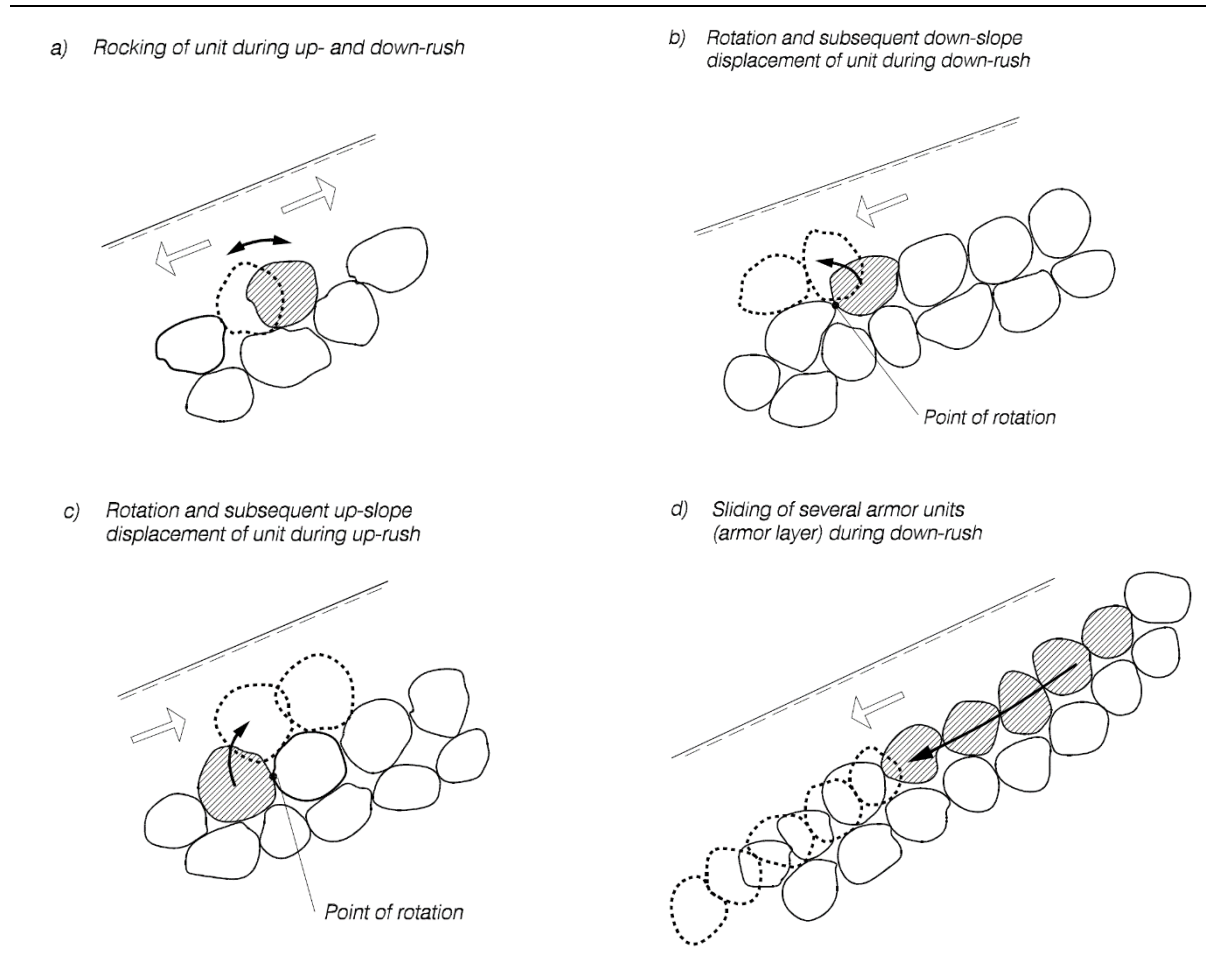
Figure 1. 5 Typical failure modes of armour layer (Burcharth 1993, CEM 2002)

Many empirical stability formulae have been developed to estimate the applicable armour unit weight under design wave loads corresponding to a certain damage level of the units, and improved not to overestimate or underestimate unit weight. However, armour layer stability estimation still mainly depends on the design engineer's experience, and it was noted that the stability formulae are based on small scale model tests and thus have the influence of scale effect and useful for preliminary design. Therefore, large structures should be designed considering the uncertainties of formulae and tests due to diversity of variables of formulae and stochastic nature of wave loads and wave-structure interactions (Kamali and Hashim, 2009).

1.3 FILTER UNIT (FU)

Filter Unit (FU) is a synthetic fiber net bag of (small) rubble stones. The FUs were used first in river works such as protection of bridge foundations, river bank scouring and river bed erosion (Figure 1.6).

Figure 1. 6 FU application for river bank protection (one of Kyowa's Projects)

As shown in Figure 1.7, any type of solid materials such as stones, pebbles could be used as the stuffing material of FUs, and stone filling is not complicated and can be done with few workers. Then, unit installation and removal can be carried out using one point lifting ring, and the ring can provide fast and accurate placement on the sea bed, and consequently can reduce construction and installation time efficiently, and can lower total project costs. In addition, several units can be placed at once by using a lifting frame.

The FUs are highly flexible, that can be placed on any rough surfaces, and the units are environmentally-friendly and durable, made of recycled materials (recycled polyester/nylon) that can save natural resources. It was noted (Kyowa Filter Unit, Subsea Expo AECC 2018 Presentation documents, Sumitomo Corp.,) that the lifespan of net material in sea water is up to 50 years, and the FUs have been applied for protection of subsea assets and structures, and a recognized alternative to rocks (rock dumping) and concrete mattresses. Figure 1.8 illustrates the structures of two FU types before and after stuffing stones, and the difference between them is presented in FUs' previous studies.
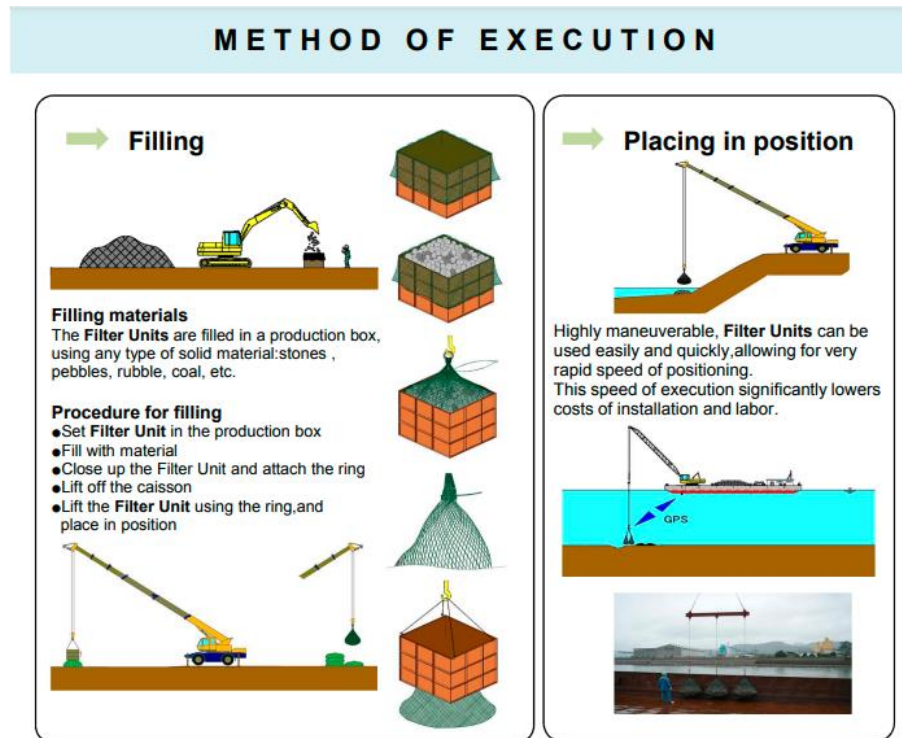
Figure 1. 7 Execution Method (Source: Kyowa's pamphlet)
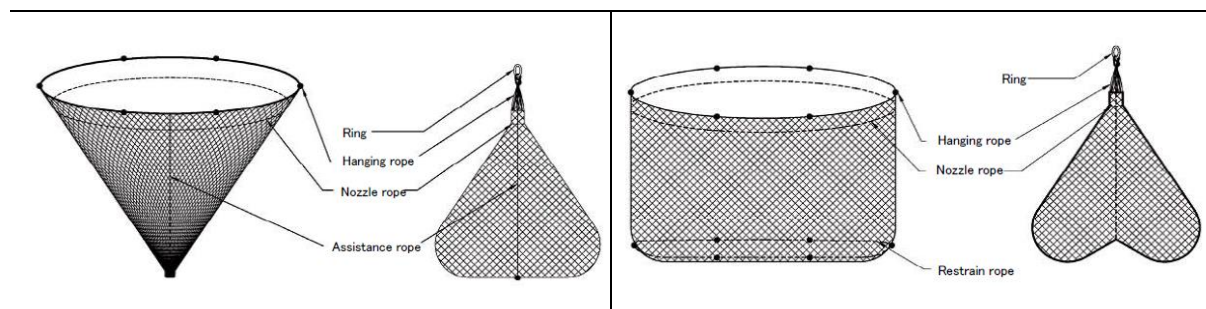
Figure 1. 8 Filter bag structure illustration (Source: Kyowa Filter Unit Brochure)

Some researchers have proposed to apply FUs in coastal and ocean regions because of the FUs' significant characteristics such as high flexibility, porosity and being environmentally-friendly and cost-efficient. In the literature, some studies have been performed in order to apply FUs as a countermeasure against seabed scouring, for instance, scouring of seabed in front of quay walls of ports because of a jet generated from bow thruster of vessel and study resulted in an effective countermeasure (Nakamura, et al., 2011). Moreover, the FUs have been examined to use in the protective cover layer of rubble mound structures exposed to ocean wave action, when large natural rocks are unavailable and concrete armor units are too expensive for execution.

A number of experimental studies on the stability of FUs as an armor unit covering rubble mound under wave motion have been carried out. Akiyama et al., (2001) described the construction method of FUs, and conducted hydraulic model experiments using FUs on a mild slope revetment in the place of armourstones, then concluded that the FUs have high flexibility and hydraulic stability under wave loading compared to the armourstones.

Kubota et al., (2003) modified the conventional FUs used in river works in order to improve not only their stability in the sea state but also their durability because violent collision of stuffing stones with synthetic fiber would damage the net. They carried out both small-scale (1/20) and large-scale (1/5) hydraulic model tests of FUs armouring a rubble mound of composite breakwater (submerged rubble mound). FU model movement was analyzed based on the velocity direction acting on FUs, and FU damage definition was when a FU had moved more than half of its diameter from its initial position. Conclusions were that the modified unit was more stable when the velocity direction was almost horizontal, and when the velocity direction was almost parallel to breakwater slope, both units showed no difference in stability. The modified unit, which has a restraining rope inside connecting the top and bottom of bag, is referred to as the restricted type (S-type FU) (Figure 1.9 (b)), and the conventional unit as the normal type (N-type FU) (Figure 1.9 (a)).

(a) Normal type (N-type FU)

(b) Restricted type (S-type FU)
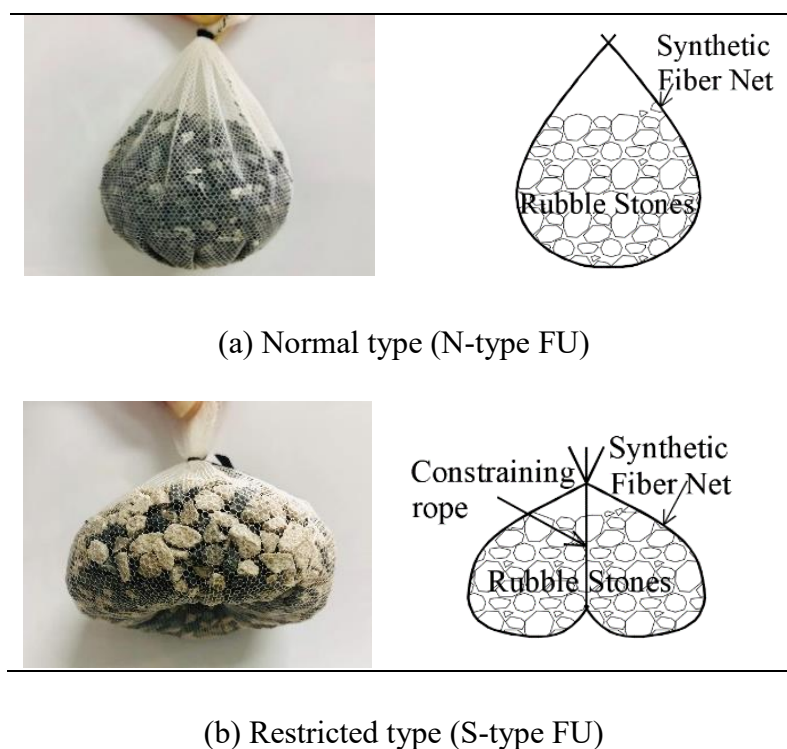
Figure 1. 9 Filter Unit Types

Mizutani et al., (2007) then carried out laboratory experiments using S-type FU model (FU model scale: 1/34), shown in Figure 1.10, under various wave conditions. Models were placed on uniform slopes (1/1.5 & 1/2) of rubble mound breakwater in order to study wave force acting on a model and to evaluate stability condition. In the research, FU damage was when a FU moved more than half of its diameter under regular waves, and under irregular waves, critical condition was when the FU movement reached rank-3 as shown in Figure 1.11 in which the under-layer was already exposed to waves directly. Besides, pressure difference between upper and lower surfaces of model near the shoreline was measured and computed, from which the uplift force was estimated.

As their research summaries, the uplift force has two peak values in one wave period, and magnitude of the uplift force as well as tangential and normal wave forces acting on the model are proportional to tangential wave velocity square, then S-type FUs are suitable for practical use in comparison to natural armourstones from the viewpoint of hydraulic stability.

(a) Plane view   (b) Side view
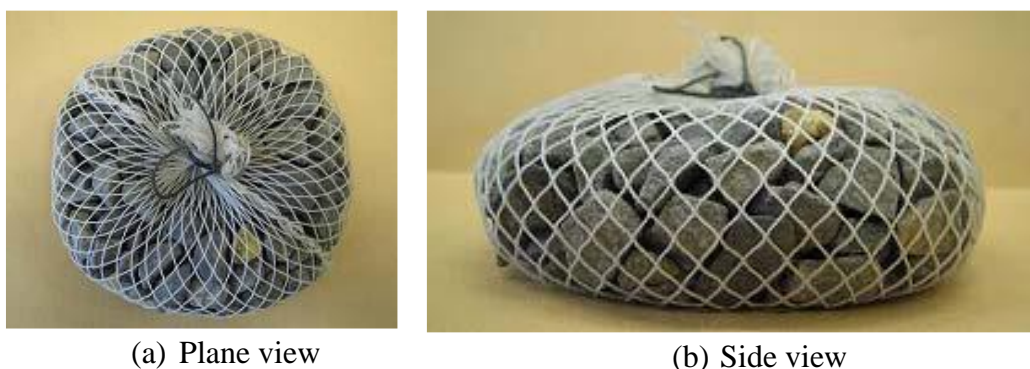
Figure 1. 10 S-type FU model used in the work of Mizutani et al. (2007)
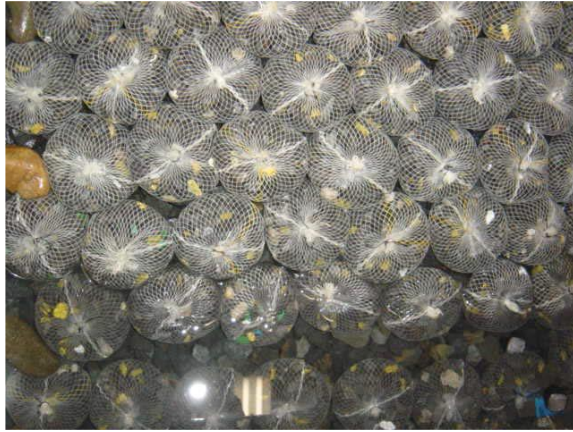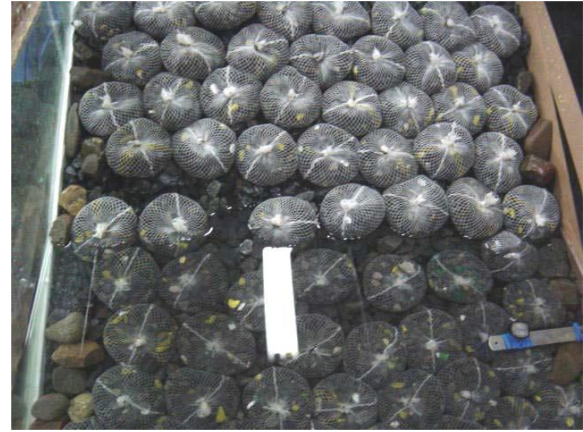
(a) Rank-2   (b) Rank-3

Figure 1. 11 Damage definition in the work of Mizutani et al. (2007)

Saito (2017) also carried out hydraulic FU model experiments on a sloping rubble mound breakwater (1/1.5 of slope) generating irregular waves, and models were not only S-type FU but also N-type FU as given in Figure 1.12 in which FU model scale was 1/40. The models were placed in different arrangements such as one or more layer-overlapping, and damage condition was examined with counting method (number of FUs moved more than one or half of diameter). It was noted that FUs arranged in double-layer stacking had better stability than in single-layer stacking, and the latter arrangement was better than flat placing on rubble mound slope. Next, it was found that S-type was quite difficult to deform on this sloping rubble mound breakwater compared with N-type, and thus provided more stable condition than N-type FU model.

(a) N-type   (b) S-type

Figure 1. 12 FU models used in the work of Saito (2017)

In order to study FU's geometric parameters, available model parameters from the above-mentioned researches as well as of Kyowa's 8t-type were recorded in Table 1.1 and Table 1.2, and the ratios of model diameter to height were found as 3, 3.2, 3.6, 4.1 and 4.3. The other parameters such as constraining rope length and fiber bag size were not described and not focused yet.
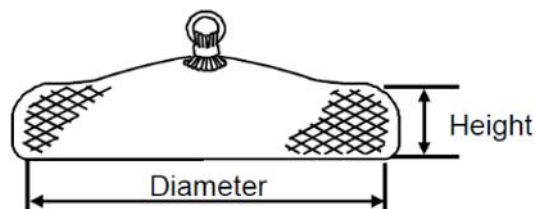
Figure 1. 13 Dimensions of FU installed (source: Kyowa Filter Unit)

Table 1. 1 Model parameters from previous researches

Parameters	Kubota et al., (2003)				Mizutani et al., (2007)	Saito (2017)
Prototype	4t-type				8ton	8t-type (Kyowa's)
Model type	N-type		S-type		S-type	N-type & S-type
Model scale	1/5	1/20	1/5	1/20	1/34	1/40
Mass	32.0 kg	516.7 g	32.0 kg	516.7 g	200 g	125 g
Diameter- D_{FU}	51.0 cm	12.8 cm	47.2 cm	12.8 cm	9 cm	7.5 cm
Height- H_{FU}	12.4 cm	4.0 cm	13.1 cm	4.0 cm	3 cm	1.75 cm
D_{FU}/H_{FU}	4.1	3.2	3.6	3.2	3	4.3
Stuffing stone size	-	-	-	-	-	4 ~ 10 (mm)

Table 1. 2 FU Prototype parameters (8t-type from Kyowa)

FU	Mass	Diameter- D_{FU}	Height- H_{FU}	D_{FU}/H_{FU}
S-type	8 ton	3 m	0.7 m	4.3

1.4 STUDY APPROACH

As presented in section 1.3, researchers have performed hydraulic model experiments to observe and enhance FU's stability and durability in the sea state, and concluded that FUs are appropriate for practical use instead of natural rock (armourstones of rubble mound) from hydraulic stability viewpoint. However, FU's structural parameters have not been examined yet, though FU's diameter and height were described.

This study investigates FU's structural parameter influence on its stability under wave loads in order to assess an effective FU structure. First of all, many FU models have been considered changing FU's fiber bag size and constraining rope length. Then laboratory model experiments have been carried out with the FU models in order to make a comparison of their hydraulic stability, their displacement and damage mechanism due to wave action. This experimental investigation is elaborated in chapter 3.

Furthermore, two dimensional numerical models for representing FUs have been built up using circular finite-sized particles, and the numerical models' deformation on rubble mound surface has been investigated by a combination use of CADMAS-SURF (CS2D) and Discrete Element Method (DEM/2D). CS2D and DEM are used to predict wave motion in and around the models and to estimate the model movement by the wave motion, respectively. From simulation, the damage patterns of FU models during wave attack have been assessed and discussed based on some experimental observations. The details of numerical work are given in Chapter 4, and Chapter 2 describes the theoretical background needed for Chapter 3 and Chapter 4. At the end, the conclusions of experimental and numerical studies are summarized in Chapter 5.

CHAPTER 2

Chapter 2

THEORETICAL BACKGROUND

OUTLINE

Chapter 2 consists of three main sections. Firstly, the stability number estimation formula is described. It is followed by the numerical wave flume model (CADMAS-SURF/2D) including the model settings and wave analysis work. Afterwards, 2D/DEM (Discrete Element Method) which is commonly used in the studies of rubble mound structure deformation and BPM (Bonded Particle Model) that would be applied in this research are explained.

2.1 STABILITY NUMBER

Hudson formula given in (2.1) is used to estimate the required mass for the stability of an armor unit on the surface of rubble mound breakwater,

$$M = \frac{\rho_s H^3}{K_D \left(\rho_s/\rho - 1\right)^3 \cot\alpha} \tag{2.1}$$

Then, Brebner-Donnelly formula (2.2) is used for estimating the stable weight of an armor unit on the surface of rubble foundation of composite breakwater.

$$M = \frac{\rho_s H^3}{Ns^3 \left(\rho_s/\rho - 1\right)^3} \tag{2.2}$$

Comparing (2.1) and (2.2),

$$Ns^3 = K_D \cdot \cot\alpha \tag{2.3}$$

In equations (2.1~2.3), M is the mass of armor unit (FU), ρ_s is the density of stuffing stones, ρ is the density of water, H is the design wave height, K_D is the stability coefficient, α

is the angle of breakwater slope, and Ns is the stability number of the armor unit.

2.2 NUMERICAL WAVE FLUME MODEL

The numerical wave flume model applied in this study was CADMAS-SURF/2D (CS2D), Ver. 5.1 (<u>SU</u>per <u>R</u>oller <u>F</u>lume for <u>C</u>omputer <u>A</u>ided <u>D</u>esign of <u>MA</u>ritime <u>S</u>tructure), which is a two dimensional numerical wave flume developed by Isobe et al. (1999) on the basis of NASA-VOF technique. The governing equations are the continuity equation of an incompressible viscous fluid and the Navier-Stokes equations modified for porous media (2.4~2.6).

$$\frac{\partial \gamma_x u}{\partial x} + \frac{\partial \gamma_z w}{\partial z} = S_p \tag{2.4}$$

$$\lambda_v \frac{\partial u}{\partial t} + \frac{\partial \lambda_x uu}{\partial x} + \frac{\partial \lambda_z wu}{\partial z}$$
$$= -\frac{\gamma_v}{\rho} \frac{\partial p}{\partial x} + \frac{\partial}{\partial x}\left\{\gamma_x v_e\left(2\frac{\partial u}{\partial x}\right)\right\} + \frac{\partial}{\partial z}\left\{\gamma_z v_e\left(\frac{\partial u}{\partial z} + \frac{\partial w}{\partial x}\right)\right\} - D_x u + S_u$$
$$- R_x \tag{2.5}$$

$$\lambda_v \frac{\partial w}{\partial t} + \frac{\partial \lambda_x uw}{\partial x} + \frac{\partial \lambda_z ww}{\partial z}$$
$$= -\frac{\gamma_v}{\rho} \frac{\partial p}{\partial z} + \frac{\partial}{\partial x}\left\{\gamma_x v_e\left(\frac{\partial w}{\partial x} + \frac{\partial u}{\partial z}\right)\right\} + \frac{\partial}{\partial z}\left\{\gamma_z v_e\left(2\frac{\partial w}{\partial z}\right)\right\} - D_z w + S_w - R_z$$
$$- \gamma_v g \tag{2.6}$$

where t is the time, x and z are the horizontal and vertical coordinates, u and w are the horizontal and vertical water particle velocities, ρ is the density of the fluid, p is the pressure, v_e is the sum of kinematic viscosity and eddy viscosity, g is the gravitational acceleration, γ_v is the volume porosity, γ_x and γ_z are the horizontal and vertical components of the surface permeability, and S_p, S_u and S_w are the source terms of wave generation. λ_v, λ_x, λ_z are given by (2.7~2.9) in which C_M is the inertia coefficient.

$$\lambda_v = \gamma_v + (1 - \gamma_v)C_M \tag{2.7}$$

$$\lambda_x = \gamma_x + (1 - \gamma_x)C_M \tag{2.8}$$

$$\lambda_z = \gamma_z + (1 - \gamma_z)C_M \tag{2.9}$$

D_x and D_z are the energy dissipation coefficients, R_x and R_z are the resistance terms for porous structure (2.10~2.11) in the direction of x and z, respectively, C_D is the drag coefficient, Δx and Δz are the horizontal and vertical grid spaces for numerical simulation.

$$R_x = \frac{1}{2}\frac{C_D}{\Delta x}(1 - \gamma_x)u\sqrt{u^2 + w^2} \tag{2.10}$$

$$R_z = \frac{1}{2}\frac{C_D}{\Delta z}(1 - \gamma_z)w\sqrt{u^2 + w^2} \tag{2.11}$$

The free water surface is calculated by using Volume of Fluid (VOF) method (2.12), where F means a function which represents the ratio of the fluid inside each cell, and S_F is the source term for wave generation.

$$\gamma_v \frac{\partial F}{\partial t} + \frac{\partial \gamma_x uF}{\partial x} + \frac{\partial \gamma_z wF}{\partial z} = S_F \tag{2.12}$$

In the model (CS2D), the time step Δt for simulation stability has to satisfy the following two conditions:

① (Courant-Friedrichs-Levy) CFL condition

$$\Delta t \leq \min\left(\frac{\Delta x}{u}, \frac{\Delta z}{w}\right) = \Delta t_c$$

② Stability condition in viscosity term (v)

$$\Delta t \leq \frac{1}{2} \frac{1}{v\left[\left(\frac{1}{\Delta x}\right)^2 + \left(\frac{1}{\Delta z}\right)^2\right]} = \Delta t_v$$

where, Δx and Δz are the horizontal and vertical grid spaces, u and w are the horizontal and vertical wave velocities. The CS2D has a function of "AUTO" which decides Δt by using (2.13) and α is a safety factor ($0.0 < \alpha < 1.0$).

$$\Delta t = \alpha \min(\Delta t_c, \Delta t_v) \tag{2.13}$$

In the CS2D model, a staggered grid method is adopted to computation in which scalar variables are stored in the cell centers and velocity variables are located at the center of the cell surface for each direction, and Donor-Acceptor method is applied for the discretization of VOF equation (Figure 2.1). The settings applied in the present work are listed in Table 2.1, where the wave maker source method and energy damping zone were selected to generate the waves and to reduce the influence of the wave reflection.

The details of the discretization process of the governing equations are given in the CADMAS-Surf manual book, 2001 (in Japanese) and in the appendix section of "Wave Dissipation over Vegetation Fields" Ph.D. thesis (Suzuki, 2011) (in English).

(a) Before   (b) After
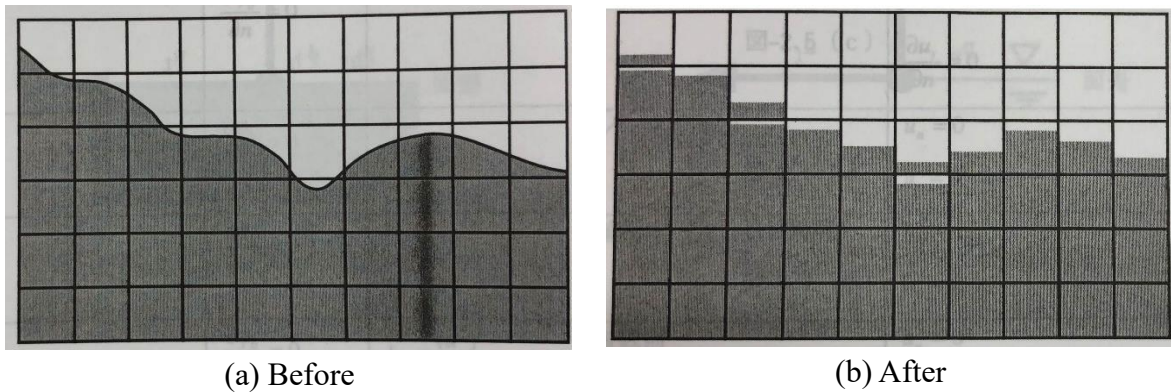
Figure 2. 1 Sketch of free surface modelling by VOF method (CS2D manual, 2001)

Table 2. 1 Numerical methods in CS2D

Function	Method
Time step	AUTO (safety factor, α = 0.1)
Wave function	STOKES (5th-order Stokes theory)
Wave generation model	Wave maker source method
Non-reflective model	Energy damping zone
Discretization scheme for advection terms	VP-DONOR 0.2 (DONOR scheme: Hybrid scheme of ① & ②) ①1st order accuracy upwind difference ②2nd order accuracy central difference
Boundary condition	SLIP
Solving simultaneous linear equations	M-ILUBCGSTAB matrix solver

2.2.1 Selection of applicable non-linear wave theory

An applicable wave theory for practical case study can be selected using shallow water Ursell's parameter (U_r) (2.14). As shown in Figure 2.2, Isobe (2013) reviewed the validity ranges of wave theories such as Stokes, cnoidal and SFM 19 (19th-order Stream Function Method). Roughly, if the parameter (U_r) is smaller than 25, 5th-order Stokes wave theory should be used, and otherwise, 3rd-order cnoidal wave theory should be used.

$$U_r = HL^2/h^3$$

$$L = T\sqrt{gh}$$

$$U_r = gHT^2/h^2$$

(2.14)

where, H is the wave height, h is the water depth, L is the shallow water wavelength, T is the wave period, and g is the gravitational acceleration.
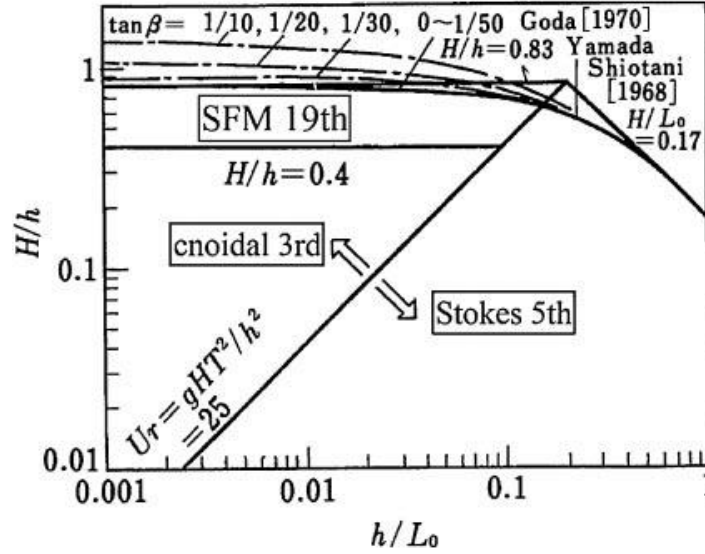
Figure 2. 2 Diagram of selecting appropriate wave theory for the study (Isobe, 2013)

2.2.2 Wave spectrum

The spectrum of irregular waves applied in the study was the modified Bretschneider-Mitsuyasu Spectrum that can be expressed as (2.15), and the significant wave height can be estimated based on the wave spectrum using (2.16 ~2.17) (Goda, 1985).

$$S(f) = 0.205H_{1/3}{}^2 T_{1/3}{}^{-4} f^{-5} exp\left[-0.75(T_{1/3}f)^{-4}\right] \tag{2.15}$$

$$m_0 = \lim_{t_0 \to \infty} \frac{1}{t_0} \int_0^{t_0} \eta^2 dt = \int_0^{\infty} S(f) df \tag{2.16}$$

$$H_{1/3} = 4.004 \eta_{rms} = 4.004\sqrt{m_0} \tag{2.17}$$

where, f is the frequency, $S(f)$ is the spectral density, $H_{1/3}$ and $T_{1/3}$ are significant wave height and significant wave period, m_0 is the representative value of the total wave energy, η is the surface elevation, and η_{rms} is the root-mean-square value of the surface elevation.

31

2.2.3 Incident waves and reflection coefficient

The amplitudes of incident and reflected waves, a_I and a_R, are calculated using A_1, B_1, A_2, B_2 and the phase lag $k\Delta l$, given in Goda and Suzuki (1976) (2.18 & 2.19). Δl is the wave gauge spacing estimated by (2.20), where L_{max} and L_{min} are the wavelengths corresponding to minimum and maximum frequencies (f_{min} and f_{max}). The reflection coefficient can be approximated either as the ratio of a_R to a_I, or as the square root of the ratio of reflected wave energy (E_R) to incident wave energy (E_I) (2.21).

These are applicable to both regular and irregular waves, and it is recommended to install wave gauges at the distance of more than one wavelength from test structure and wave generator in irregular wave case (Goda & Suzuki, 1976).

$$a_I = \frac{1}{2|\sin k\Delta l|}\sqrt{(A_2 - A_1\cos k\Delta l - B_1\sin k\Delta l)^2 + (B_2 + A_1\sin k\Delta l - B_1\cos k\Delta l)^2} \qquad (2.18)$$

$$a_R = \frac{1}{2|\sin k\Delta l|}\sqrt{(A_2 - A_1\cos k\Delta l + B_1\sin k\Delta l)^2 + (B_2 - A_1\sin k\Delta l - B_1\cos k\Delta l)^2} \qquad (2.19)$$

$$\left. \begin{array}{l} f_{min}: \Delta l/L_{max} = 0.05 \\[1em] f_{max}: \Delta l/L_{min} = 0.45 \end{array} \right\} \qquad (2.20)$$

$$K_R = \frac{a_R}{a_I} = \sqrt{E_R/E_I} \qquad (2.21)$$

2.2.4 Morison-type formula

Horizontal and vertical wave forces acting on particle i of the armor unit model, F_{xi} and F_{zi}, are evaluated by Morison-type formula (2.22~2.23).

$$F_{xi} = \frac{1}{2}\rho C_D A_i\sqrt{(u_i)^2 + (w_i)^2}(u_i) + \rho V_i C_M \frac{\partial(u_i)}{\partial t} \qquad (2.22)$$

$$F_{zi} = \frac{1}{2}\rho C_D A_i \sqrt{(u_i)^2 + (w_i)^2}(w_i) + \rho V_i C_M \frac{\partial(w_i)}{\partial t} \qquad (2.23)$$

where, C_D and C_M are the drag and inertia coefficients, ρ is the water density, A_i and V_i are the projected area and volume of particle i, u_i and w_i are the water particle velocities acting on particle i in horizontal and vertical direction respectively.

2.2.5 Porosity estimation

The rubble mound structure was treated as a porous model, and the porosity for each cell was calculated using (2.24), (Maeno et al., 2009).

$$n = (A_f + A_s n_0)/(A_f + A_s) \qquad (2.24)$$

where, A_f is the fluid area in the cell, A_s is the area of rubble particles in the cell, and n_0 is the particle porosity ($n_0 = 0.39$ was used with reference to Maeno et al., 2009).

2.3 DISCRETE ELEMENT METHOD (DEM)

DEM (Discrete Element Method or Distinct Element Method), introduced by Cundall & Strack (1979), is a numerical method that mimics a material as an assemblage of discrete particles with a finite mass, and monitors the particle interaction by tracing the movement of individual particles under the forces acting on them such as particle contact forces, externally applied forces and body forces. The basic particles are circular (in 2D) or spherical (in 3D) rigid bodies, and interact only at the soft contacts, and can also be arranged together to model any arbitrary shape of material. The particles are allowed to overlap on each other at their contact points, though the overlap's magnitude is directly related to the particle contact force, and thus a small amount of the particle sizes is considered as the overlap in calculation.

DEM is widely applied in coastal engineering to estimate the deformation of rubble mound structures due to hydrodynamic forces (Kiyama & Fujimura, 1983, Araki et al., 2001, 2002, Maeno et al., 2005, 2009, Fukumizu et al., 2018 and Jafari, et al., 2021) as well as to estimate armour block displacement on breakwater (Araki and Deguchi, 2011).

The governing equations for two-dimensional individual particles are the following translation and rotation motion equations (for particle i, 2.25~2.27), assuming that the applied wave forces (F_{xi} and F_{zi}) are acting on the center of gravity of the particles. (Particle j: every particle in contact with the particle i)

$$(m_i + m_i')\ddot{u}_i = \sum_j [f_x]_{ij} + F_{xi} \tag{2.25}$$

$$(m_i + m_i')\ddot{w}_i = \sum_j [f_z]_{ij} + F_{zi} - V_i(\rho_i - \rho)g \tag{2.26}$$

$$(I_i + I_i')\ddot{\theta}_i = \sum_j [M]_{ij} \tag{2.27}$$

where m_i and m_i' are the mass and added mass of particle i, I_i and I_i' are the moment of inertia and added moment of inertia of the particle i, $\ddot{u}_i$, $\ddot{w}_i$ and $\ddot{\theta}_i$ are the horizontal, vertical and angular accelerations of the particle i, F_{xi} and F_{zi} are the horizontal and vertical wave forces (external forces) acting on the particle i, V_i and ρ_i are the volume and density of the particle i, $\sum_j [f_x]_{ij}$ and $\sum_j [f_z]_{ij}$ are the sum of horizontal and vertical contact forces arising from particles j in contact, and $\sum_j [M]_{ij}$ is the sum of moment (about the particle i's center) arising from particle contact with particles j.

2.3.1 Contact force calculation

In the DEM, contact forces between particles can be assessed by using various (constitutive models) contact force models such as a linear spring-dashpot model, non-linear Hertz-Mindlin contact models, and so on (Miyata et al., 2002). Only the most common model that we applied in the study is presented herein, and it is the linear spring-dashpot model (Kelvin-Voight model) consisting of an elastic spring, a viscous damping dash pot and a friction slider as shown in Figure 2.3, where K_n and K_s are the contact normal and shear stiffness, μ is the friction coefficient, and η_n and η_s are the normal and shear damping coefficients.

Hence, these input parameters can significantly affect the inter-particle forces as well as the calculation results, and the parameters have to be determined carefully. In the literature,

the parameters are evaluated either using analytical assumption or inverse calibration methods (Sadek, 2013). In the former one, the input parameters are estimated from the existing theory using material properties such as Young's modulus and Poisson's ratio, and in the inverse calibration method, the parameters are found by matching the model results with experimental results.
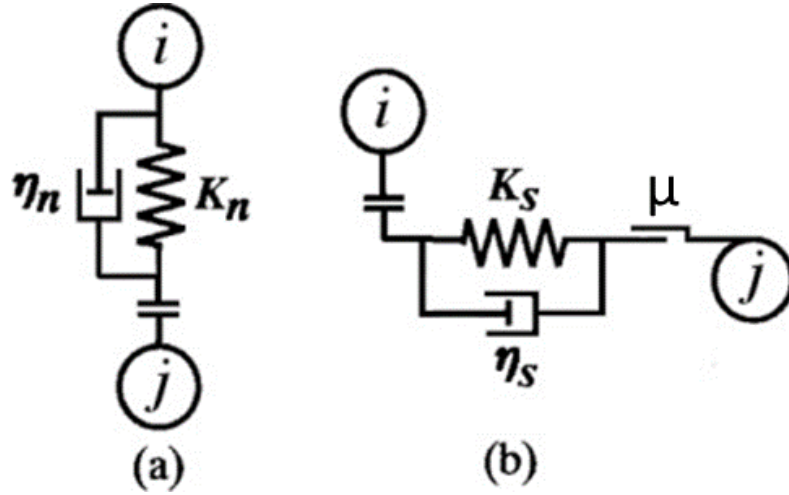

Figure 2. 3 Contact forces between particle i and j in (a) normal direction (b) tangential (shear) direction (Linear spring-dashpot model)
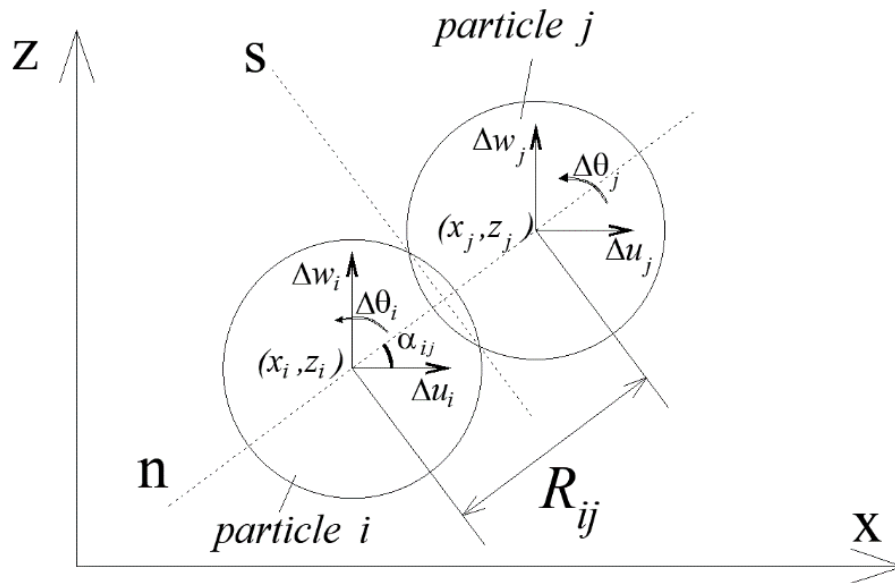

Figure 2. 4 Contact condition and relative particle displacements

The contact condition of numerical particles for the study followed (2.28) in which r_i and r_j are the radius of particles i and j, and R_{ij} is the distance between the particles (Figure2.4).

$$r_i + r_j \geq R_{ij} \; where \; R_{ij} = \sqrt{(x_i - x_j)^2 + (z_i - z_j)^2} \qquad (2.28)$$

The particle contact forces (from 2.25~2.27) acting on particle i are resolved into normal and tangential components on the contact plane (2.29~2.30), and the moment arising from the contact is obtained as given in (2.31). (On the contact plane (n, s): the force and moment acting on the particle i are taken positive if acting in the compressive and counterclockwise direction)

$$\sum_j [f_x]_{ij} = \sum_j \{-f_n \cos \alpha_{ij} + f_s \sin \alpha_{ij}\} \qquad (2.29)$$

$$\sum_j [f_z]_{ij} = \sum_j \{-f_n \sin \alpha_{ij} - f_s \cos \alpha_{ij}\} \qquad (2.30)$$

$$\sum_j [M]_{ij} = \sum_j \{-f_s \cdot r_i\} \qquad (2.31)$$

Then, the normal and tangential particle contact forces (f_n and f_s) at the time t are assessed by (2.32~2.37), where e_n and e_s are the normal and tangential contact force (elastic spring), d_n and d_s are the normal and tangential damping force (dashpot), and Δu_n and Δu_s are the normal and tangential relative displacements of particle i with respect to particle j during the time, Δt.

$$[f_n]_t = [e_n]_t + [d_n]_t \qquad (2.32)$$

$$[f_s]_t = [e_s]_t + [d_s]_t \qquad (2.33)$$

$$[e_n]_t = [e_n]_{t-\Delta t} + K_n \Delta u_n \qquad (2.34)$$

36

$$[d_n]_t = \eta_n \Delta u_n / \Delta t \tag{2.35}$$

$$[e_s]_t = [e_s]_{t-\Delta t} + K_s \Delta u_s \tag{2.36}$$

$$[d_s]_t = \eta_s \Delta u_s / \Delta t \tag{2.37}$$

in which, the relative displacements of particle i with respect to particle j on the contact plane (Figure 2.4) are estimated using (2.38~2.39).

$$\Delta u_n = (\Delta u_i - \Delta u_j) \cos \alpha_{ij} + (\Delta w_i - \Delta w_j) \sin \alpha_{ij} \tag{2.38}$$

$$\Delta u_s = -(\Delta u_i - \Delta u_j) \sin \alpha_{ij} + (\Delta w_i - \Delta w_j) \cos \alpha_{ij} + (r_i \Delta \theta_i + r_j \Delta \theta_j) \tag{2.39}$$

In the typical DEM, the particles are non-cohesive, and thus, the tensile force is not allowed between the particles (Gotoh, et al., 1997). For this characteristic, in the normal direction when $[e_n]_t < 0$,

$$[e_n]_t = [d_n]_t = 0, and \ [e_s]_t = [d_s]_t = 0 \tag{2.40}$$

However, in the tangential direction, the conditions of tangential forces are specified by the Coulomb-type friction law as follows:

When $|[e_s]_t| > \mu [e_n]_t$,

$$[e_s]_t = \acute{\mu} [e_n]_t. SIGN([e_s]_t), and \ [d_s]_t = 0 \tag{2.41}$$

in which μ and μ' are the static and dynamic friction coefficients.

2.3.2 Time integration of motion equations

The DEM typically uses an explicit central difference type algorithm to integrate the governing motion equations and thus the time integration is as the following finite difference schemes for accelerations and velocities, and in which the superscript n indicates nth

calculation step, and Δt is the time step.

Accelerations: $\ddot{u}^n = \dfrac{\dot{u}^{n+1/2} - \dot{u}^{n-1/2}}{\Delta t}$

Velocities: $\dot{u}^{n+1/2} = \dfrac{u^{n+1} - u^n}{\Delta t}$
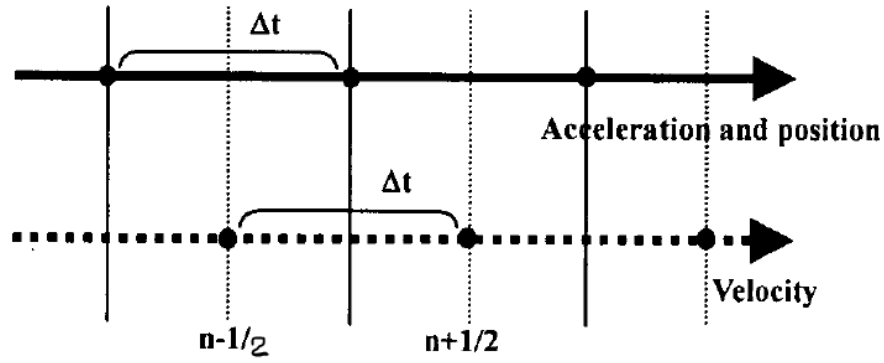
Figure 2. 5 Diagram of time stepping scheme (Miyata et al., 2002)

Thus, employing these schemes, the translational and rotational velocities from (2.25 ~ 2.27) can be obtained as:

$$\dot{u}_i^{\,n+1/2} = \dot{u}_i^{\,n-1/2} + \ddot{u}_i^{\,n}\Delta t \qquad (2.42)$$

$$\dot{w}_i^{\,n+1/2} = \dot{w}_i^{\,n-1/2} + \ddot{w}_i^{\,n}\Delta t \qquad (2.43)$$

$$\dot{\theta}_i^{\,n+1/2} = \dot{\theta}_i^{\,n-1/2} + \ddot{\theta}_i^{\,n}\Delta t \qquad (2.44)$$

Then, the new translation position and rotation angle of the particle i can be updated as follows:

$$u_i^{\,n+1} = u_i^{\,n} + \dot{u}_i^{\,n+1/2}\Delta t \qquad (2.45)$$

$$w_i^{\,n+1} = w_i^{\,n} + \dot{w}_i^{\,n+1/2}\Delta t \qquad (2.46)$$

38

$$\theta_i^{n+1} = \theta_i^n + \dot{\theta}_i^{n+1/2}\Delta t \tag{2.47}$$

The explicit time integration scheme imposes the limitation on the time step size, and the calculation is conditionally stable only if the time step size is small enough. Therefore, it is important to assess the optimal time step value in order to save the computation time. The time step Δt must not be larger than the critical time step Δt_{cr} evaluated using (2.48) (Rojek et al., 2011).

$$\Delta t_{cr} = 2.\sqrt{\frac{m_{min}}{k_n}}$$

$$\Delta t \leq \Delta t_{cr} \; ; \; \Delta t = \alpha.\Delta t_{cr} \tag{2.48}$$

where, α is a certain safety factor (α=0.1 - 0.2), m_{min} is the minimum particle mass, and k_n is the corresponding normal contact stiffness.

2.3.3 Bonded-Particle Model (BPM)

Within DEMs, bonded-particle model (BPM), proposed by Potyondy and Cundall (2004), approximates the mechanical behavior of material by representing the material as a cemented particle assembly, adding a bond model to the typical DEM. There are two bond models: contact bond model and parallel bond model in the BPM, and only the parallel bond model is described herein.

The bond model named as the parallel bond can transmit not only forces (normal and tangential forces: $f_{B,n}$ and $f_{B,s}$) but also moments (bending moment, $M_{B,s}$, and twisting moment, $M_{B,n}$) between particles (For the two dimensional model, the twisting moment is zero). The bond's forces and moment are assessed by (2.50~2.52) in 2D.

The parallel bond model is defined by five parameters: normal and shear stiffnesses per unit area ($k_{B,\,n}$ & $k_{B,\,s}$), tensile and shear strengths (σ & τ) and bond-radius multiplier (λ). The bond breaks if the maximum tensile (σ^{max}) and shear (τ^{max}) stresses acting on it exceed its tensile and shear strength (σ and τ). The tensile and shear stresses acting on a bond are calculated by using beam theory (2.53~2.54).

Figure 2.6 shows a parallel bond model between discrete particles i and j, where R and L are the bond radius and bond length, and the bond radius (R) is set based on the particles' radius (r_i, r_j) and bond-radius multiplier (λ) as given in (2.49), and the detail of the relation between the bond length (L) and normal stiffness parameter is presented in the work of Potyondy and Cundall (2004).

$$R = \lambda \min(r_i, r_j) \tag{2.49}$$

$$f_{B,n} = k_{B,n} A \Delta u_n \tag{2.50}$$

$$f_{B,s} = k_{B,s} A \Delta u_s \tag{2.51}$$

$$M_{B,s} = k_n I \Delta\theta \tag{2.52}$$

$$\sigma^{max} = \frac{-f_{B,n}}{A} + \frac{|M_{B,s}| R}{I} \tag{2.53}$$

$$\tau^{max} = \frac{|f_{B,s}|}{A} + \frac{|M_{B,n}| R}{J} \tag{2.54}$$

in which A, I and J are the bond cross-section's area, moment of inertia and polar moment of inertia, respectively. In the BPM, local non-viscous damping is used by identifying damping coefficients. The damping forces (f_x^{damp} & f_z^{damp}) and damping moment (M^{damp}) applied to the particle i are given by (2.55~2.57).

$$f_x^{damp} = -\alpha^t |F^x| \, sign(\dot{u}_i) \tag{2.55}$$

$$f_z^{damp} = -\alpha^t |F^z| \, sign(\dot{w}_i) \tag{2.56}$$

$$M^{damp} = -\alpha^r |M|\, sign(\dot{\theta}_i) \tag{2.57}$$

where, $\dot{u}_i$, $\dot{w}_i$ and $\dot{\theta}_i$ are the horizontal, vertical and rotational velocities of the particle i, $|F^x|$, $|F^z|$ and $|M|$ are the magnitude of the unbalanced forces and moment acting on the particle i, and α^t and α^r are the respective damping coefficients for the translation and rotation motion.
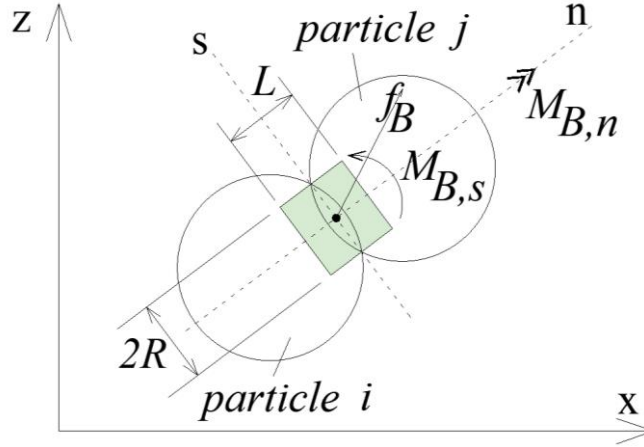

Figure 2. 6 Parallel bond model between discrete particles

Hence, after adding a parallel bond model, the governing equations (2.25~2.27) can be written as (2.58~2.60); in which $\sum_j [f_x]_{ij}$, $\sum_j [f_z]_{ij}$ and $\sum_j [M]_{ij}$ are the particle contact forces and moment from the particles j in contact including only the spring component (spring-dashpot).

$$(m_i + m_i')\ddot{u}_i = \sum_j [f_x]_{ij} + F_{xi} + \sum_j [f_{B,x}]_{ij} + f_x^{\ damp} \tag{2.58}$$

$$(m_i + m_i')\ddot{w}_i = \sum_j [f_z]_{ij} + F_{zi} - V_i(\rho_i - \rho)g + \sum_j [f_{B,z}]_{ij} + f_z^{\ damp} \tag{2.59}$$

$$(I_i + I_i')\ddot{\theta}_i = \sum_j [M]_{ij} + \sum_j [M_B]_{ij} + M^{damp} \tag{2.60}$$

2.3.4 DEM calculation procedure

Figure 2.7 shows calculation steps how individual particle (Particle i) movement are traced within one-time step under loadings. First, contact detection is carried out based on particle position, and inter-particle forces as well as bond-transmitted forces and moment, if it is a bonded particle contact, are estimated. Then, wave forces acting on particle i by Morison-type formula using wave motion data from CS2D and damping forces and moment by local non-viscous damping system are estimated. Afterwards, particle acceleration and particle velocity are assessed and finally new particle position is obtained.
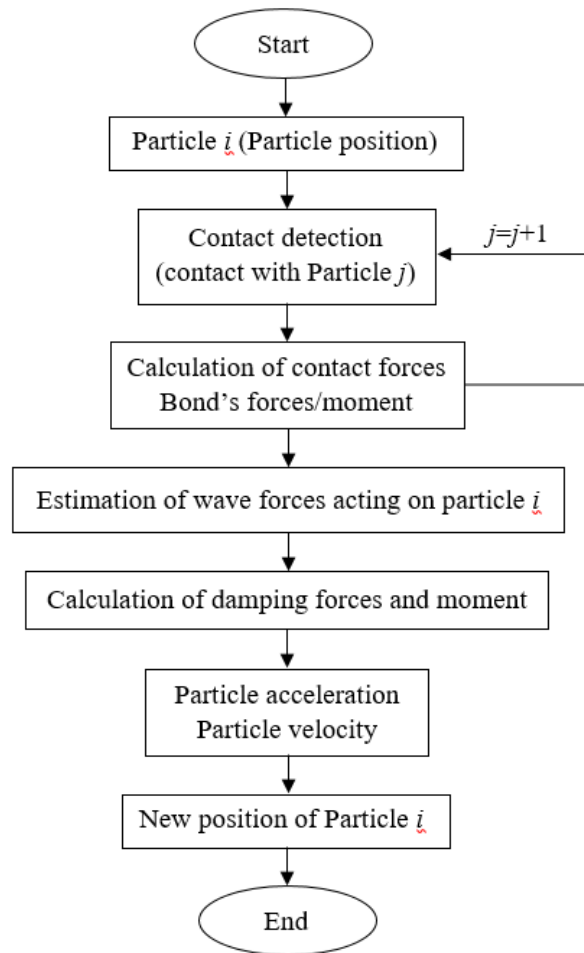
Figure 2. 7 Calculation flow within one-time step of DEM

CHAPTER 3

Chapter 3

EXPERIMENTAL STUDY

OUTLINE

Chapter 3 is assigned mainly for the detailed explanation of hydraulic FU model experiments. First of all, a brief introduction is given on the experiments carried out in a two-dimensional wave flume, which is followed by explanation of the experiments' objectives and FU models. Afterwards, methodology including the experimental setup, test condition and test procedure is described in detail, and finally the experimental results are presented.

3.1 INTRODUCTION

All these hydraulic FU model experiments have been conducted in a two-dimensional wave flume at Hydraulic Laboratory of Osaka University. The wave flume is 30 m-long, 0.71 m-wide, and 1 m-deep. Rubble mound breakwater was constructed on a 1/10 fixed bottom. A piston type wave generator, which is used to generate both regular and irregular waves, is installed at one end of the wave flume.

In the study, two hydraulic FU model experiments have been performed: 'Single-FU' experiment and 'Multiple-FU' experiment. Various S-type FU models and one N-type FU model were used in the former experiment to compare their hydraulic stability and to select an optimum FU structure. The 'Multiple-FU' experiment has then been carried out, using the FUs of optimum type selected from the Single-FU experiment, on rubble mound breakwater under irregular waves to evaluate stability number of the FUs with corresponding damage level. The hydraulic stability of the FUs was studied by video and photo techniques in the experiments.

3.2 OBJECTIVES

The primary objectives of experiments are 1) to investigate influence of the FUs' geometric parameters on their hydraulic stability on rubble mound, 2) to examine deformation

mechanism of FUs on rubble mound during wave action and 3) to estimate stability number of the FUs with appropriate damage definition.

3.3 EXPERIMENTAL FU MODELS

Some parameters of the prototype and model filter units are given in Table 3. 1. Scales were calculated based on the Froude similarity. The model scale ratios for Single-FU experiment and Multiple-FU experiment were applied as 1/35 and 1/40 respectively. The larger scale ratio was used for the Single-FU experiment in which various FUs were tested individually so that it would be easier to find the difference of individual characteristics from the view point of hydraulic stability.

In the first experiment aimed at studying and comparing the stability of various FU structures, eight FU models in total were tested. Tests included one N-type FU and two groups of S-type FUs (Group A and Group B), and the S-type FUs were divided in accordance with their filter net size and constraining rope length. All these FU models have the same mass, 187 g, and approximately the same volume of stuffing stones.

Table 3. 1 Parameters of the prototype and FU models

Model Scale	1/1	1/35	1/40
(FU) Weight (kg)	8000	0.187	0.125
(FU) Diameter (mm)	3000	86	75
(FU) Height (mm)	700	20	17.5
(FU) Volume	5.0 m^3	117 cm^3	78 cm^3
Stuffing stone size (mm)	75~300	2.1~8.6	1.9~7.5

The FU models in Group A have the same constraining rope length, but different cut lengths of filter net. Group B includes the FUs having different constraining rope lengths with the same cut length of filter net. Parameters, size of filter net and constraining rope length for

the FU models tested in the experiment are given in Tables (3. 2~ 3. 3). Group-A FU models are arranged in ascending order of filter net size from left to right, and the diameter of the model becomes larger and the height of the model is slightly lower. Ratios of model diameter to height were between 1.8 and 5.0 in the present study, and in the previous studies described in Chapter 1, the range of this ratio (model diameter/height) was between 3 and 4.3.

Not only the ratio of model diameter to height but also ratio of constraining rope length to height were estimated as shown in the Tables (3. 2~3. 3). Then, by neglecting the elongation effect of fiber material, volume ratio of fiber bag to filling stones was assumed as 1 for A1 (the most compact unit), and the volume ratios (of bag/stones) for the other FU models were calculated, based on initial cut length of filter net, that were 1.2 for A2-FU, 1.3 for A3/B2/B1/B3, 1.4 for A4 and 1.6 for A5. The FU type, which had the highest stability concerning the first experimental results, was used in Multiple-FU experiment.

Table 3. 2 Parameters of Group A (S-type FUs)

	A1	A2	A3	A4	A5
Group A (S-type FUs)					
Cut Length of Filter Net (mm)	200	240	260	280	320
Cut Width of Filter Net (mm)	120	120	120	120	120
Constraining Rope Length (mm)	28	28	28	28	28
Ratio (Diameter/Height)	1.8	2.9	3.6	4.0	5.0
Ratio (Constraining rope length /Height)	0.7	1.0	1.1	1.2	1.4
Volume ratio (Bag/stuffing stones) (with assumption)	1	1.2	1.3	1.4	1.6

Table 3. 3 Parameters of Group B (S-type FUs)

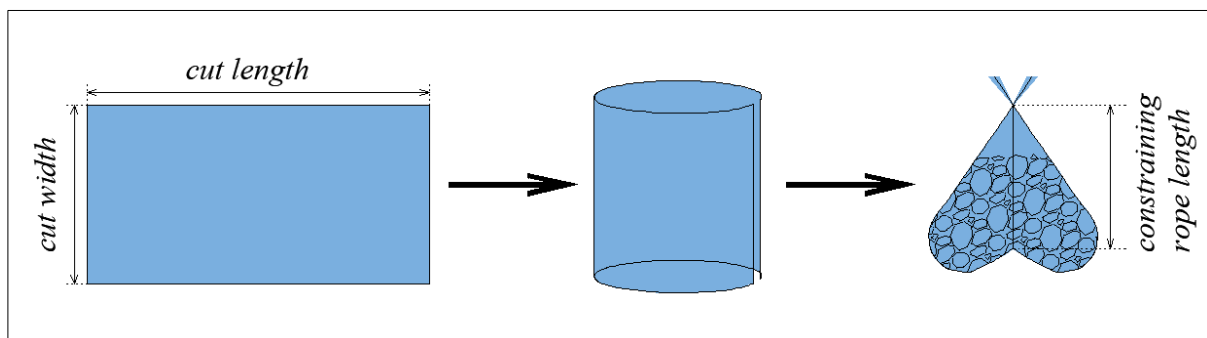|	B1	B2	B3
Group B (S-type FU)			
Cut Length of Filter Net (mm)	260	260	260
Cut Width of Filter Net (mm)	120	120	120
Constraining Rope Length (mm)	18	28	38
Ratio (Diameter/Height)	3.4	3.6	4.0
Ratio (Constraining rope length /Height)	0.7	1.1	1.6
Volume ratio (Bag/stuffing stones) (with assumption)	1.3	1.3	1.3

Figure 3. 1 Sketch showing dimensions of FU models

3.4 METHODOLOGY

3.4.1 Single-FU Experiment

In this experiment, several FU models presented in the above section were tested individually on a fixed rubble mound surface and on original rubble mound surface under regular waves in order to study the deformation mechanism of the individual FU models, and in order to compare the wave resistance stability of the FUs.
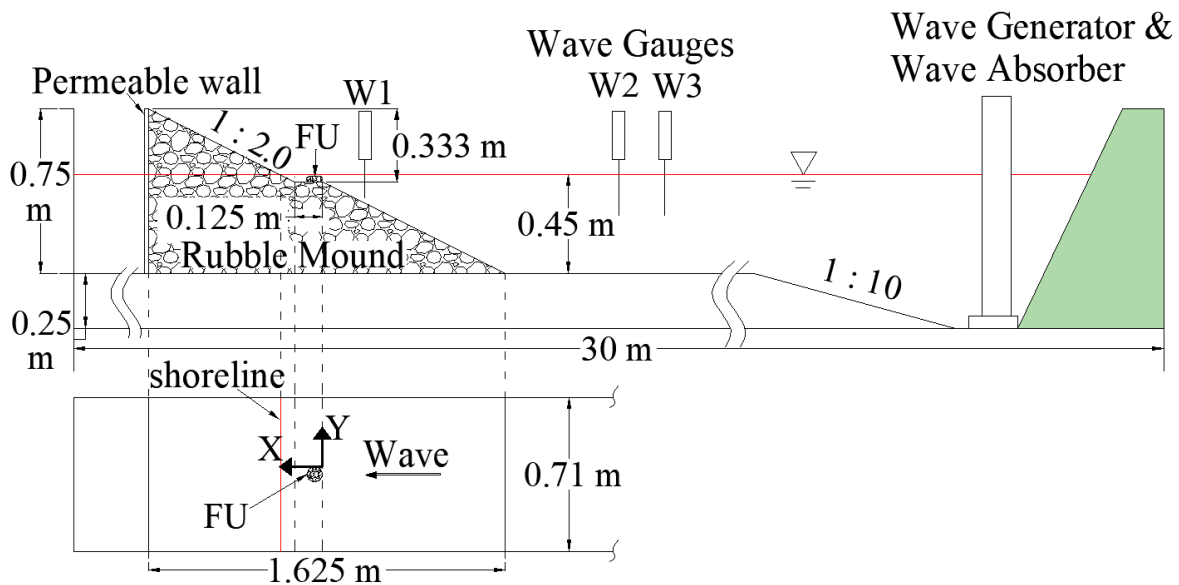
3.4.1.1 Experimental Setup

Figure 3. 2 Single-FU Experimental setup

The side view and plan view of Single-FU experimental set-up in the wave flume is given in Figure 3. 2. In the experiment, water depth (h) was kept constant at 0.45 m, and FU model was placed at the seaward edge of flat portion of a fixed rubble mound breakwater. The rubble mound breakwater was constructed using crushed stones (d_{50}=20 mm), and an adhesive glue was used to prevent scouring around the FU model. The porosity of the breakwater was carefully reproduced, though the surface of the rubble mound around the FU model was rough for some extent.

As shown in the Figure 3. 2, three wave gauges were applied; one was installed near

the FU model and the other two wave gauges were installed offshore at intervals of 500 mm to capture incident and reflected waves.

3.4.1.2 Experimental Conditions and Test Procedure

Regular waves of wave period, 1.0 second, were generated in the experiment. The tests were started with small amplitude waves (wave height, H ≈ 5 cm) which did not cause any significant movement of FU model, and the wave height was gradually increased until the FU damage occurred due to the striking waves. The height of the striking waves was increased without returning the FU to its initial position. The number of waves for each wave height rank was set to approximately 300. The test was then repeated three times.

3.4.2 Multiple-FU Experiment

The FU-A3/B2 and FU-A2, selected from the Single-FU experiment, were subjected to irregular waves in Multiple-FU experimental cases. These irregular wave experiments (model scale 1/40) were conducted on a slope of 1:2.0 of rubble mound breakwater in order to investigate the number of FUs displaced from their initial position and to estimate uncovered area ratio after each wave height attack with increasing significant wave height.

3.4.2.1 Experimental Setup

Figure 3. 3 and 3. 4 illustrate schematic diagrams of the Multiple-FU experimental set-up in the wave flume and the arrangement of FU models on surface of the rubble mound structure. Similar to the first experiment, the rubble mound structure was built behind permeable wall by using crushed stones whose median diameter (d_{50}) is 20 mm, and three wave gauges were installed to evaluate significant wave height, significant wave period, wave reflection coefficient, etc. Furthermore, the FUs were placed between 200 mm above and below the still water level. The total number of FUs arranged in Figure 3. 3 were 117.
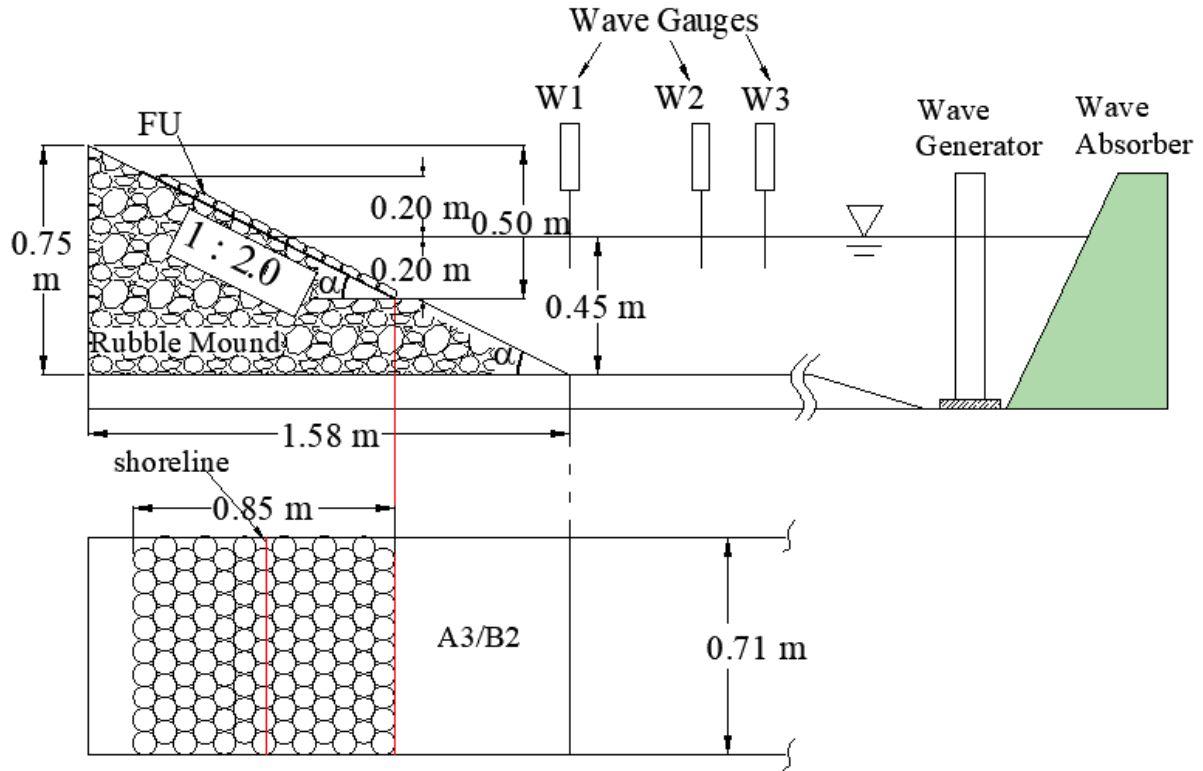
Figure 3. 3 Multiple-FU experimental setup (without lateral control)

The experimental condition shown in Figure 3. 3 was modified based on the experimental experience in order to reduce the FU damage, and under the modified experimental conditions not only FU-A3/B2 type but also FU-A2 type were tested and compared. In Figure 3. 4 (the modified experimental setup), after the FUs were placed, steel plates were fixed at both ends of the FU layer to limit the lateral movement due to the gaps between FU layer and the flume, and some FUs were placed at the bottom of FU slope to obtain a support for the FU slope. The FUs that were fixed with steel plates were not considered in FU damage analysis (shaded FUs in the Figure 3. 4). The number of FUs placed in FU-A3/B2 case and FU-A2 case was not the same as FU sizes were different. The surface area that was considered in the FU damage calculation was the same (919 mm x 560 mm). The numbers of FUs that were not constrained in the focused area were 98 and 112 for the FU-A3/B2 case and the FU-A2 case respectively.
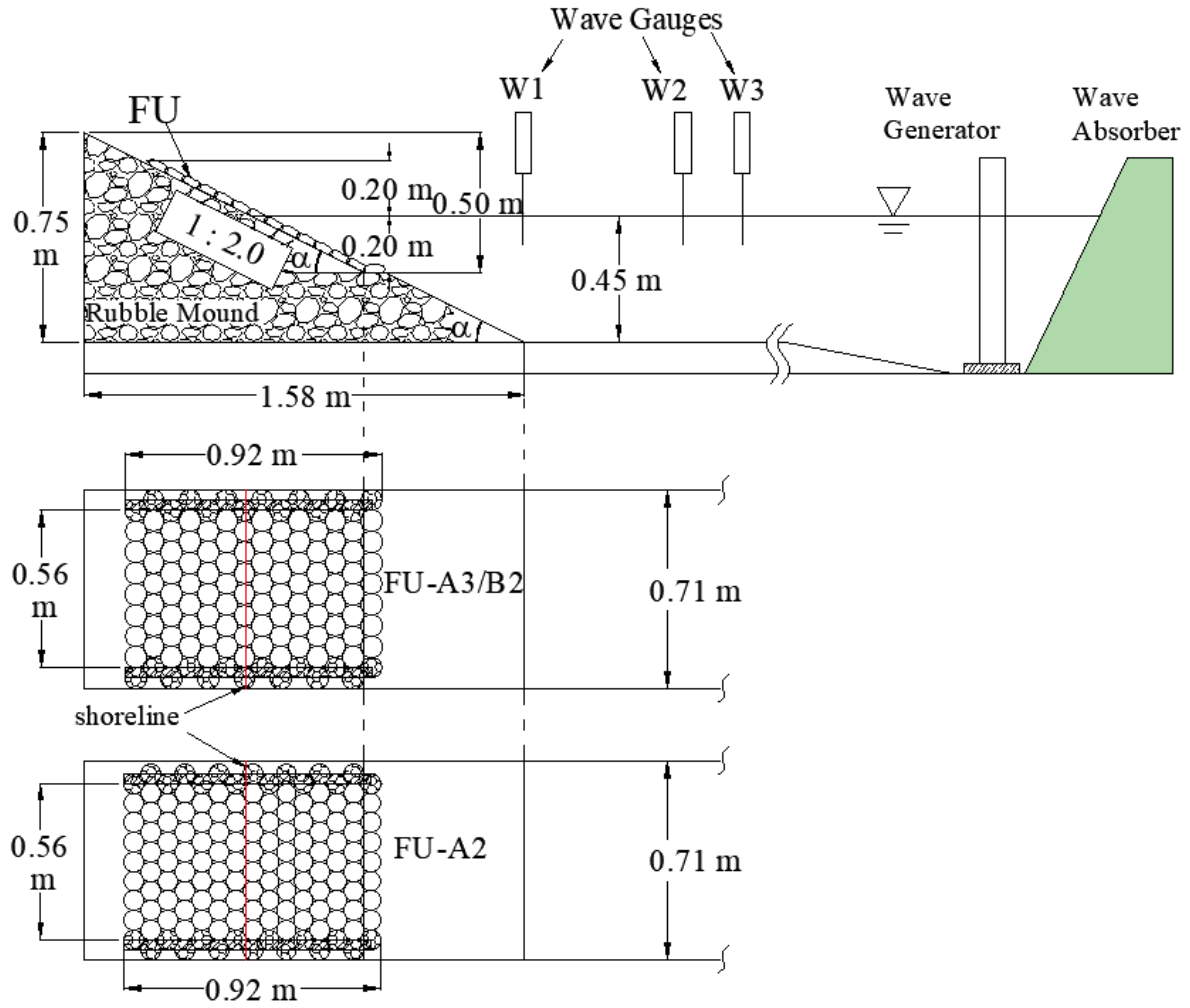
Figure 3. 4 Multiple-FU experimental setup (with lateral control)

3.4.2.2 Experimental Conditions and Test Procedure

The irregular wave experiments were also started with small amplitude waves, and the wave height was gradually increased without rearranging the FU models and without rebuilding the rubble mound slope. The test conditions are given in Table 3. 4. The test procedure in this multiple-FU experiment was repeated, and the experimental results were compared.

Table 3. 4 Multiple-FU experimental conditions

Model Scale	1/40
Water depth (h)	45 cm
Irregular waves	Modified Bretschneider-Mitsuyasu wave spectrum
Wave period $T_{1/3}$	1.0 sec, 1.5 sec, 2.0 sec
Wave height $H_{1/3}$	5 cm ~ 10 cm
Number of waves for each wave height rank	Approx. 1000
FU model: mass density	125 g 2.6 g/cm3

3.5 EXPERIMENTAL RESULTS AND DISCUSSION

3.5.1 Single-FU Experiment

The movement of all FU models was examined in both horizontal and vertical plane. The FU damage for this Single-FU experiment was defined as when half of the FU's diameter had moved into the lee side of the rubble mound.

The horizontal displacements of the FU models were measured from the seaward edge of flat portion of the fixed rubble mound after each case with different wave height, and the critical wave height that caused the FU damage as per the definition was recorded. Then, vertical displacement was measured from the initial position's top of the individual models on the fixed rubble mound surface.

(a)

(b)
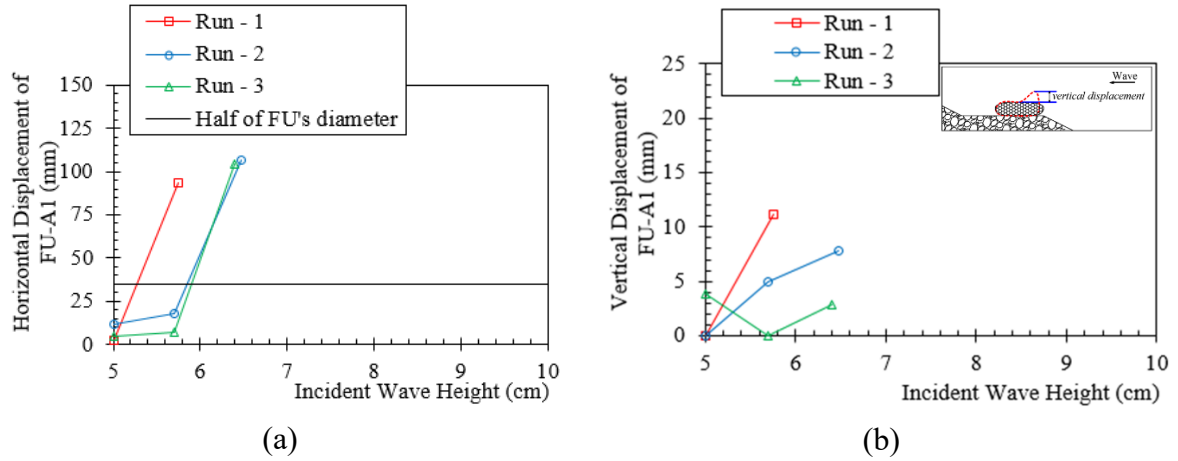
Figure 3. 5 Variation in horizontal and vertical displacements of FU-A1 during each experimental run
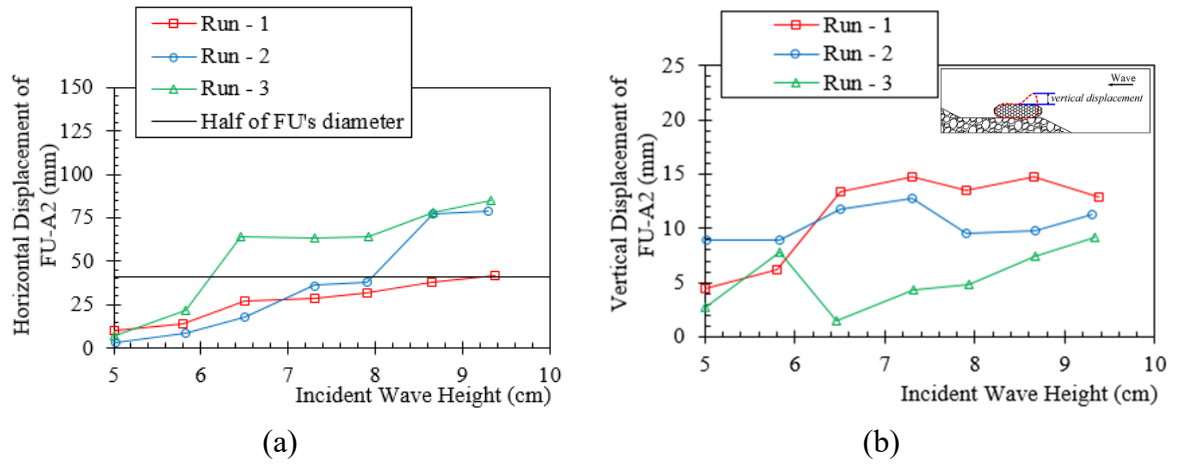

(a)

(b)

Figure 3. 6 Variation in horizontal and vertical displacements of FU-A2 during each experimental run

Each FU model was tested three times by repeating same conditions in order to check the variability of the results, namely Run-1, Run-2 and Run-3. Figures (3. 5 ~ 3. 12) show the horizontal and vertical displacements of the FU models as function of incident wave height and in the graphs showing the horizontal displacement, the horizontal line indicates half of the FU's diameter. FU-A1 had moved more than half of its diameter during small wave height attack (Figure 3. 5), and the wave height which caused the FU damage was denoted as its critical wave height.

In Figure 3. 6, the movement of FU-A2 reached the horizontal line after the final wave height attack in first-run case, and in Run-2, the FU-A2 was displaced more than half of

53

its diameter by waves of 8.67 cm-incident wave height. In Run-3 case, the critical wave height of the FU-A2 was lower than that of the previous cases, and the vertical A2 displacement of the Run-3 experienced a significant change due to the waves of the critical wave height.
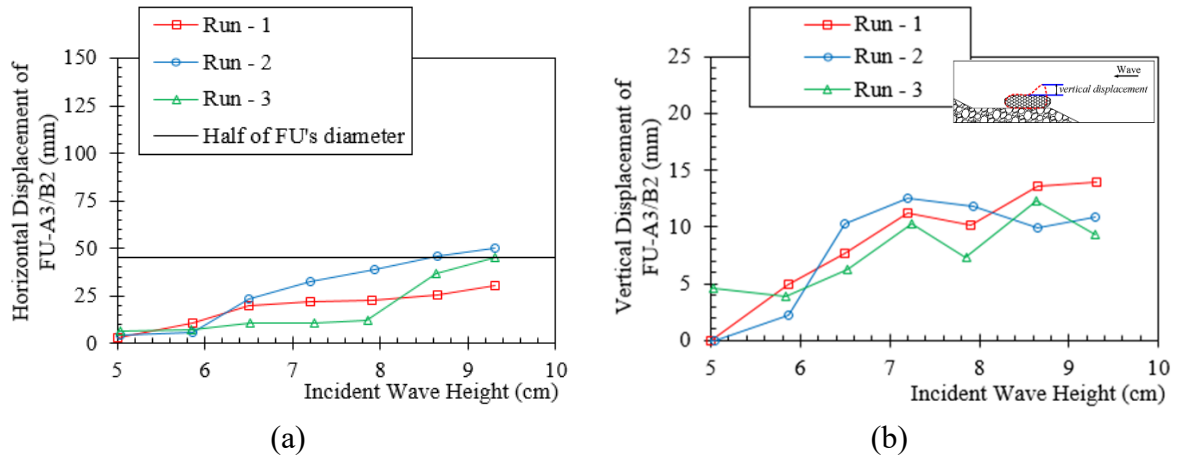

(a)   (b)

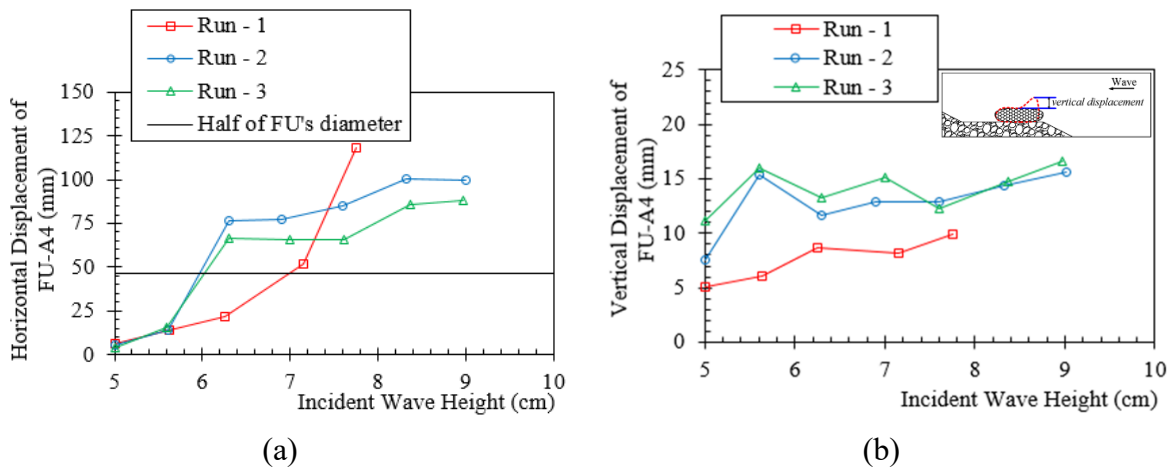Figure 3. 7 Variation in horizontal and vertical displacements of FU-A3/B2 during each experimental run

(a)   (b)

Figure 3. 8 Variation in horizontal and vertical displacements of FU-A4 during each experimental run

In Figure 3. 7, the horizontal movement of FU-A3/B2 did not exceed the horizontal line in first run, meaning that the FU was not damaged until the maximum wave height generated. However, in Run-2, the FU-A3/B2 had moved more than half of its diameter during 8.65 cm wave attack, and in last run, the critical wave height of the FU-A3/B2 was 9.34 cm. In the case of FU-A4 (Figure 3. 8), overall the FU's stability was low compared to the FU-A2 and

54

A3/B2, and the FU damage of Run-2 and Run-3 was observed during the wave attack of wave height around 6.3 cm.
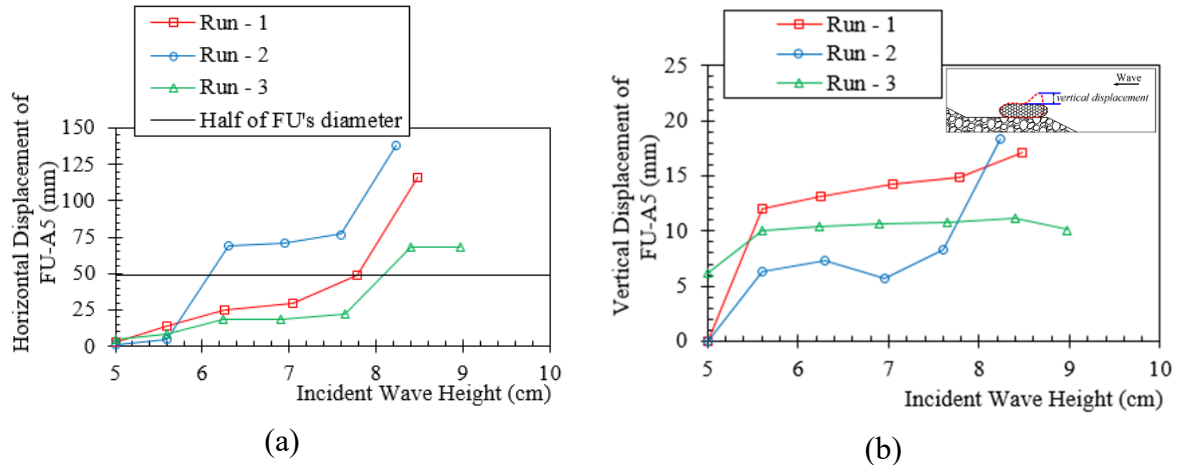

Figure 3. 9 Variation in horizontal and vertical displacements of FU-A5 during each experimental run
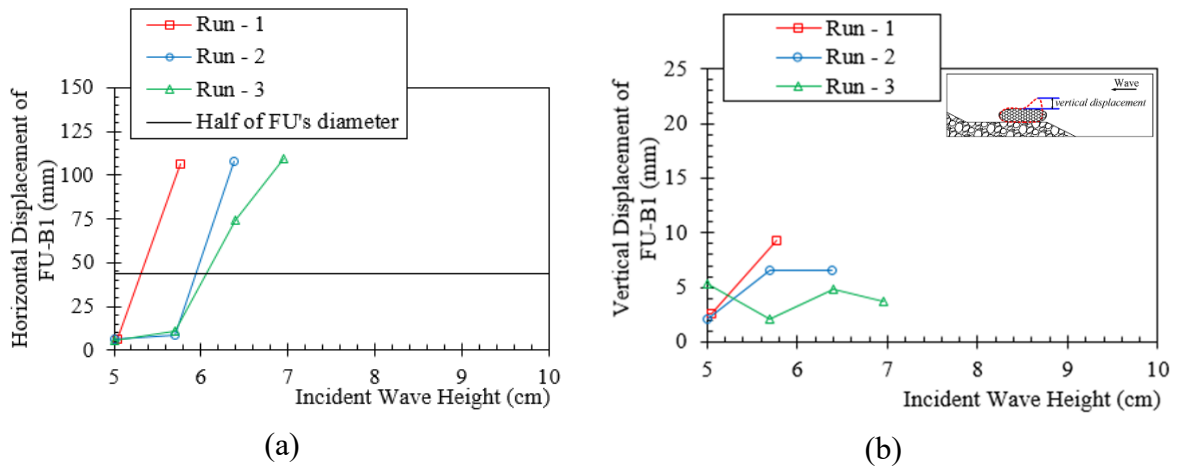

Figure 3. 10 Variation in horizontal and vertical displacements of FU-B1 during each experimental run

In FU-A5 having the ratio of model diameter to height of 5.0 (the flattest unit) as shown in Figure 3. 9, its horizontal displacement from the seaward edge of the rubble mound was relatively lower than the FU-A4, but its stability was not increased in comparison to the FU-A2 and A3/B2. FU-B1 having the shortest constraining rope inside damaged during small amplitude wave attack similar to the FU-A1 (Figure 3. 5 & 3. 10). In FU-B3 (Figure 3. 11), its ratio of constraining rope length to model height was 1.6 (Table 3. 3), and according to its

displacement graphs the B3 FU was more effective in stability than the B1 with the ratio of constraining rope length to model height of 0.7, but not as stable as the A3/B2. FU-N which is the conventional FU type widely used for river protection works, showed displacement to the onshore side by deforming throughout the all wave attack (Figure 3. 12).
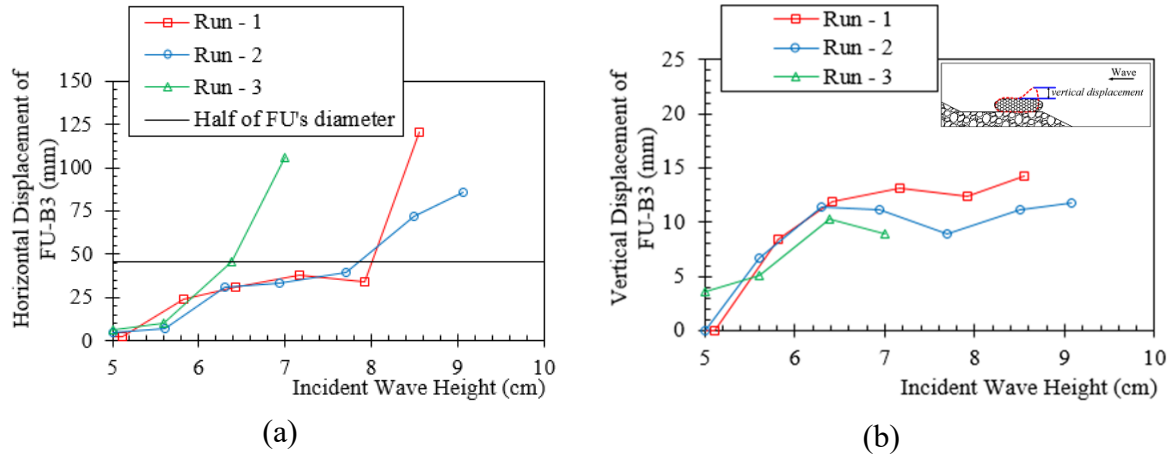

(a)   (b)

Figure 3. 11 Variation in horizontal and vertical displacements of FU-B3 during each experimental run

(a)   (b)
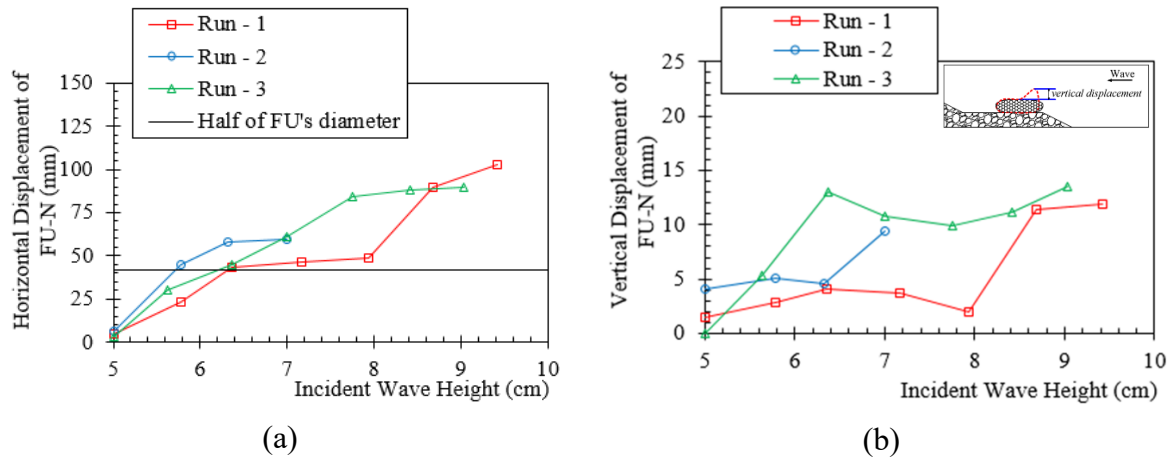
Figure 3. 12 Variation in horizontal and vertical displacements of FU-N during each experimental run

The critical wave heights of (Group A) FUs and (Group B & N-type) FUs are shown in Figure 3. 13 (a) and (b) respectively. In Group A (Figure. 3. 13 (a)), A1 had the lowest stability, A4 was a little bit higher than the A1 in stability, and A5 was more stable than the A1 and A4. FU-A3/B2 showed the highest stability, and the stability of A2, which was slightly

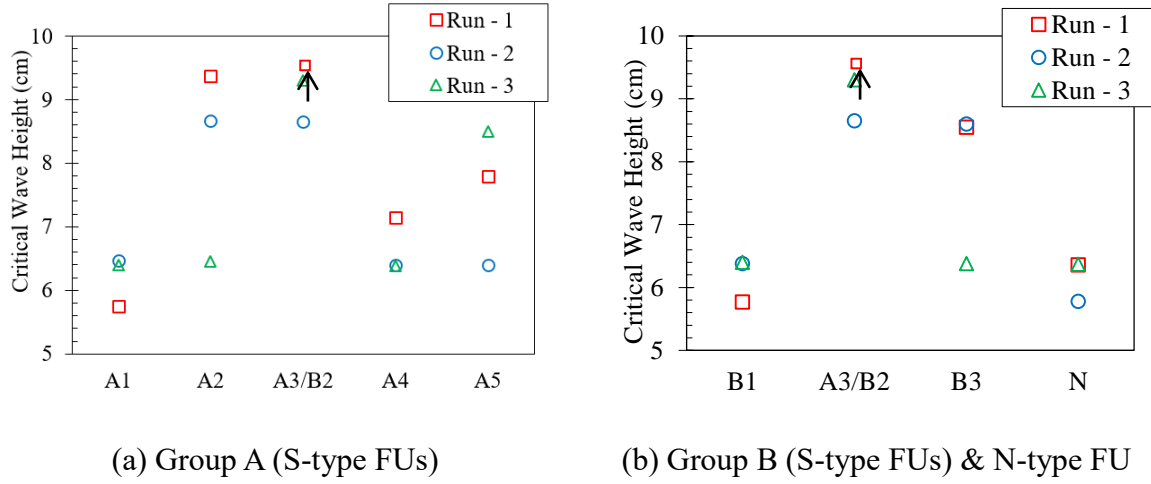lower than that of the A3/B2, was higher than that of the A1, A4 and A5.

(a) Group A (S-type FUs)   (b) Group B (S-type FUs) & N-type FU

Figure 3. 13 Comparison of critical wave heights of experimental FU models (on fixed mound surface)

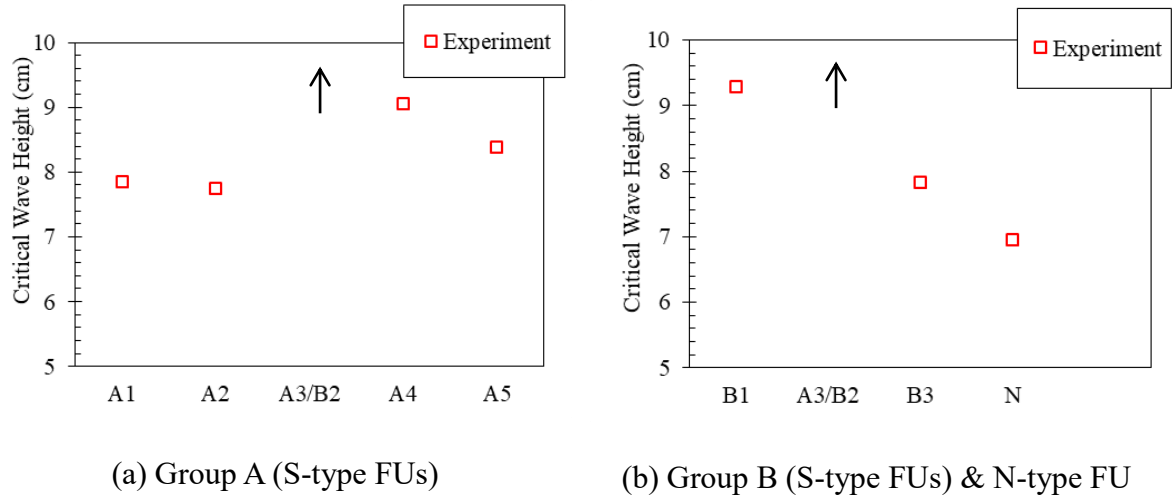(a) Group A (S-type FUs)   (b) Group B (S-type FUs) & N-type FU

Figure 3. 14 Comparison of critical wave height (on original mound surface)

In Group B (Figure 3. 13 (b)), A3/B2, having the constraining rope length of 28 mm, proved more stable than B1 and B3. In comparison, FU-A3/B2 (S-type FU) was more stable than N-type FU. The average critical wave height of the FU-A2 exceeded that of the B1, B3 and N. Thus, the FU-A3/B2 was the most effective FU structure among all the FU models tested under these experimental conditions, and the FU-A2 was the second most effective FU structure.

Figure (3. 14) gives the stability conditions of the FU models tested on original rubble mound surface, but in these cases scouring around the model occurred particularly during large amplitude wave action. Despite of some difference in experimental results (Figures 3. 13 & 3. 14), A3/B2 FU was still the most stable structure type among the tested models.

Regarding damage mechanism of FUs on this fixed rubble mound surface subjected to the regular waves, N-type FU moved to the lee side of the rubble mound, causing only a deformation during the wave attack (Figure 3. 15 (C)), and the damage pattern of FU-A1 followed a rotational movement (Figure 3. 15 (A)). The other S-type FUs: A2, A3/B2, A4, A5, B1 and B3 showed significant lateral movements of stuffing stones on the seaward side of constraining rope (Figure 3. 15 (B)), and depending on their structure it was found moved to the lee side through deformation or overturning. Some of the units (especially A3/B2) could withstand the overturning effect, that means the vertical line through the center of gravity of the whole unit was within its base of support. The stability of the FU depends not only on the location of its center of gravity but also on its supporting base (Figure 3. 16).
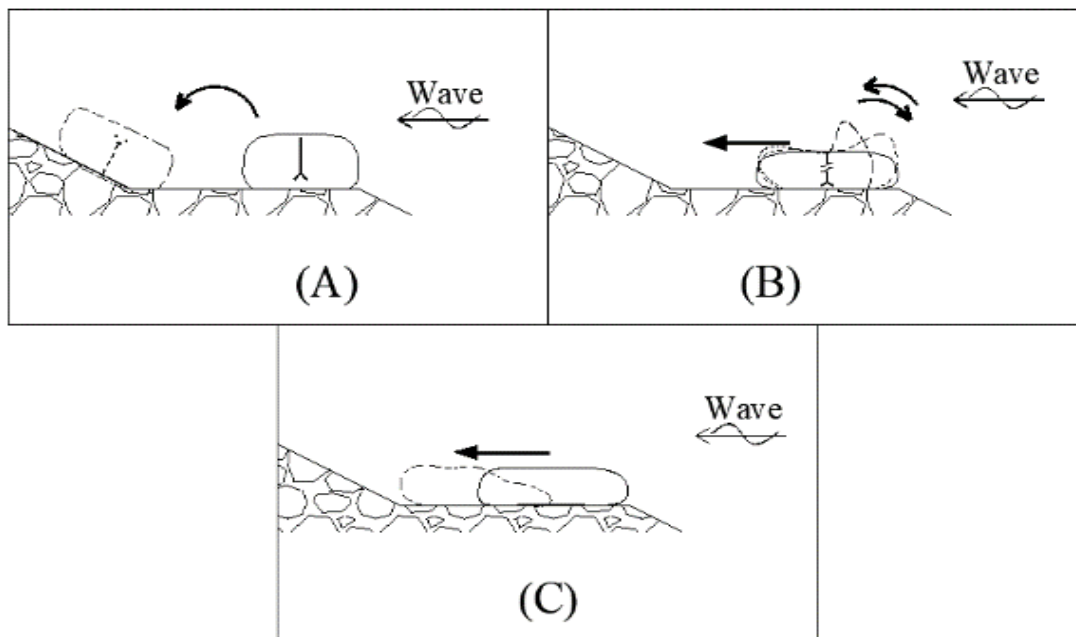

Figure 3. 15 Sketch of damage patterns of FUs

Stone movement inside the net generated by wave action, which led to the FU displacement, can be controlled by the constraining rope (Kubota et al., 2003). By comparing B1, A3/B2 and B3 having different constraint degree with the same volume ratio of filter net

to filling stones, B1 with short constraining rope turned over even during small wave height attack, but B3 with long constraining rope was more stable than B1. In A3/B2 type, its rope length for the restraint of filling stones was more effective for the stability than B1 and B3 (Figure 3. 13 (b)).

In Group-A FUs having the same constraining rope length, but different volume ratios (of filter bag/filling stones), A1, the most compact type, had the lowest stability, and as in Figure 3. 13 (a), on average the stability was higher with increasing volume ratio and reached a peak at A3/B2. After this, the graph showed a decline in critical wave height.

Therefore, it could be judged that the hydraulic stability of an S-type FU depends not only on its constraint degree but also on its volume ratio (of filter net/ stuffing stones).
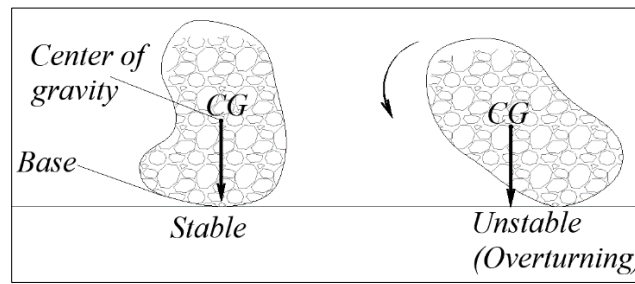
Figure 3. 16 (Sketch) CG and supporting base of an FU

3.5.2 Multiple-FU Experiment

The stability number (Ns) of the FUs was evaluated using the Brebner-Donnelly formula (2.2), described in Chapter 2, for all the experimental cases. Along with that, the FU damage was studied by evaluating the number of FUs moved from the initial position (DR_M) and by measuring the uncovered area (DR_U) after each wave height rank attack. The damage criteria for the single-layer flat placing of the FUs need to be strict because after the FU displacement, the under-layer of rubble mound will directly be exposed to waves, which can be followed closely by a sudden failure of the mound during severe wave action.

The movement of FU (M_{FU}) was investigated as shown in Figure 3. 17, measuring the horizontal displacement from center to center of the FU before and after the wave attack

and dividing the displacement by its initial diameter (*d*). Then the FU damage ratio in movement (DR$_M$ (%)) was estimated in detail as shown in the following graphs where; ≥0.1d represents the number of FUs dislocated ≥10% of their initial diameter in percentage (see equation: 3.1), ≥0.2d represents the number of FUs dislocated ≥20% of their initial diameter in percentage, and so on. The damage ratio of uncovered area (DR$_U$ (%)) was estimated approximately based on focus area as shown in equation (3. 2), and the gaps between the FUs placement were neglected.

$$M_{FU} = \frac{|x_2 - x_1|}{FU's\ initial\ diameter\ (d)}$$
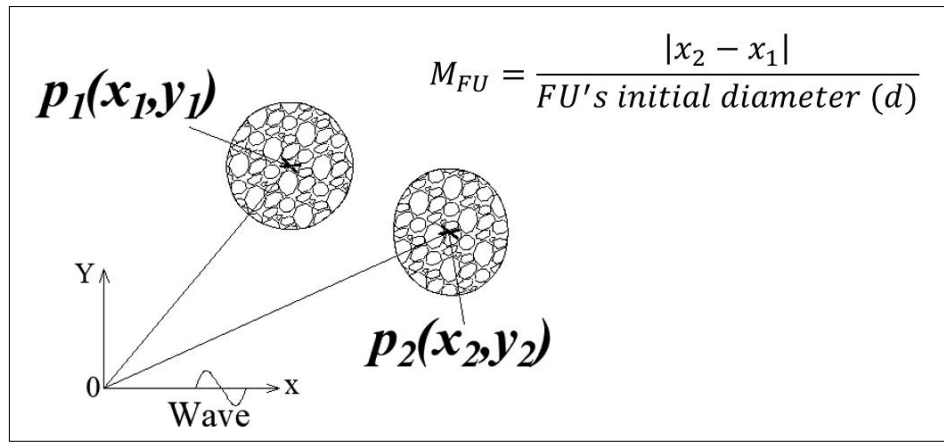
Figure 3. 17 Sketch for FU movement (*M$_{FU}$*) estimation

$$\geq 0.1d = \frac{No.of\ FUs\ dislocated\ \geq 10\%\ of\ their\ initial\ diameter\ (d)}{Total\ number\ of\ FUs\ focused} \qquad (3.1)$$

$$DR_U = \frac{Uncovered\ area\ (around\ the\ FUs\ displaced)}{Focus\ area} \qquad (3.2)$$

The stability of FU-A3/B2 type under the condition of no lateral control (Figure 3. 3) subjected to irregular waves is shown in Figures (3. 18~3. 20), in which its stability numbers are plotted with corresponding damage ratios (DR$_M$ & DR$_U$), and the focused area in this case was 85 cm x 71 cm. The initial covered area of the FUs was 85% of the focused area (85 x 71

cm). In Tables (3. 6~3. 8), the FUs' stability number considering no damage condition in terms of FU movement ratio and uncovered area ratio are given. In terms of DR_M (%), (≥0.5d) Ns^* means stability number with no damage if the damage definition was considered as when the FUs had dislocated ≥0.5d from their initial position. In terms of DR_U (%), (5%) Ns is the stability number of the FUs which had the uncovered area ratio of 5 %. Table 3. 5 gives the damage ratio values for the case of one unit being dislocated: DR_M and DR_U.

Table 3. 5 Damage ratios for the case of one unit (A3/B2-type) being displaced

FU-A3/B2 type	
DR_M (1FU) (%)	0.85
DR_U (1FU) (%)	0.73

Small damage ratio values in both DR_M and DR_U were found in '1.0 sec-cases' (Figure 3. 18), where the uncovered area ratios of first run and second run were just around 2 % and 1 % after the complete tests, and in these cases, one or two units were damaged conforming to Table 3. 5. If the damage definition in movement DR_M was taken as ≥0.5d and ≥0.6d, Ns* would be around 1.30 (1.1 % DR_U) and ≥1.64 (2.1 % DR_U), respectively in first run, but in second run, no damage occurred until the final wave height rank.

In '1.5 sec-cases' (Figure 3. 19), the FU-A3/B2 type's damage ratios (% of DR_M and DR_U) were substantially higher than those of the '1.0 sec-cases'. If the critical damage condition of the FUs was taken as ≥0.6d (in DR_M), Ns* of the FUs obtained would be 1.10 in first run (& 1.32 in second run), having the uncovered area ratio of 1.8 % in first run (& less than 2 % in second run). If the damage definition was determined as when the FUs moved more than one diameter, Ns* would be still 1.10 in first run (1.49 in second run) and the uncovered area ratio would be still 1.8 % in first run (& around 2 % in second run). However, in these '1.5 sec-cases', most of the FUs rolled down the slope during the attack of largest amplitude waves generated, and as a result the uncovered area ratio became very large at once. Thus, the uncovered area ratio reached 9.7 % at Ns≈1.66 in first run, but 5.2 % at Ns≈1.80 in second run, and this different result may be because the second test was started by applying to the structure with smaller amplitude waves.

In '2.0 sec-cases', a huge number of FUs had oscillated: more than 55 % of $\geq 0.1d$ in DR_M was observed after the complete test (Figure 3. 20), and the uncovered area ratios of first run and second run reached 7.7 % and 6.1 % respectively. If the FU damage was considered when as $\geq 0.6d$ or $\geq 1.0d$ (in DR_M), Ns^* of these FUs would be 1.25 in both first run and second run, having the uncovered area ratio of around 2.2 % in first run (almost the same condition: 2.3 % in second run).

The FU damage ratios (% of DR_M & DR_U) resulted from the 1.5 sec & 2.0 sec cases were notably bigger than the damage ratios of the 1.0 sec-cases. Although there was a considerable increase in the damage ratio of FU movement (% of DR_M), a slight increase in uncovered area ratio value (% of DR_U) was observed during these experimental runs. The damage level determined considering uncovered area ratio would be practical because the uncovered area ratio is directly related to the protection of under-layer of rubble mound (the exposure of under-layer to striking waves).

In these experimental cases, the FUs had moved not only up and down of the rubble mound slope but also left and right due to the wave action. The FUs' damage ratio in movement (DR_M %) was calculated based on their initial diameter, and the measurement of FU's dislocation was carried out only in up and down direction. Overall similar results were found out in the first and second runs. In '1.5 sec-cases', the FUs (A3/B2 type) generally moved in rolling down the rubble mound slope, and in '2.0 sec-cases', most of the FUs displaced by sliding down.

Then, in order to make a comparison of A3/B2 type and A2 type especially in terms of uncovered area FU damage ratio, the same focus area for both types was decided based on their dimensions as illustrated in Figure 3. 4, in which one row of FUs was added at the bottom in order to support the FU slope on rubble mound, and steel plates were used at both ends in order to control the transverse movement of the FUs due to wave action.
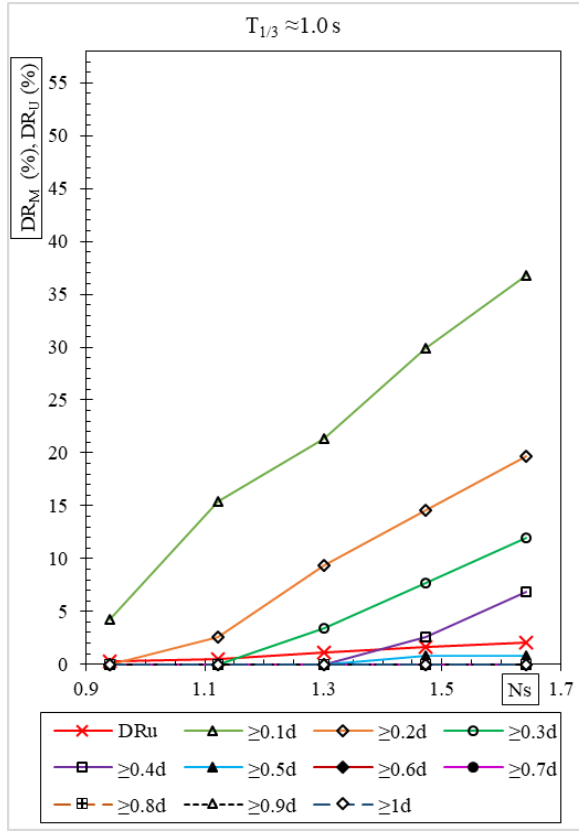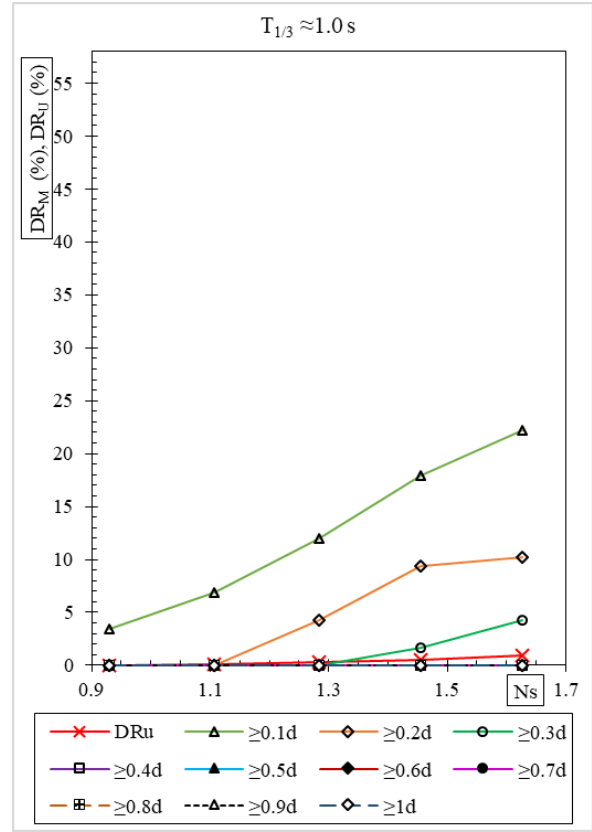
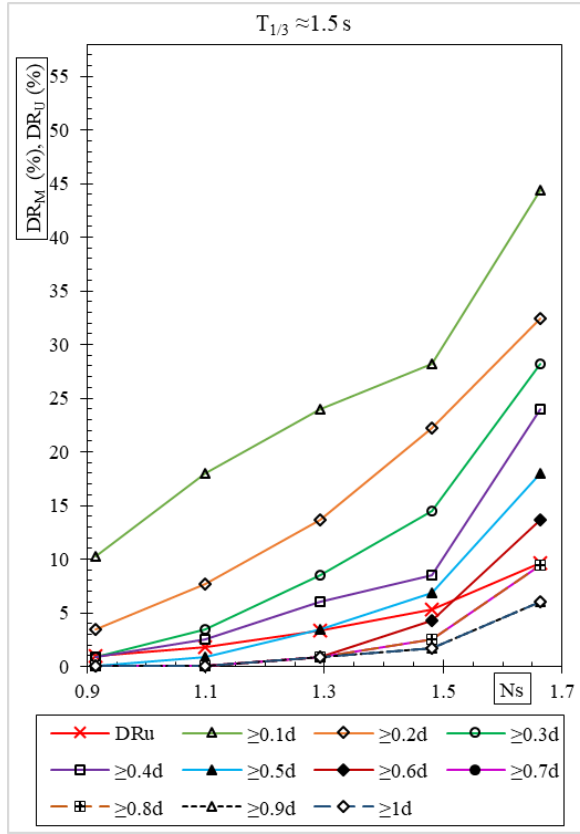(a) FU-A3/B2 type – First Run   (b) FU-A3/B2 type – Second Run

Figure 3. 18 (FU-A3/B2 type) 1.0 second wave period cases

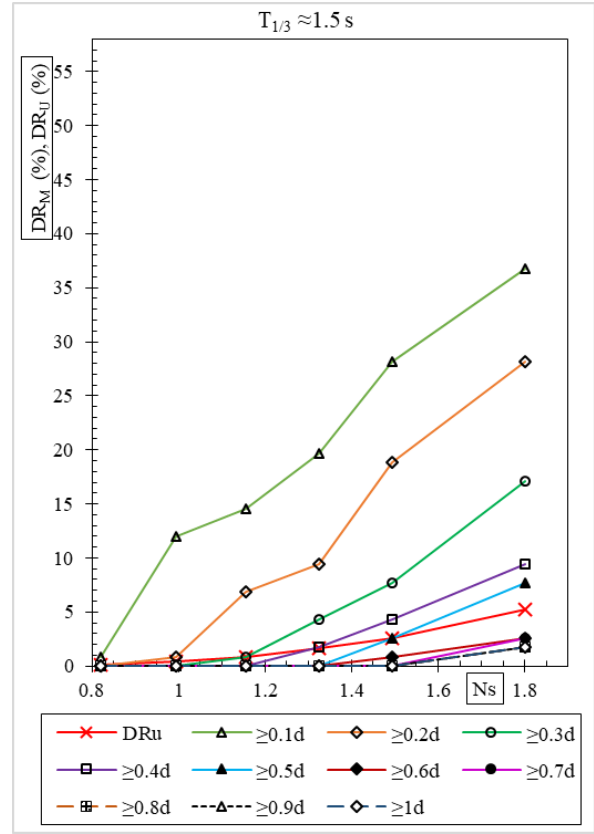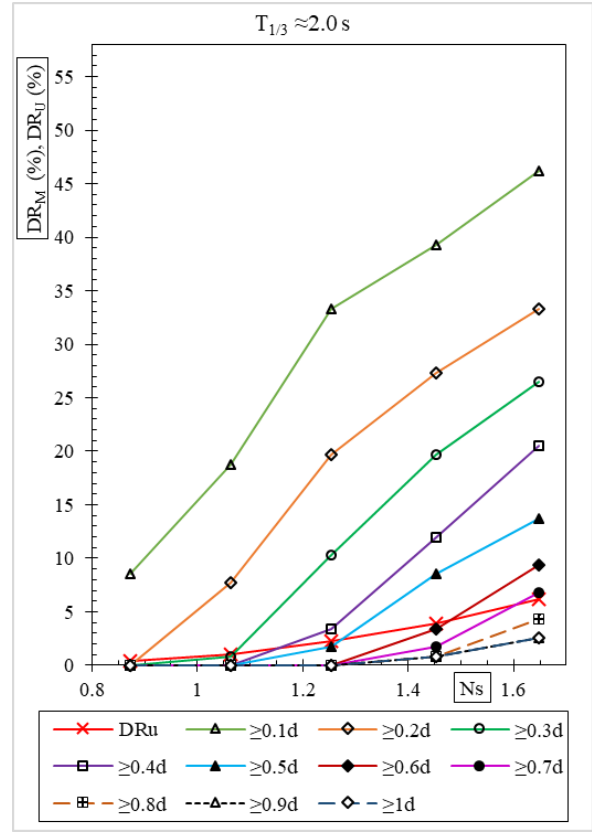Table 3. 6 Stability Number of A3/B2-type with no damage (1.0 sec)

(a) First Run		(b) Second Run	
In terms of DR_M (%)	In terms of DR_U (%)	In terms of DR_M (%)	In terms of DR_U (%)
($\geq$0.1d) Ns^*<0.94	(1.1%) Ns≈1.30	($\geq$0.1d) Ns^*<0.93	(0.9%) Ns≈1.63
($\geq$0.2d) Ns^*≈0.94	(2.1%) Ns≈1.64	($\geq$0.2d) Ns^*≈1.11	(2%) Ns$\geq$1.63
($\geq$0.3d) Ns^*≈1.12	(3%) Ns$\geq$1.64	($\geq$0.3d) Ns^*≈1.28	(3%) Ns$\geq$1.63
($\geq$0.4d) Ns^*≈1.30	(4%) Ns$\geq$1.64	($\geq$0.4d) $Ns^*$$\geq$1.63	(4%) Ns$\geq$1.63
($\geq$0.5d) Ns^*≈1.30	(5%) Ns$\geq$1.64	($\geq$0.5d) $Ns^*$$\geq$1.63	(5%) Ns$\geq$1.63
($\geq$0.6d) $Ns^*$$\geq$1.64		($\geq$0.6d) $Ns^*$$\geq$1.63	
($\geq$0.7d) $Ns^*$$\geq$1.64		($\geq$0.7d) $Ns^*$$\geq$1.63	
($\geq$0.8d) $Ns^*$$\geq$1.64		($\geq$0.8d) $Ns^*$$\geq$1.63	
($\geq$0.9d) $Ns^*$$\geq$1.64		($\geq$0.9d) $Ns^*$$\geq$1.63	
($\geq$1.0d) $Ns^*$$\geq$1.64		($\geq$1.0d) $Ns^*$$\geq$1.63	

($\geq$ ~ d) Ns^* – stability number with no damage in ($\geq$ ~ d) DR_M (%)

(1%) Ns – Stability number with the uncovered area ratio 1%

(a) FU-A3/B2 type First Run   (b) FU-A3/B2 type Second Run

Figure 3. 19 (FU-A3/B2 type) 1.5 second wave period cases

Table 3. 7 Displacement of A3/B2-type (1.5 sec)

(a) First Run		(b) Second Run	
In terms of DR_M (%)	In terms of DR_U (%)	In terms of DR_M (%)	In terms of DR_U (%)
(≥0.1d) Ns^*<0.91	(1%) Ns≈0.91	(≥0.1d) Ns^*<0.82	(0.8%) Ns≈1.16
(≥0.2d) Ns^*<0.91	(1.8%) Ns≈1.10	(≥0.2d) Ns^*≈0.82	(2%) 1.32<Ns<1.49
(≥0.3d) Ns^*<0.91	(3.3%) Ns≈1.29	(≥0.3d) Ns^*≈0.99	(3%) 1.49<Ns<1.80
(≥0.4d) Ns^*<0.91	(4%) 1.29<Ns<1.48	(≥0.4d) Ns^*≈1.16	(4%) 1.49<Ns<1.80
(≥0.5d) Ns^*≈0.91	(5.3%) Ns≈1.48	(≥0.5d) Ns^*≈1.32	(5.2%) Ns≈1.80
(≥0.6d) Ns^*≈1.10	(6%) 1.48<Ns<1.66	(≥0.6d) Ns^*≈1.32	(6%) Ns≥1.80
(≥0.7d) Ns^*≈1.10	(7%) 1.48<Ns<1.66	(≥0.7d) Ns^*≈1.49	(7%) Ns≥1.80
(≥0.8d) Ns^*≈1.10	(8%) 1.48<Ns<1.66	(≥0.8d) Ns^*≈1.49	(8%) Ns≥1.80
(≥0.9d) Ns^*≈1.10	(9%) 1.48<Ns<1.66	(≥0.9d) Ns^*≈1.49	(9%) Ns≥1.80
(≥1.0d) Ns^*≈1.10	(9.7%) Ns≈1.66	(≥1.0d) Ns^*≈1.49	(10%) Ns≥1.80

(≥ ~ d) Ns^* – stability number with no damage in (≥ ~ d) DR_M (%)

(1%) Ns – Stability number with the uncovered area ratio 1%
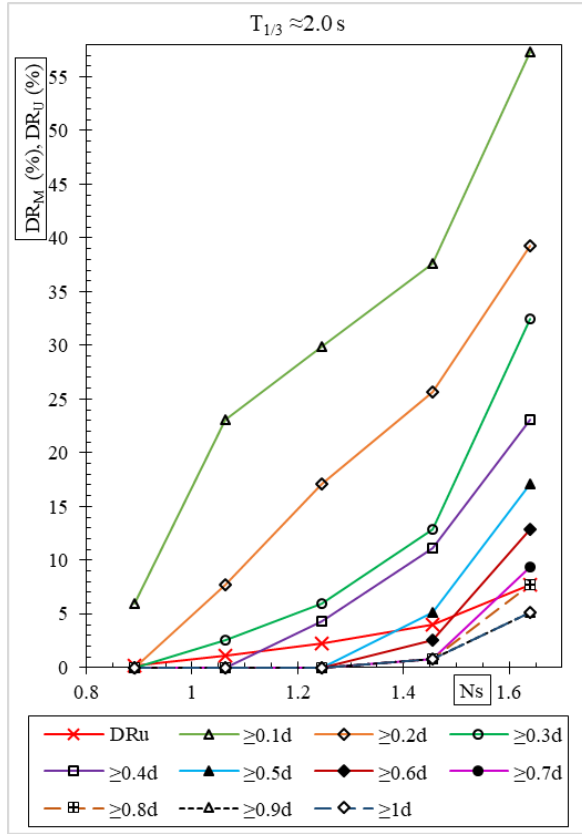
(a) (FU-A3/B2 type) – First Run   (b) (FU-A3/B2 type) Second Run

Figure 3. 20 (FU-A3/B2 type) 2.0 second wave period cases

Table 3. 8 Displacement of A3/B2-type (2.0 sec)

(a) First Run		(b) Second Run	
In terms of DR$_M$ (%)	In terms of DR$_U$ (%)	In terms of DR$_M$ (%)	In terms of DR$_U$ (%)
(≥0.1d) Ns*<0.89	(1.1%) Ns≈1.06	(≥0.1d) Ns*<0.87	(1%) Ns≈1.06
(≥0.2d) Ns*≈0.89	(2.2%) Ns≈1.25	(≥0.2d) Ns*≈0.87	(2.3%) Ns≈1.25
(≥0.3d) Ns*≈0.89	(3%) 1.25<Ns<1.45	(≥0.3d) Ns*≈0.87	(3%) 1.25<Ns<1.45
(≥0.4d) Ns*≈1.06	(4%) Ns≈1.45	(≥0.4d) Ns*≈1.06	(3.9%) Ns≈1.45
(≥0.5d) Ns*≈1.25	(5%) 1.45<Ns<1.64	(≥0.5d) Ns*≈1.06	(5%) 1.45<Ns<1.64
(≥0.6d) Ns*≈1.25	(6%) 1.45<Ns<1.64	(≥0.6d) Ns*≈1.25	(6.1%) Ns≈1.64
(≥0.7d) Ns*≈1.25	(7%) 1.45<Ns<1.64	(≥0.7d) Ns*≈1.25	(7%) Ns≥1.64
(≥0.8d) Ns*≈1.25	(7.7%) Ns≈1.64	(≥0.8d) Ns*≈1.25	(8%) Ns≥1.64
(≥0.9d) Ns*≈1.25	(9%) Ns≥1.64	(≥0.9d) Ns*≈1.25	(9%) Ns≥1.64
(≥1.0d) Ns*≈1.25	(10%) Ns≥1.64	(≥1.0d) Ns*≈1.25	(10%) Ns≥1.64

(≥ ~ d) Ns* – stability number with no damage in (≥ ~ d) DR$_M$ (%)

(1%) Ns – Stability number with the uncovered area ratio 1%

65

Similar to the previous experimental study, the stability and damage condition (DR_M (%) & DR_U (%)) of the FUs (A3/B2 and A2 types) due to wave action are shown in Figures (3. 21 ~ 3.26). The damage ratio of uncovered area (DR_U (%)) was estimated approximately based on focus area (92 cm x 56 cm) as shown in Figure 3. 4, and the gaps between the FUs placement were neglected. The initial covered area in percentage of the FUs that were not constrained, was around 84 % of the focused area (92 x 56 cm) for both A3/B2 and A2-type.

The damage ratio values (% of DR_M and % of DR_U) for the case of one-unit dislocation for both FU types are described in Table 3. 9: 0.85 for A3/B2 type and 0.75 for A2 type in percentage of uncovered area over the focused area. The stability numbers with no FU damage condition in terms of movement ratio and uncovered area ratio are given in Tables (3. 10 ~ 3. 15).

Table 3. 9 Damage ratios for the case of one-unit displacement

FU	A3/B2-type	A2-type
DR_M (1FU) (%)	1.02	0.89
DR_U (1FU) (%)	0.85	0.75

The stability numbers of first-run cases of FU-A3/B2 type under irregular waves are shown in Figures (3. 21 (a), 3.23 (a) & 3.25 (a)), plotted with the related damage ratios (DR_U & DR_M). In FU-A3/B2-type $T_{1/3}$=1.0 s-case, the FU which moved ≥0.7 of its diameter from its initial position, was not observed at Ns≈1.6. Similarly, in $T_{1/3}$=1.5 s-case, there were no FUs which dislocated ≥0.7 of its diameter, but the number of FUs damaged increased. In $T_{1/3}$=2.0 s-case, the number of the FU moved ≥1.0d was discovered as 1% after the maximum wave height attack. Comparing the graphs for wave periods of 1.0 s, 1.5 s and 2.0 s, DR_M increased significantly with longer wave periods, but a small increase in DR_U was observed. Moreover, DR_M and DR_U were compared at the end of the wave attacks to decide a critical condition for these first run cases of the FU-A3/B2 type. In short wave period (1.0 s-case), DR_U was almost the same as ≥0.5d in DR_M at Ns≈1.6, and the uncovered area ratio for $T_{1/3}$=1.5 s and 2.0 s cases became closer to ≥0.6d. If the FU damage was considered as when dislocation of ≥0.6d, the stability number Ns* with no FU damage would be around 1.45. In the repetition tests of the

FU-A3/B2 type (Figures: 3. 22 (a), 3.24 (a) & 3.26 (a)), similar results were found out except for wave period 1.5 s case. The 1.5 s case showed an outlier in which the significant damage in DR_M and uncovered area ratio (approximately 6% in DR_U) were found out being different from the previous case.

Figures (3. 21 (b), 3. 23 (b) & 3. 25 (b)) shows the stability number of FU-A2 type against its damage ratios (DR_U & DR_M). Likewise, the FU-A2 type experienced a significant increase in the number of FUs damaged in movement for long wave periods, and the uncovered area ratio was also increased to some extent. In comparison of the first-run graphs, DR_U (%) of FU-A2 for $T_{1/3}$=1.0 s after the maximum significant wave action was in the range of ≥0.4d and ≥0.5d in DR_M (%), and DR_U (%) for $T_{1/3}$=1.5 s and 2.0 s coincided with DR_M of ≥0.7d (%). If the critical damage definition for this FU type was when the FU had moved ≥0.7d from its initial position, the Ns* with no damage would be around 1.45 for $T_{1/3}$=2.0 s and around 1.3 for wave period 1.0 s and 1.5 s cases. These experiments were also repeated for each wave period, and the results showed similar behavior (Figures: 3. 22 (b), 3.24 (b) & 3.26 (b)).

Comparing the final conditions of FU-A3/B2 and FU-A2 at the end of the short-period wave attacks (first-run cases), DR_M for A2 type was lower than that of A3/B2 type, although DR_U values were approximately the same. In repeated tests, A2 type showed better stability than A3/B2 type. In the case of long wave period ($T_{1/3}$= 2.0 s), most of the FUs slid down the slope during the wave attack and the stability of A3/B2 type was comparatively higher than A2 type in uncovered area ratio. In all the long wave period tests, the A3/B2 type showed more stable than the A2 type. Regarding the graphs shown in Figures (3.23 (a) and (b)), the damage ratio of A3/B2 type was moderately lower than that of A2 type in the first runs of wave period 1.5 s. However, the damage rate for FU-A3/B2 type in the repeated experimental run was quite different.
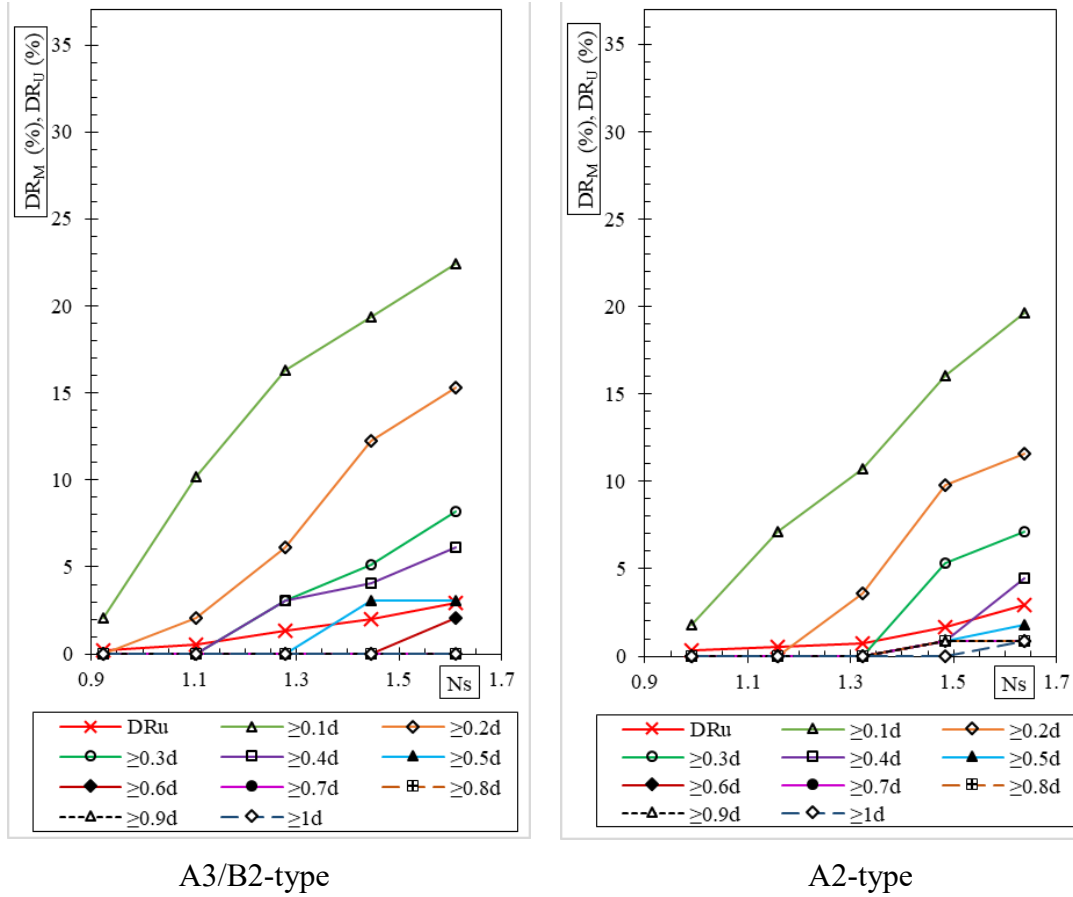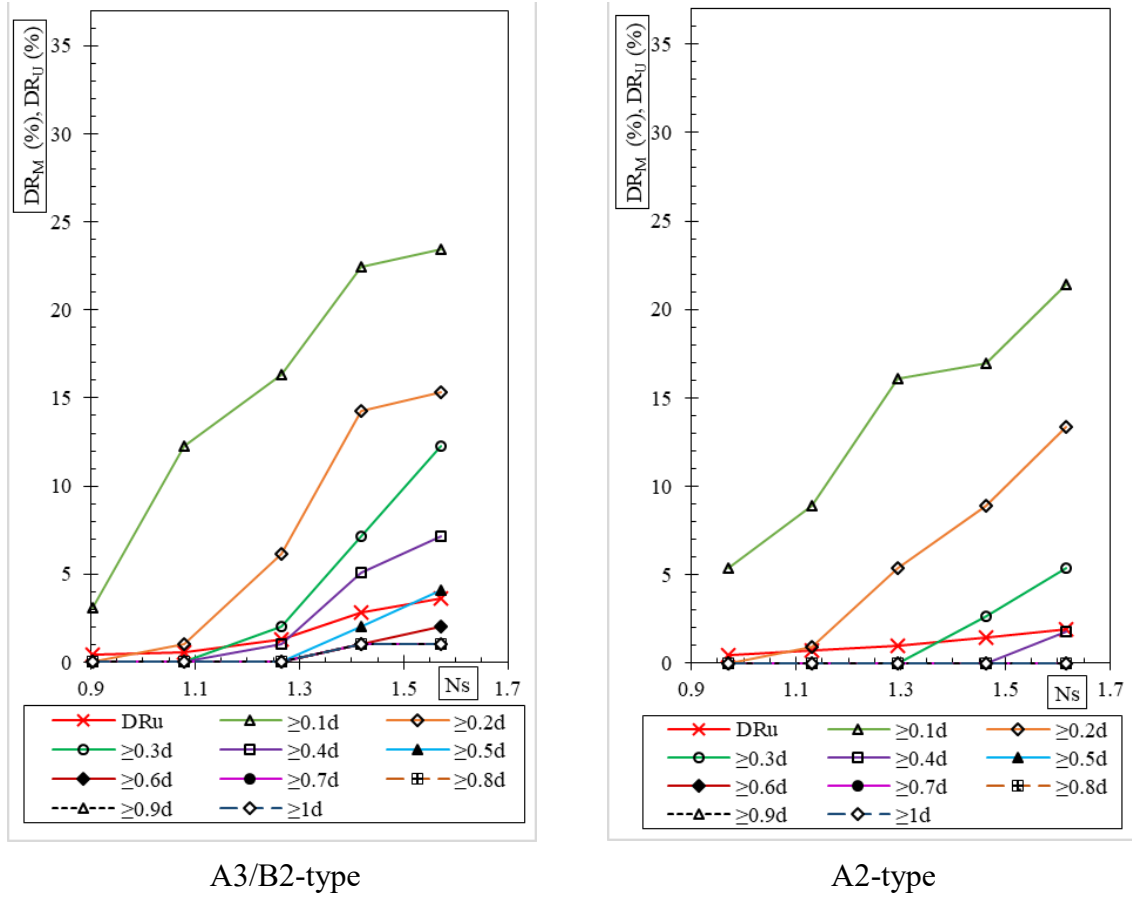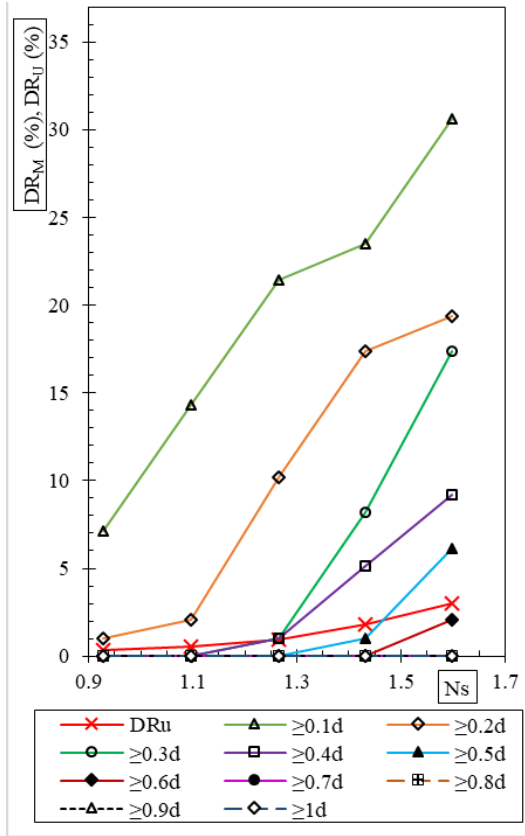
A3/B2-type   A2-type

Figure 3. 21 Comparison between A3/B2 and A2-type (1.0 sec, first run)

Table 3. 10 Comparison of A3/B2 and A2-type (1.0 sec, first run)

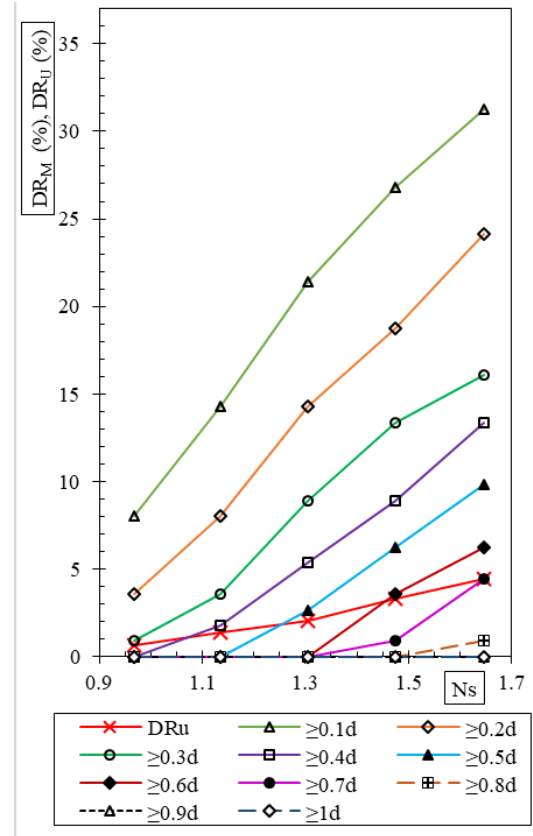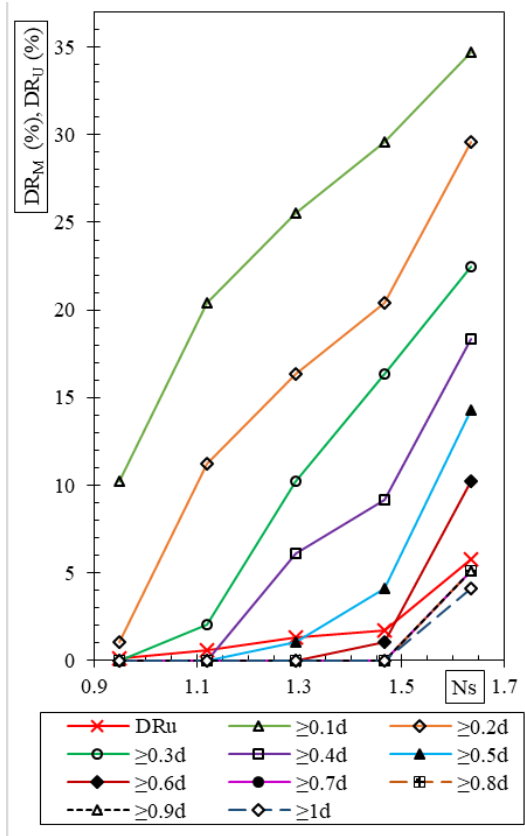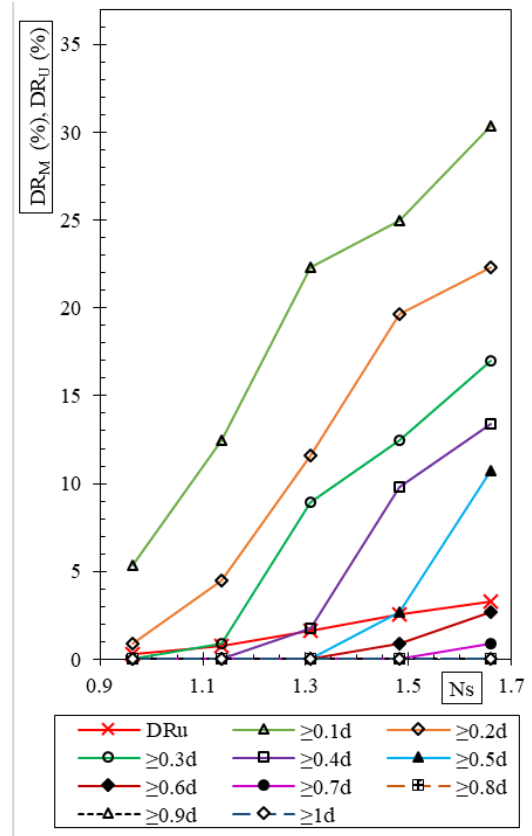| A3/B2-type		A2-type	
In terms of DR_M (%)	In terms of DR_U (%)	In terms of DR_M (%)	In terms of DR_U (%)
(≥0.1d) Ns^*<0.92		(≥0.1d) Ns^*<0.99	
(≥0.2d) Ns^*≈0.92		(≥0.2d) Ns^*≈1.16	
(≥0.3d) Ns^*≈1.10	(1%) 1.10<Ns<1.28	(≥0.3d) Ns^*≈1.32	(1%) 1.32<Ns<1.48
(≥0.4d) Ns^*≈1.10	(2%) Ns≈1.45	(≥0.4d) Ns^*≈1.32	(2%) 1.48<Ns<1.64
(≥0.5d) Ns^*≈1.28	(3%) Ns≈1.61	(≥0.5d) Ns^*≈1.32	(2.9%) Ns≈1.64
(≥0.6d) Ns^*≈1.45	(4%) Ns≥1.61	(≥0.6d) Ns^*≈1.32	(3%) Ns≥1.64
(≥0.7d) Ns^*≥1.61	(5%) Ns≥1.61	(≥0.7d) Ns^*≈1.32	(4%) Ns≥1.64
(≥0.8d) Ns^*≥1.61		(≥0.8d) Ns^*≈1.32	(5%) Ns≥1.64
(≥0.9d) Ns^*≥1.61		(≥0.9d) Ns^*≈1.32	
(≥1.0d) Ns^*≥1.61		(≥1.0d) Ns^*≈1.48	

(≥ ~ d) Ns^* – stability number with no damage in (≥ ~ d) DR_M (%)

(1%) Ns – Stability number with the uncovered area ratio 1%

A3/B2-type   A2-type

Figure 3. 22 Comparison between A3/B2 and A2-type (1.0 sec, second run)

Table 3. 11 Comparison of A3/B2 and A2-type (1.0 sec, second run)

A3/B2-Type		A2-Type	
In terms of DR_M (%)	In terms of DR_U (%)	In terms of DR_M (%)	In terms of DR_U (%)
(≥0.1d) Ns^*<0.90	(1%) 1.08<Ns<1.27	(≥0.1d) Ns^*<0.97	(1%) Ns≈1.29
(≥0.2d) Ns^*≈0.90	(2%) 1.27<Ns<1.42	(≥0.2d) Ns^*≈0.97	(1.9%) Ns≈1.62
(≥0.3d) Ns^*≈1.08	(3%) 1.42<Ns<1.57	(≥0.3d) Ns^*≈1.29	(2%) Ns≥1.62
(≥0.4d) Ns^*≈1.08	(3.6%) Ns≈1.57	(≥0.4d) Ns^*≈1.46	(3%) Ns≥1.62
(≥0.5d) Ns^*≈1.27	(4%) Ns≥1.57	(≥0.5d) Ns^*≈1.62	(4%) Ns≥1.62
(≥0.6d) Ns^*≈1.27	(5%) Ns≥1.57	(≥0.6d) Ns^*≈1.62	(5%) Ns≥1.62
(≥0.7d) Ns^*≈1.27		(≥0.7d) Ns^*≈1.62	
(≥0.8d) Ns^*≈1.27		(≥0.8d) Ns^*≈1.62	
(≥0.9d) Ns^*≈1.27		(≥0.9d) Ns^*≈1.62	
(≥1.0d) Ns^*≈1.27		(≥1.0d) Ns^*≥1.62	

(≥ ~ d) Ns^* – stability number with no damage in (≥ ~ d) DR_M (%)

(1%) Ns – Stability number with the uncovered area ratio 1%

69

A3/B2-type

A2-type

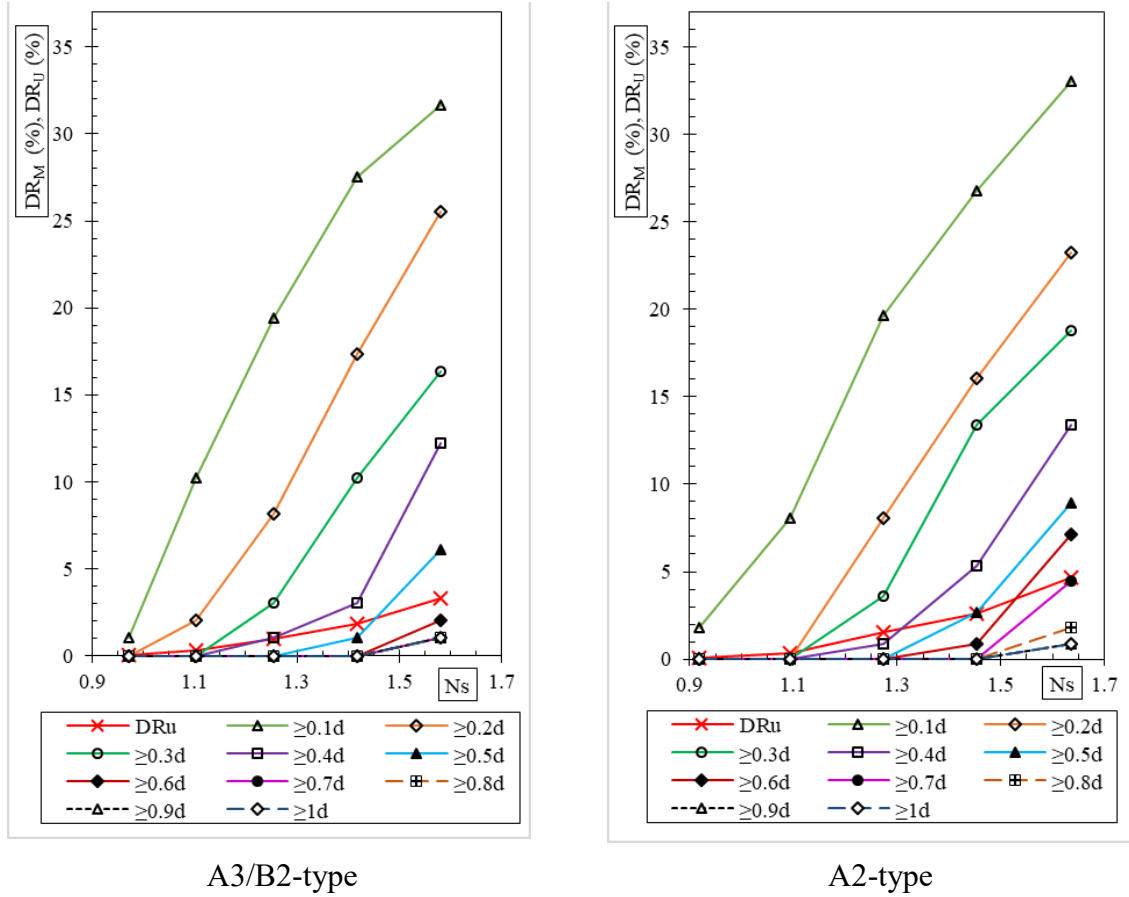Figure 3. 23 Comparison between A3/B2 and A2-type (1.5 sec, first run)

Table 3. 12 Comparison of A3/B2 and A2-type (1.5 sec, first run)

A3/B2-Type		A2-Type	
In terms of DR_M (%)	In terms of DR_U (%)	In terms of DR_M (%)	In terms of DR_U (%)
($\geq$0.1d) Ns^*<0.93	(1%) 1.27<Ns<1.43	($\geq$0.1d) Ns^*<0.97	(1%) 0.97<Ns<1.14
($\geq$0.2d) Ns^*<0.93	(2%) 1.43<Ns<1.60	($\geq$0.2d) Ns^*<0.97	(2.1%) Ns$\approx$1.30
($\geq$0.3d) $Ns^*\approx$1.10	(3%) Ns$\approx$1.60	($\geq$0.3d) Ns^*<0.97	(3%) 1.30<Ns<1.47
($\geq$0.4d) $Ns^*\approx$1.10	(4%) Ns$\geq$1.60	($\geq$0.4d) $Ns^*\approx$0.97	(4%) 1.47<Ns<1.65
($\geq$0.5d) $Ns^*\approx$1.27	(5%) Ns$\geq$1.60	($\geq$0.5d) $Ns^*\approx$1.14	(4.4%) Ns$\approx$1.65
($\geq$0.6d) $Ns^*\approx$1.43		($\geq$0.6d) $Ns^*\approx$1.30	(5%) Ns$\geq$1.65
($\geq$0.7d) $Ns^*\geq$1.60		($\geq$0.7d) $Ns^*\approx$1.30	
($\geq$0.8d) $Ns^*\geq$1.60		($\geq$0.8d) $Ns^*\approx$1.47	
($\geq$0.9d) $Ns^*\geq$1.60		($\geq$0.9d) $Ns^*\geq$1.65	
($\geq$1.0d) $Ns^*\geq$1.60		($\geq$1.0d) $Ns^*\geq$1.65	

($\geq$ ~ d) Ns^* – stability number with no damage in ($\geq$ ~ d) DR_M (%)

(1%) Ns – Stability number with the uncovered area ratio 1%
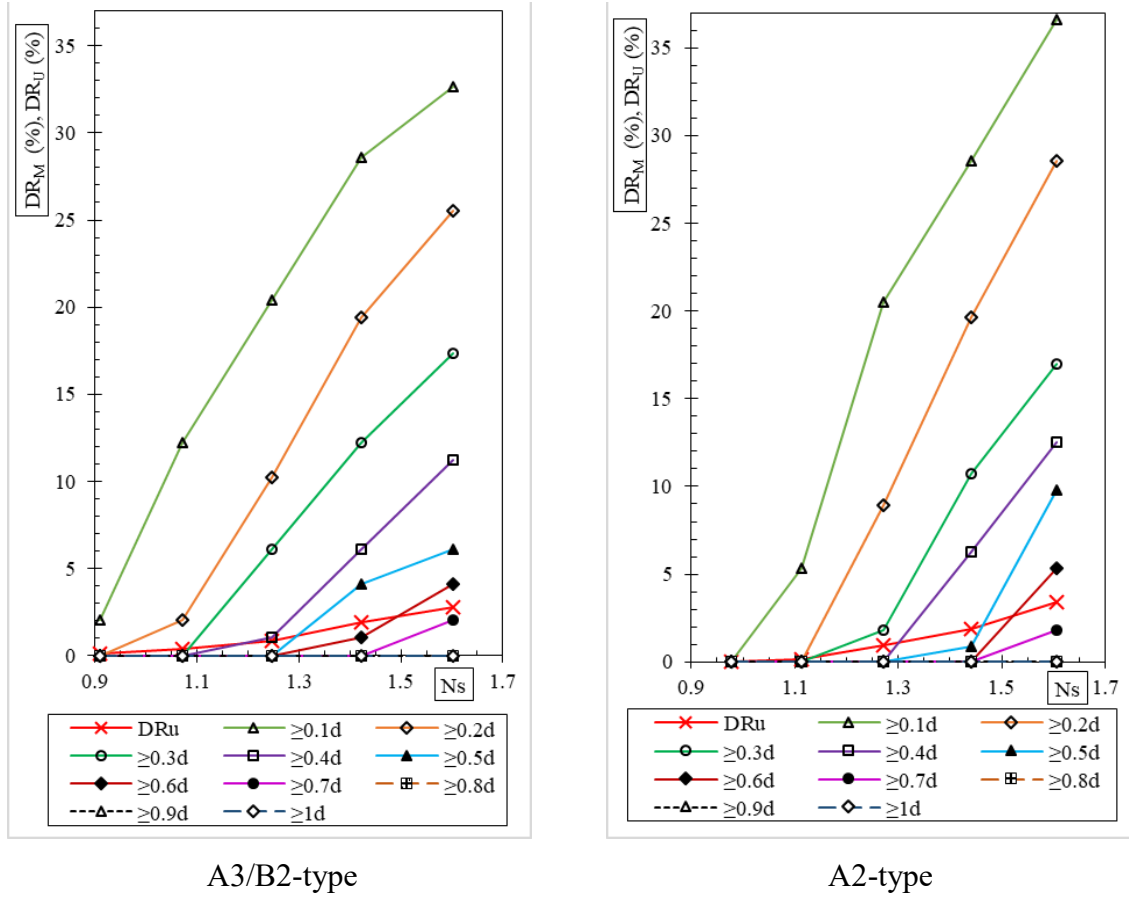
70

A3/B2-type   A2-type

Figure 3. 24 Comparison between A3/B2 and A2-type (1.5 sec, second run)

Table 3. 13 Comparison of A3/B2 and A2-type (1.5 sec, second run)

A3/B2-Type		A2-Type	
In terms of DR_M (%)	In terms of DR_U (%)	In terms of DR_M (%)	In terms of DR_U (%)
(≥0.1d) Ns^*<0.95	(1%) 1.12<Ns<1.29	(≥0.1d) Ns^*<0.96	(1%) 1.14<Ns<1.31
(≥0.2d) Ns^*<0.95	(2%) 1.47<Ns<1.63	(≥0.2d) Ns^*<0.96	(2%) 1.31<Ns<1.48
(≥0.3d) Ns^*≈0.95	(3%) 1.47<Ns<1.63	(≥0.3d) Ns^*≈0.96	(3%) 1.48<Ns<1.66
(≥0.4d) Ns^*≈1.12	(4%) 1.47<Ns<1.63	(≥0.4d) Ns^*≈1.14	(3.3%) Ns≈1.66
(≥0.5d) Ns^*≈1.12	(5%) 1.47<Ns<1.63	(≥0.5d) Ns^*≈1.31	(4%) Ns≥1.66
(≥0.6d) Ns^*≈1.29	(5.8%) Ns≈1.63	(≥0.6d) Ns^*≈1.31	(5%) Ns≥1.66
(≥0.7d) Ns^*≈1.47		(≥0.7d) Ns^*≈1.48	
(≥0.8d) Ns^*≈1.47		(≥0.8d) Ns^*≥1.66	
(≥0.9d) Ns^*≈1.47		(≥0.9d) Ns^*≥1.66	
(≥1.0d) Ns^*≈1.47		(≥1.0d) Ns^*≥1.66	

(≥ ~ d) Ns^* – stability number with no damage in (≥ ~ d) DR_M (%)

(1%) Ns – Stability number with the uncovered area ratio 1%

A3/B2-type   A2-type

Figure 3. 25 Comparison between A3/B2 and A2-type (2.0 sec, first run)

Table 3. 14 Comparison of A3/B2 and A2-type (2.0 sec, first run)

A3/B2-Type		A2-Type	
In terms of DR_M (%)	In terms of DR_U (%)	In terms of DR_M (%)	In terms of DR_U (%)
(≥0.1d) Ns^*<0.97	(1%) Ns≈1.25	(≥0.1d) Ns^*<0.92	(1%)
(≥0.2d) Ns^*≈0.97	(2%) 1.42<Ns<1.58	(≥0.2d) Ns^*≈1.09	1.09<Ns<1.27
(≥0.3d) Ns^*≈1.10	(3%) 1.42<Ns<1.58	(≥0.3d) Ns^*≈1.09	(2%)
(≥0.4d) Ns^*≈1.10	(3.3%) Ns≈1.58	(≥0.4d) Ns^*≈1.09	1.27<Ns<1.45
(≥0.5d) Ns^*≈1.25	(4%) Ns≥1.58	(≥0.5d) Ns^*≈1.27	(3%)
(≥0.6d) Ns^*≈1.42	(5%) Ns≥1.58	(≥0.6d) Ns^*≈1.27	1.45<Ns<1.64
(≥0.7d) Ns^*≈1.42		(≥0.7d) Ns^*≈1.45	(4%)
(≥0.8d) Ns^*≈1.42		(≥0.8d) Ns^*≈1.45	1.45<Ns<1.64
(≥0.9d) Ns^*≈1.42		(≥0.9d) Ns^*≈1.45	(4.7%) Ns≈1.64
(≥1.0d) Ns^*≈1.42		(≥1.0d) Ns^*≈1.45	(5%) Ns≥1.64

(≥ ~ d) Ns^* – stability number with no damage in (≥ ~ d) DR_M (%)

(1%) Ns – Stability number with the uncovered area ratio 1%

72

A3/B2-type   A2-type

Figure 3. 26 Comparison between A3/B2 and A2-type (2.0 sec, second run)

Table 3. 15 Comparison of A3/B2 and A2-type (2.0 sec, second run)

A3/B2-Type		A2-Type	
In terms of DR_M (%)	In terms of DR_U (%)	In terms of DR_M (%)	In terms of DR_U (%)
(≥0.1d) Ns^*<0.91	(1%) 1.25<Ns<1.42	(≥0.1d) Ns^*≈0.98	(1%) Ns≈1.27
(≥0.2d) Ns^*≈0.91	(2%) 1.42<Ns<1.60	(≥0.2d) Ns^*≈1.11	(2%) 1.44<Ns<1.61
(≥0.3d) Ns^*≈1.07	(2.8%) Ns≈1.60	(≥0.3d) Ns^*≈1.11	(3%) 1.44<Ns<1.61
(≥0.4d) Ns^*≈1.07	(3%) Ns≥1.60	(≥0.4d) Ns^*≈1.27	(3.4%) Ns≈1.61
(≥0.5d) Ns^*≈1.25	(4%) Ns≥1.60	(≥0.5d) Ns^*≈1.27	(4%) Ns≥1.61
(≥0.6d) Ns^*≈1.25	(5%) Ns≥1.60	(≥0.6d) Ns^*≈1.44	(5%) Ns≥1.61
(≥0.7d) Ns^*≈1.42		(≥0.7d) Ns^*≈1.44	
(≥0.8d) Ns^*≥1.60		(≥0.8d) Ns^*≥1.61	
(≥0.9d) Ns^*≥1.60		(≥0.9d) Ns^*≥1.61	
(≥1.0d) Ns^*≥1.60		(≥1.0d) Ns^*≥1.61	

(≥ ~ d) Ns^* – stability number with no damage in (≥ ~ d) DR_M (%)

(1%) Ns – Stability number with the uncovered area ratio 1%

73

CHAPTER 4

Chapter 4

NUMERICAL STUDY

OUTLINE

This chapter is allocated to explain numerical investigations of filter unit (FU) model deformation on rubble mound model due to wave-induced forces acting on the model. First, a brief introduction on simulation is given which is followed by presentation of objectives and scope as well as of numerical FU models. Then methodology, numerical procedure, comparison of water level variation resulted from CS2D with that of experiment and DEM input parameters are described. Afterwards, numerical results are presented.

4.1 INTRODUCTION

One of the significant characteristics of FU is that it is deformable, which is known to be related to the stability of the FU. However, how the FU deforms on rubble mound has not been examined numerically yet. In this study, a two-dimensional numerical model to represent the deformation of the FU is developed using circular finite-sized particles. The model includes two particle types: virtual rubble and virtual fiber, and the fiber particles are arranged like a string wrapping the rubbles. The deformation of the model on rubble mound structure under wave action is computed by a combination use of two numerical models: CADMAS-SURF/2D (CS2D) and Discrete Element Method (DEM/2D). The model input parameters are optimized for reproducing the flexible deformation of experimental FU models.

4.2 OBJECTIVES AND SCOPE

The main objectives of this numerical study are as follows:
1) To develop a discrete element model for simulating the deformation of the FU armoring a rubble mound structure due to wave motion,
2) To examine the simulation model's particle interaction behaviors and movement, and

3) To discuss the newly developed model in accord with some observations of physical experiments

In order to achieve these objectives, the input model parameters for DEM calculation which significantly affect the calculated results are required, and these parameters can be determined using either analytical assumption or inverse calibration methods (Sadek, 2013). In the former method, the input parameters are estimated from material properties such as Young's modulus, shear modulus and Poisson's ratio, and in the inverse calibration method, the parameters are assessed by matching the calculated results with experimental results.

Many researchers simulated rubble mound structure deformation by waves using DEM (Araki et al., 2001, 2002, Maeno et al., 2005, 2009 & Fukumizu et al., 2018), and Sadek (2013) mimicked the tensile test of hemp fiber using DEM. The governing equations used for rubble mound deformation under wave attack (Equations: 2.25~2.27) are modified for predicting the FU deformation in the present study by adding a parallel bond model as described in Chapter 2. The numerical models which represent the FUs are built up with virtual rubble and fiber particles, and the model input parameters required for the modified governing equations (Equations: 2.58~2.60) are determined based on the relevant previous researches as well as on some material properties available.
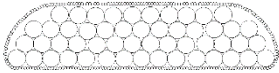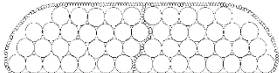
Wave forces acting on the numerical FU model are evaluated by Morison-type formula using the water particle velocity data from CS2D in which the waves are generated by Stokes theory of 5th order. Moreover, porosity adjustment, introduced by Maeno et al (2009), for rubble mound structure is applied. The model scale of the numerical FU model is 1/35, and the effect of fiber net structure on wave motion is not considered in this research.

4.3 NUMERICAL FU MODELS

One experimental model and numerical models are given in Table 4. 1, in which Model-I and Model-II represented N-type FU and S-type FU models, respectively. Numerical models included virtual fiber particles of 0.1 cm in diameter and virtual rubbles of 0.6 cm in diameter. The particles were arranged randomly based on the shape of the experimental model allowing small particle overlap. In the Model-II representing S-type FU, constraining rope inside the bag was modelled using 28 fiber particles. The diameter and height of these

numerical FU models were around 9.0 and 2.1 cm respectively.

Table 4. 1 Numerical FU Models

Models		No. of virtual fiber particles	No. of virtual rubble particles
Exp. FU model		-	-
Model-I		230	52
Model-II		258	52

4.4 METHODOLOGY

In the present study, the deformation of FU models on rubble mound structure due to regular waves was studied numerically using two dimensional CADMAS-SURF (CS2D) and Discrete Element Method (DEM/2D): CS2D for predicting the wave motion in and around the models and DEM for estimating the models' movement by the wave motion. Numerical wave data (water surface elevation) from the CS2D was compared with that of experiment, and the deformation patterns of the numerical models were investigated in detail during the wave attack.

4.4.1 Numerical Setup
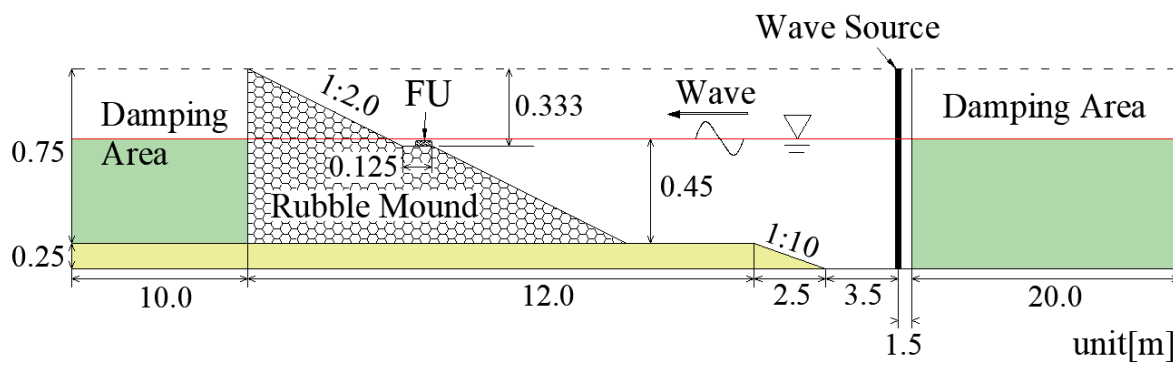
Figure 4. 1 Numerical Wave Flume Model in CS2D

The numerical wave flume model setup in the CS2D is shown in Figure 4. 1, and any turbulent model was not applied in the calculation. In this CS2D model, the vertical grid size was set as $\Delta z = 0.01$ m. The gird size in the horizontal direction Δx was set to 0.08 m in the vicinity of the offshore damping area and the wave source, and Δx was gradually decreased to 0.01 m before the toe of the rubble mound model, then gradually increased to 0.05 behind the rubble mound.

4.4.2 Initial Structural Condition for Simulation

Rubble mound model was constructed with fixed circular particles of a diameter of 2.0 cm in hexagonal arrangement, and then the numerical armor model representing the FU was placed at the seaward edge of flat portion of the mound model (Figure 4. 1). The initial model condition used for the main simulation was achieved after some pre-calculation of DEM without the external applied wave force.

4.4.3 Numerical Procedure and Simulation Cases

To simulate the FU model deformation on rubble mound due to wave action numerically, CS2D and DEM were used in this research, and only the numerical FU model deformation was focused. Thus, the rubble mound model's rubble particles were modelled as fixed particles, and the regular waves of 1.0 second wave period were applied to the structures. Firstly, the fluid motion in and around the numerical armor model with the time series was evaluated by the CS2D. Then the computation of the individual particle movement using 10-second wave data (from 15 sec to 25 sec of the time series) was performed using the DEM.

Simulation cases described in this study are listed in Table 4. 2, and in case 0, case 1-1 and case 1-2, some rubble particles of small diameter were filled in the gaps below the numerical armor model (smooth surface). A comparative examination of the numerical armor models' behavior is made with different surface conditions.

Table 4. 2 Simulation Cases

Case no.	Numerical FU Model	Surface Condition below the armor model
Case 0	Only 52 rubbles	smooth surface
Case 1-1	Model-I	smooth surface
Case 1-2	Model-II	smooth surface
Case 2-1	Model-I	on rubble mound particles of 2.0 cm in diameter
Case 2-2	Model-II	on rubble mound particles of 2.0 cm in diameter

4.4.4 Incident Waves

The incident waves computed using the CS2D were compared with those measured in the experiment under the condition of no FU model on rubble mound. The dimension of the numerical rubble mound is the same as that used in the experimental study (Figure 3. 2). Figure. 4. 2 and Fig. 4. 3 show the time series of water surface elevation η obtained in the experiment and numerical computation, respectively. They were measured and computed at two wave gauges (W2 & W3) offshore (at intervals of 50 cm) from the rubble mound. Regular waves with wave period, T, 1.0 second, and incident wave height, approx. 9.00 cm were observed, and reflection coefficient was approx. 0.2 (Goda & Suzuki, 1976). Based on the Figures. 4. 2 ~ 4. 3, it can be concluded that the CS2D model is capable of estimating the water level variations sufficiently.
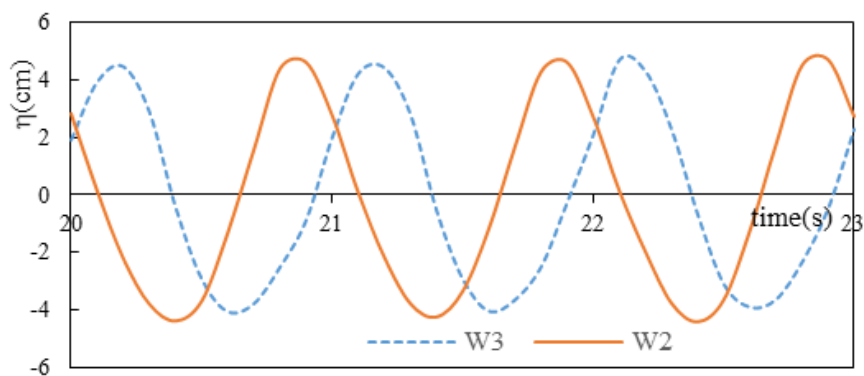
Figure 4. 2 Water surface elevation from experiment
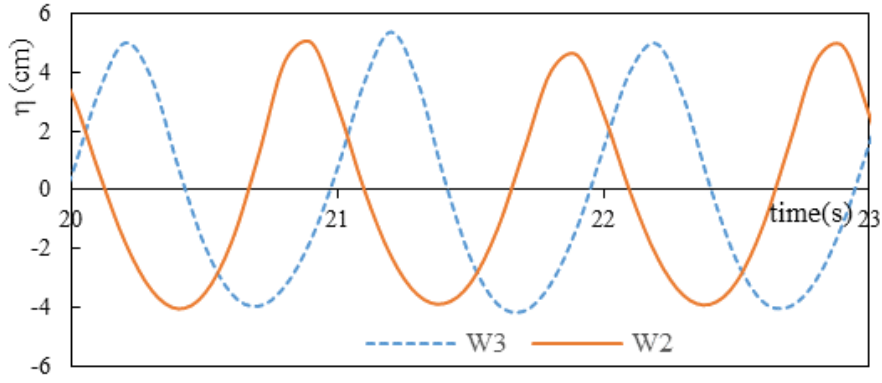
Figure 4. 3 Water surface elevation from CS2D

4.4.5 DEM Input Parameters and Calculation Domain

The FU model deformation was investigated by using the DEM input parameters of several relevant researches and by considering the simulation time, and then the optimal simulation results were presented in this thesis. The input parameters used for the simulation of the numerical FU model deformation are listed in Table 4. 3, where K_n and K_s are particle contact normal and shear stiffness, μ and μ' are static and dynamic friction coefficients, $k_{B, n}$ and $k_{B, s}$ are parallel bond's normal and shear stiffnesses per unit area, and λ is bond-radius multiplier. The densities of virtual rubble and virtual fiber were 2.65 g/cm^3 and 1.15 g/cm^3, respectively, and the tensile strength and shear strength for the bond model between virtual fiber particles were applied as 100 MPa.

Applying the method presented in the work of Rojek et al., (2011), the critical time step obtained was 7.3x10^{-7} s if the safety factor was set to 0.1. Thus, the time step for this calculation was 1x10^{-7} s, and approx. 30 min was taken for one second wave attack using the FORTRAN programming language. Moreover, the ratio of particle normal to shear stiffness (K_n/K_s) and the ratio of bond normal to shear stiffness ($k_{B, n}/k_{B, s}$) in this simulation was 2.6, and the damping coefficients (α^t & α^r) were 0.06.

Then the input parameters for the simulation of deformation of rubbles without being wrapped with virtual fiber particles (case 0) are given in Table 4. 4, η_n and η_s are normal and shear damping coefficients. In this case, the typical DEM model was applied the same way as the simulation of rubble mound structure deformation by waves (Araki et al., 2001, 2002, Maeno et al., 2005, 2009 & Fukumizu et al., 2018). The calculation domain of all the simulation

cases is illustrated in Figure 4. 4, in which the horizontal and vertical distances are 30 and 12 cm respectively.

Table 4. 3 DEM model input parameters for the simulation

Parameters	Rubble to Rubble	Fiber to Fiber	Rubble to Fiber	Fiber to Rubble of rubble mound structure
K_n (N/m)	2.73×10^5	4.55×10^4	9.1×10^4	9.1×10^4
K_s (N/m)	1.05×10^5	1.75×10^4	3.5×10^4	3.5×10^4
μ	0.6	0.1	0.6	0.3
μ'	0.4	0.06	0.4	0.2
$k_{B, n}$ (Pa/m)		4.55×10^7		
$k_{B, s}$ (Pa/m)		1.75×10^7		
λ	0	1	0	0

Table 4. 4 DEM model input parameters for case 0

K_n (N/m)	2.73×10^5
K_s (N/m)	1.05×10^5
μ	0.6
μ'	0.4
η_n (Ns/m)	5.7×10
η_s (Ns/m)	1.0×10
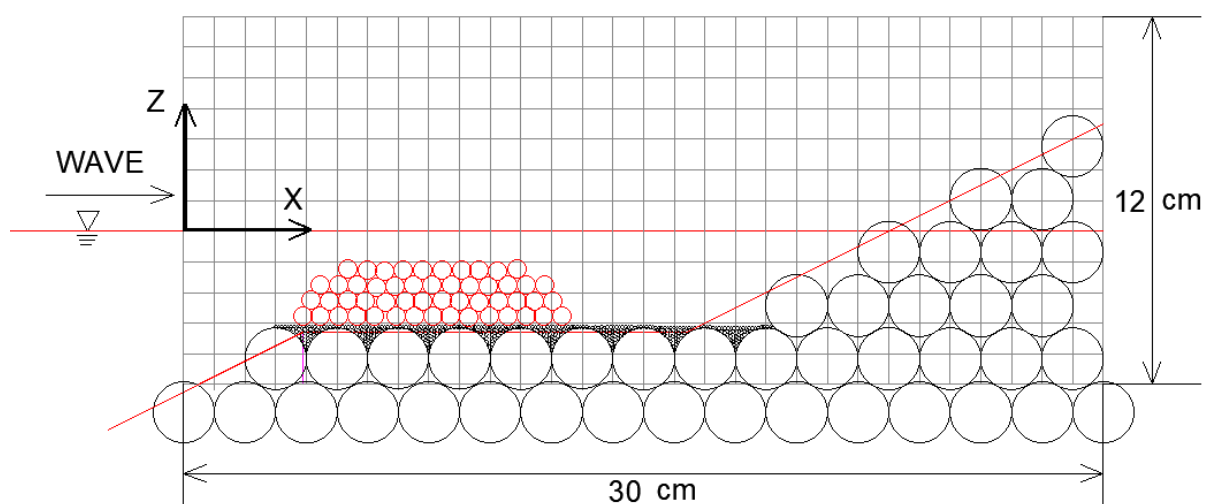
(a) Calculation domain of case 0
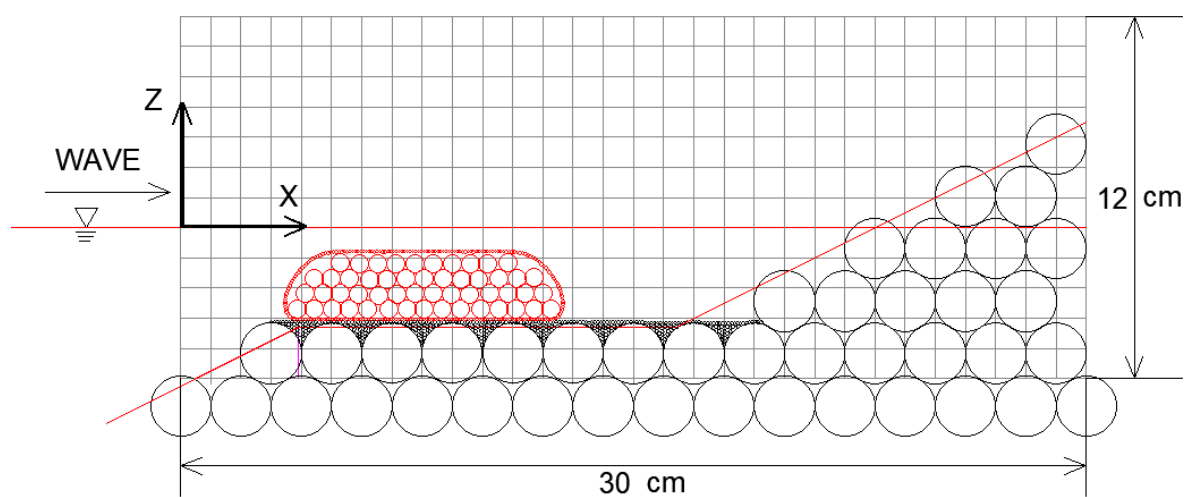
(b) Calculation domain of case 1-1 (on smooth surface)
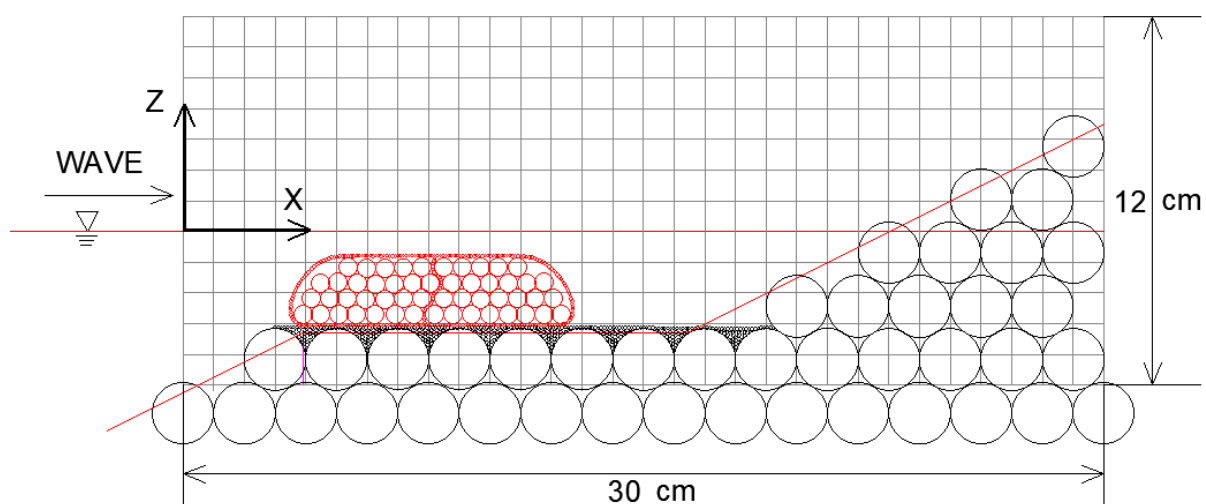
(c) Calculation domain of case 1-2 (on smooth surface)
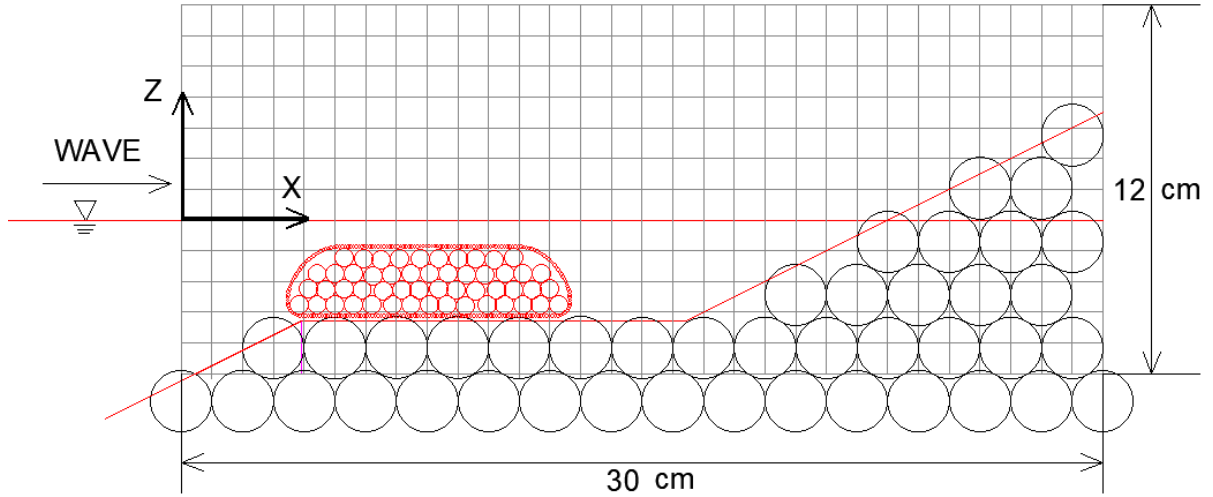
(d) Calculation domain of case 2-1
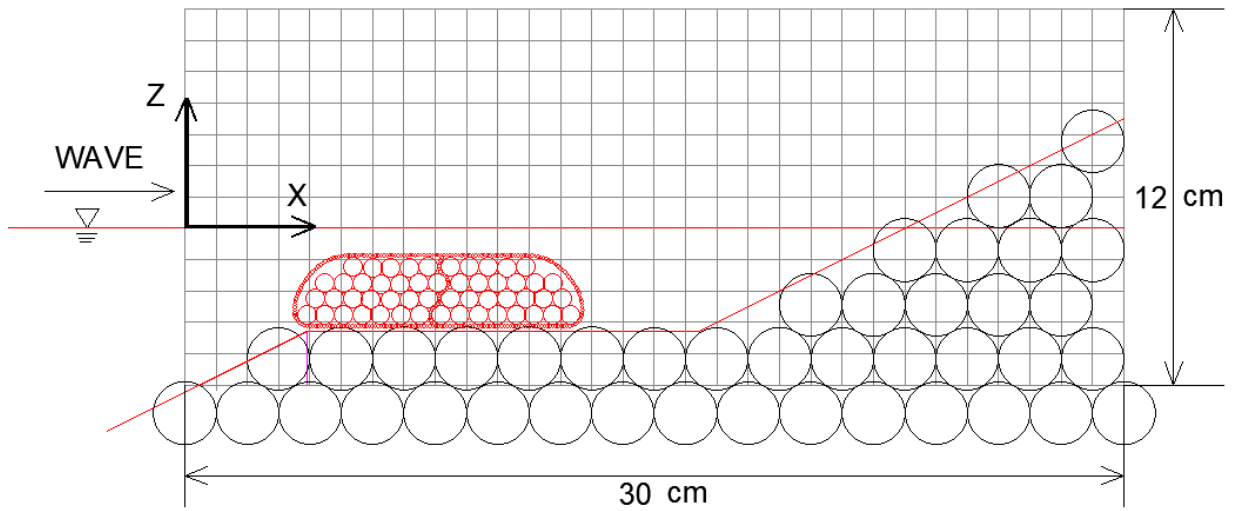
(e) Calculation domain of case 2-2

Figure 4. 4 DEM calculation domain

4.5 NUMERICAL RESULTS AND DISCUSSION

As mentioned in the above section, the simulations focused on only the deformation of the armor FU models, and the models were placed at the seaward edge of the flat portion of the rubble mound model. Figure 4. 5 (a) and (b) show the profiles of rubbles before and after wave attack for one second (case 0), and the rubbles moved separately to both offshore and onshore sides due to the one-second wave motion.

The deformation profiles of Model-I and Model-II on smooth surface (case 1-1 and case 1-2) computed at every one-second wave attack are given in Figures 4. 6 ~ 4. 7. Figures 4. 6(a) ~ 4. 7(a) show the initial numerical model conditions before the external wave forces were applied to the models. During the wave attack, the rubbles were moving in the string of fiber particles. In comparison of case 0, case 1-1 and case 1-2 after one-second wave attack, the movements of the rubbles from Model-I and Model-II were not significant, and the parallel bond model inserted between the virtual fiber particles, described in chapter 2, seems working properly by supporting a tension.

The profiles of the Model-I, shown in Figure 4. 6 (b) after 1.0 sec-, (c) after 2.0 sec- and (d) after 3.0 sec-wave attack, were almost the same; just a little movement of rubbles inside the fiber string were found. In Figure 4. 6 (e) after 4.0 sec-, (f) after 5.0 sec-, (g) after 6.0 sec- and (h) after 7.0 sec-wave attack, significant movement behavior of rubbles inside the fiber string occurred, causing a displacement of the model to the lee side of the rubble mound. Then, in the last three cases (i, j, k) of Figure 4. 6, only a little displacement of the rubbles inside the string were observed.

Likewise, in Figure 4. 7, the particle motion of Model-II computed at every one-second of wave action is illustrated. Considerable rubble movements of the Model-II were found in Figure 4.7 (e) after 4.0 sec-, (f) after 5.0- and (g) after 6.0-sec-wave attack. In the first three and last four cases (Figure 4. 7 b ~ d & h ~ k), the profiles showed a little or no movement of the rubbles inside the fiber string. The constraining rope fiber particles inside lowered the movement of the rubble particles, and thus the deformation of the Model-II was not significant in comparison to the Model-I. However, in the Model-II, the rubbles from one side of the constraining rope fibers could not move to the other side in this two-dimensional numerical model. Thus, the numerical armor model, Model-II, could not follow the deformation mechanism of the experimental S-type models adequately.
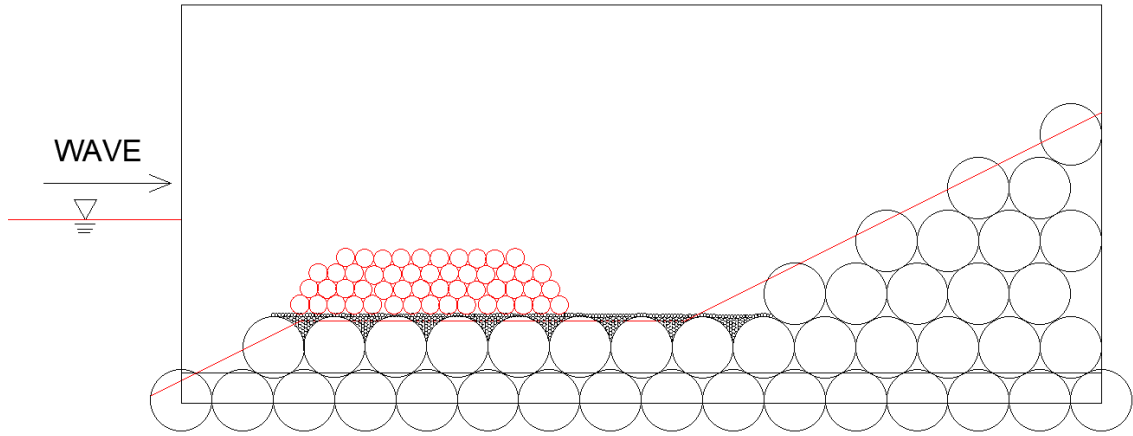
(a) Before wave attack
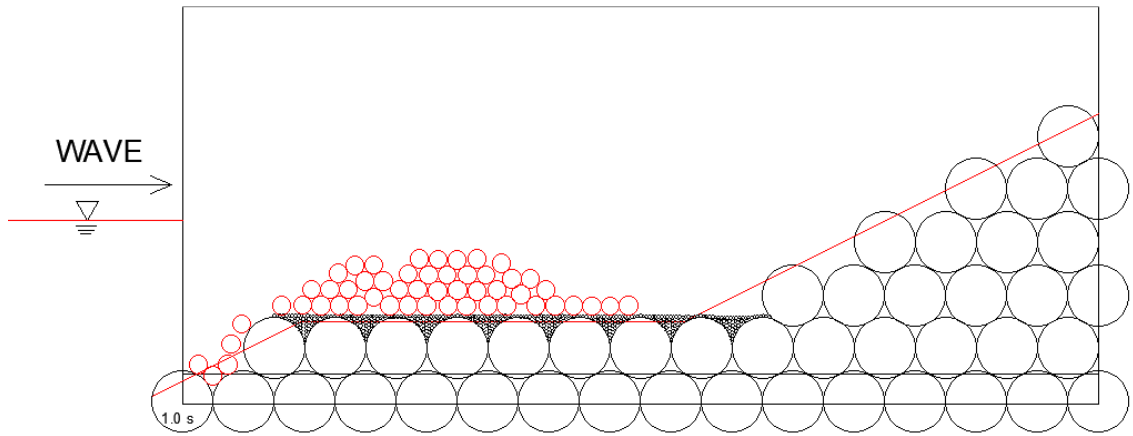
(a) After one-second wave attack

Figure 4. 5 Simulation result of case 0 after 1.0 sec
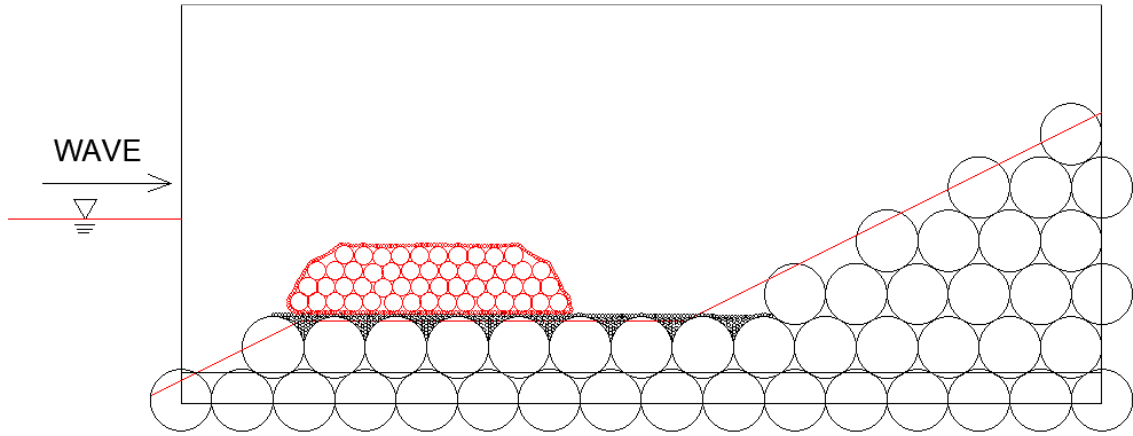
(a) Initial condition of Model-I (case 1-1)
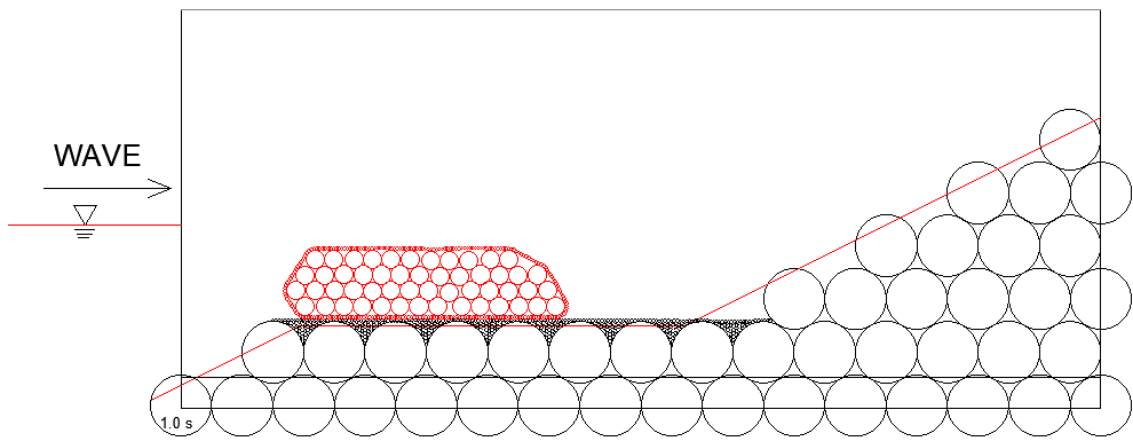
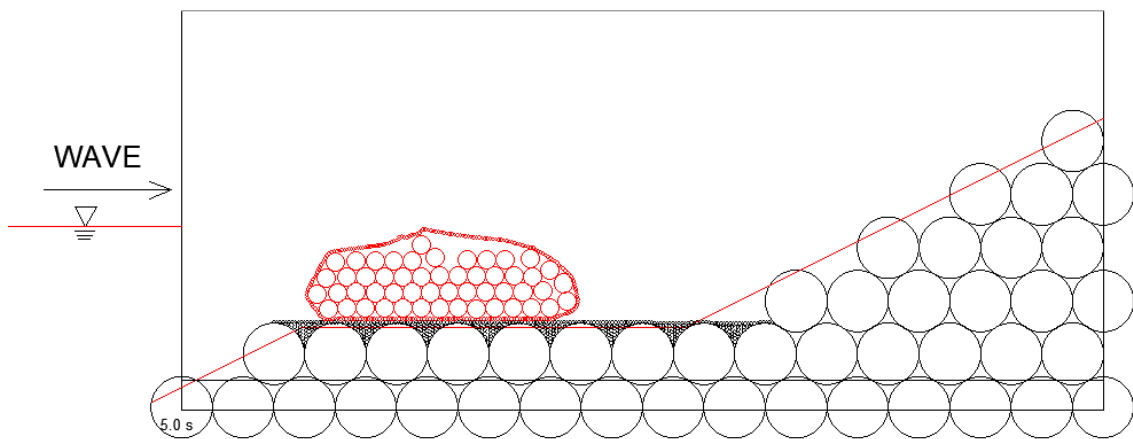(b) Model-I after 1.0 sec (case 1-1)
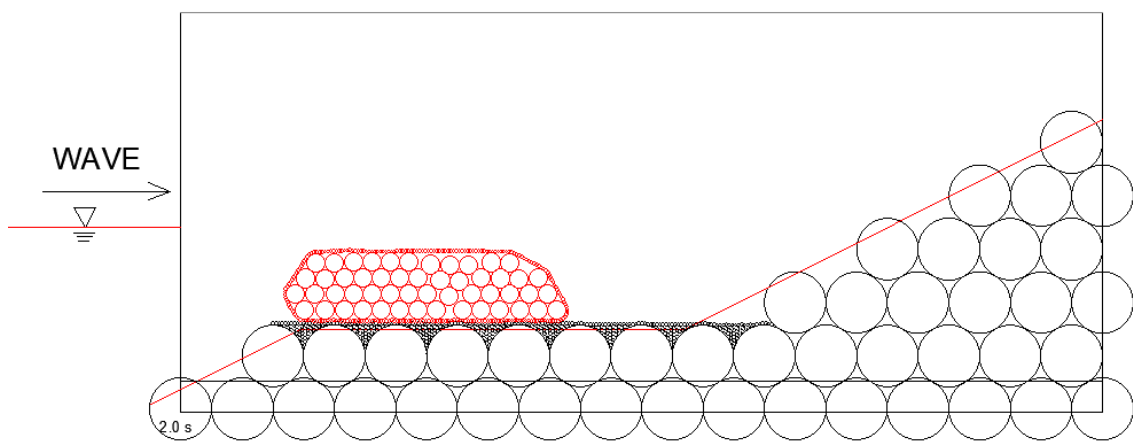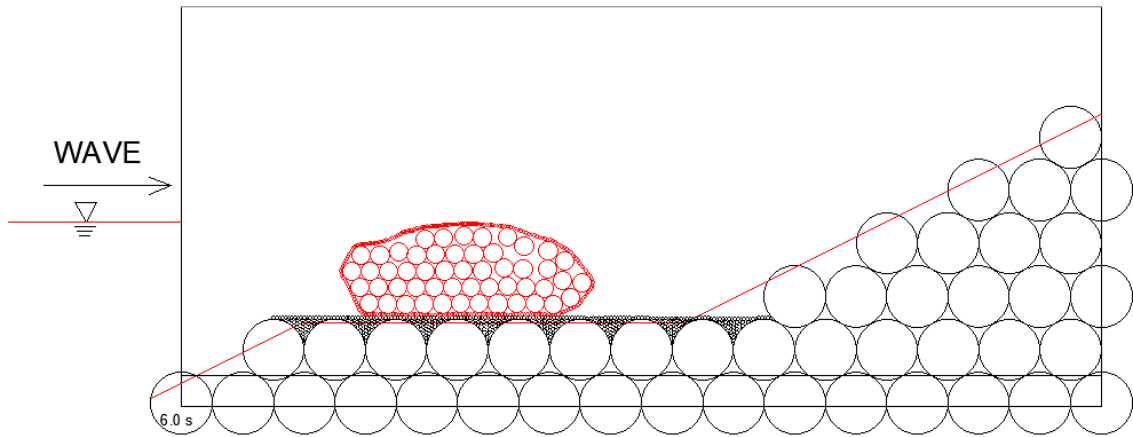

(c) Model-I after 2.0 sec (case 1-1)
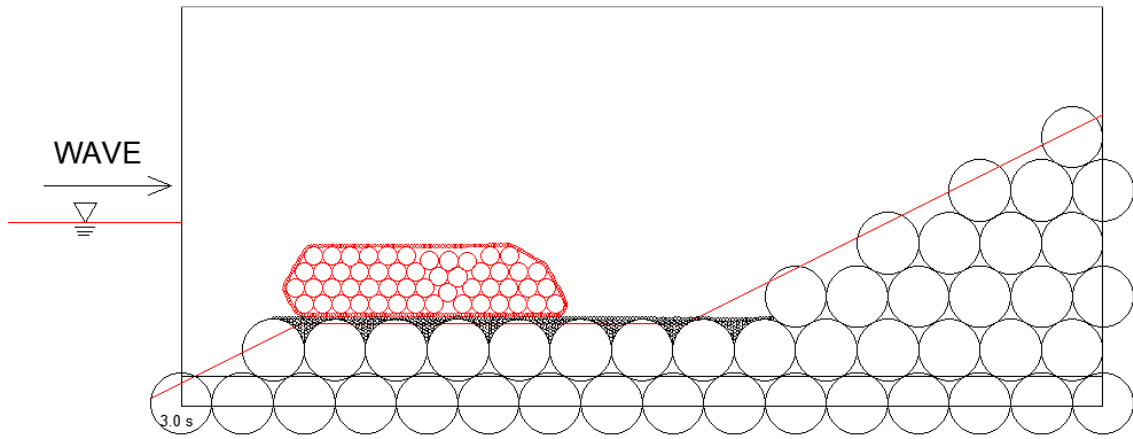
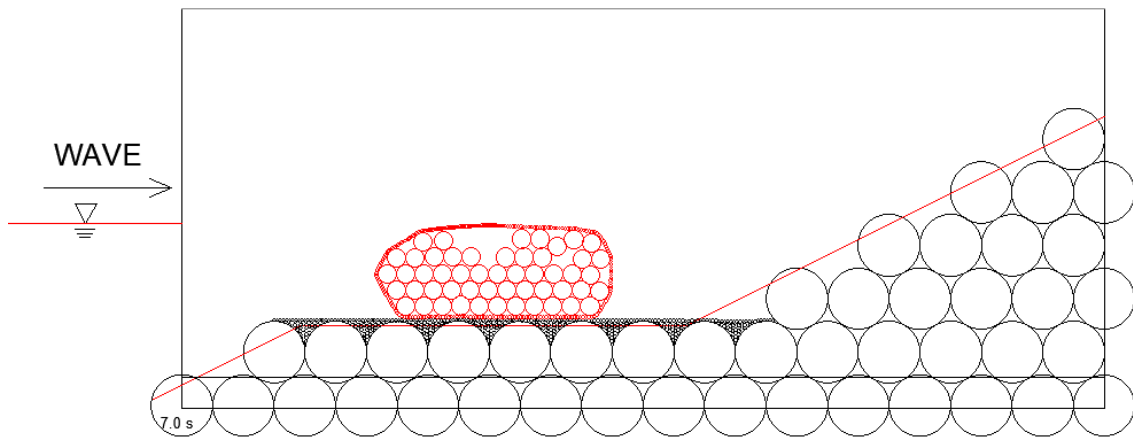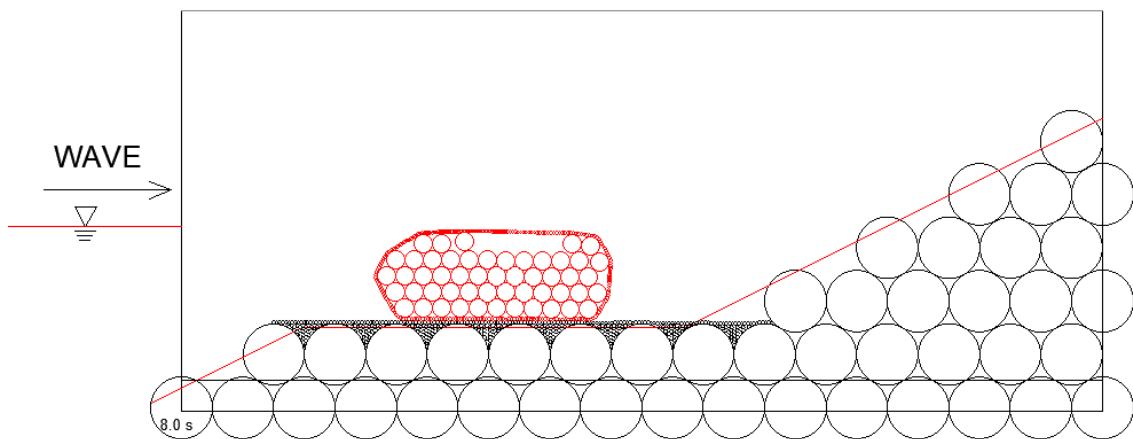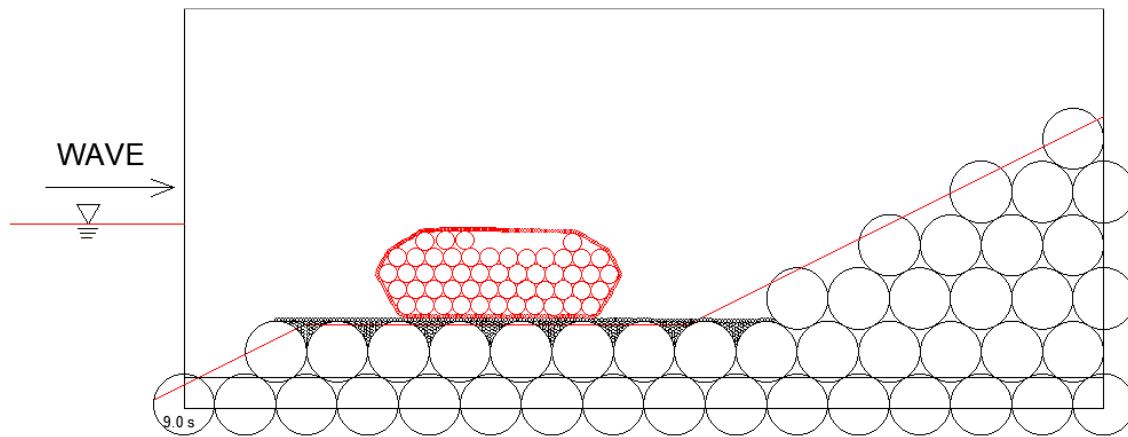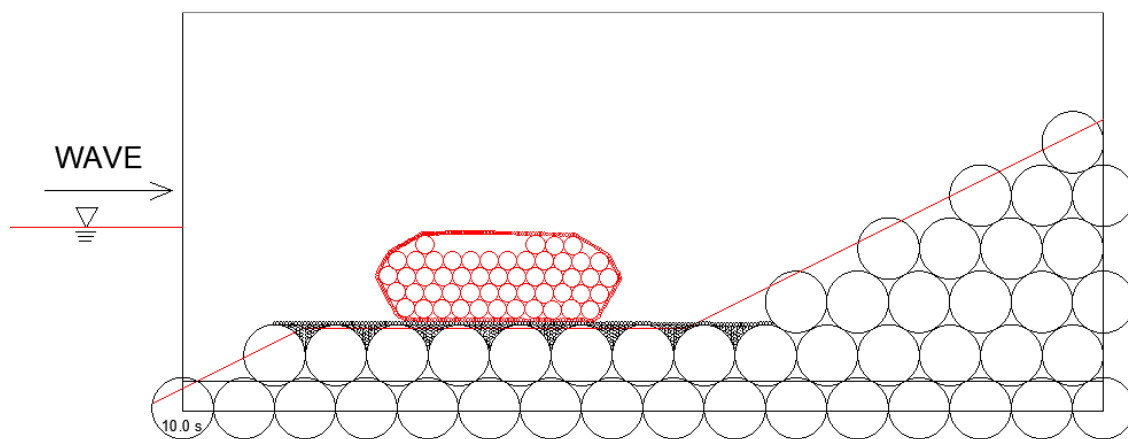(d) Model-I after 3.0 sec (case 1-1)
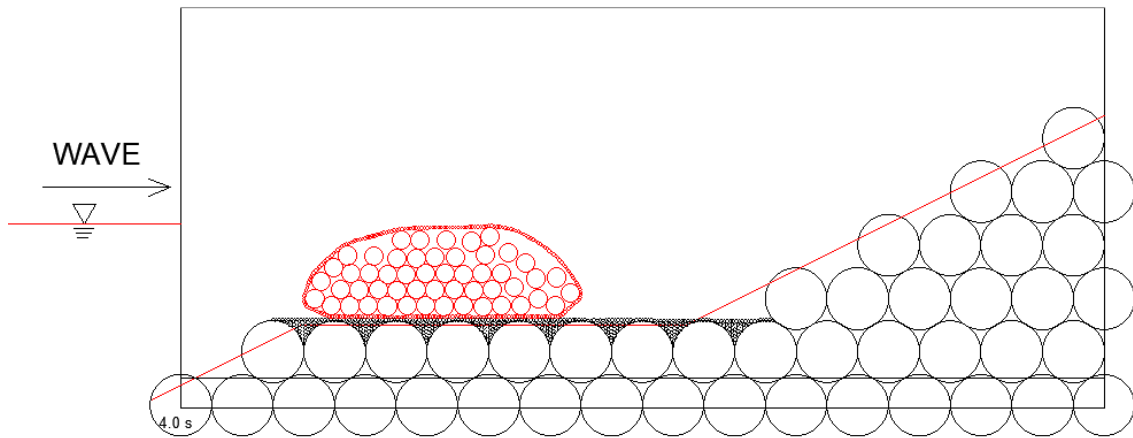
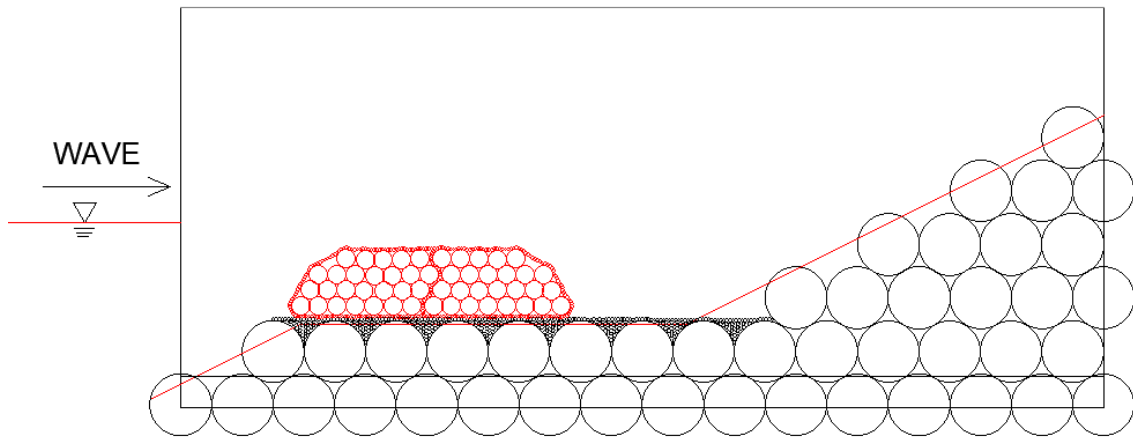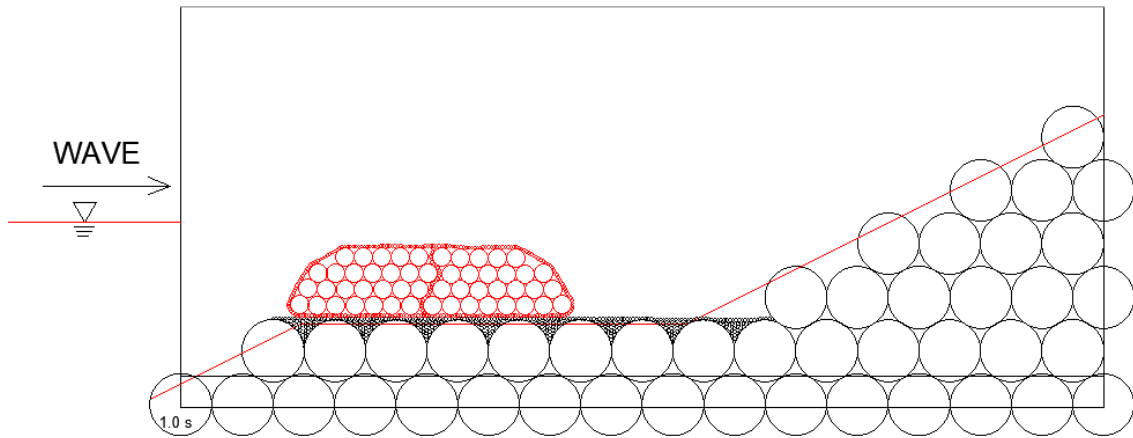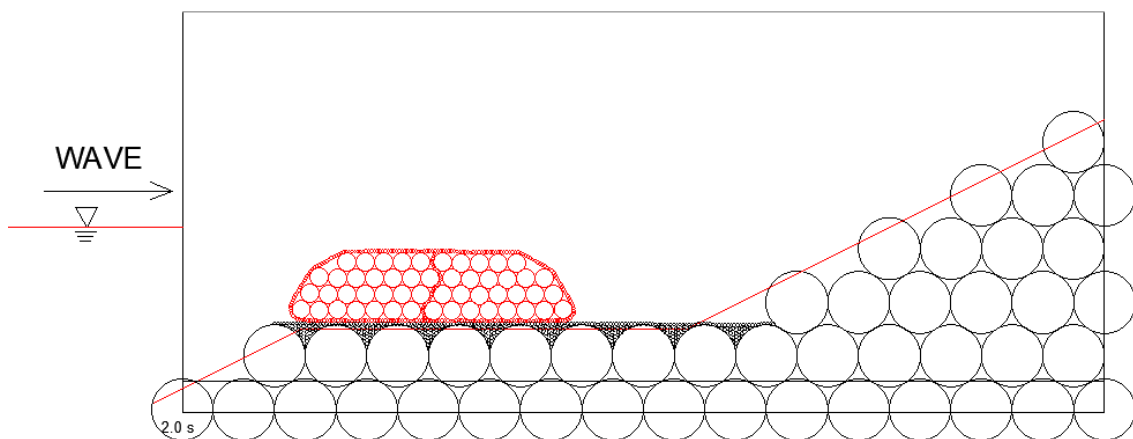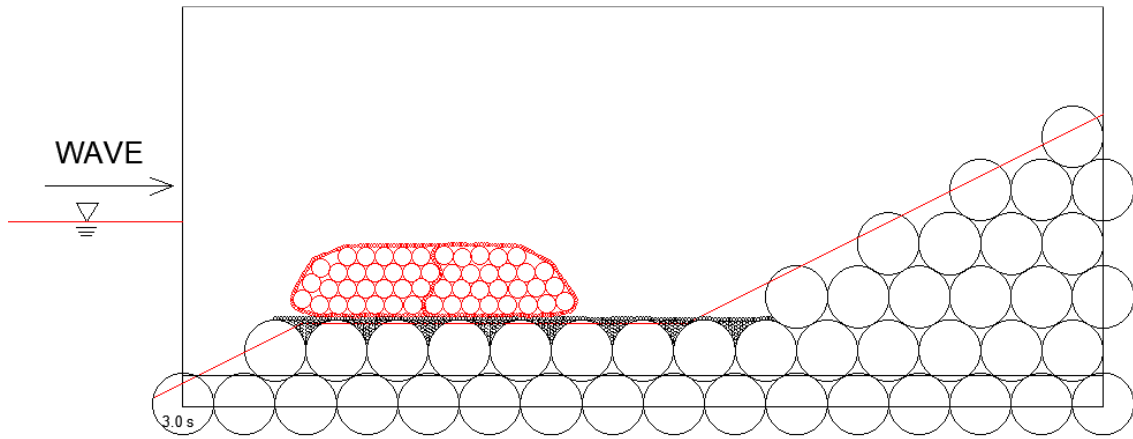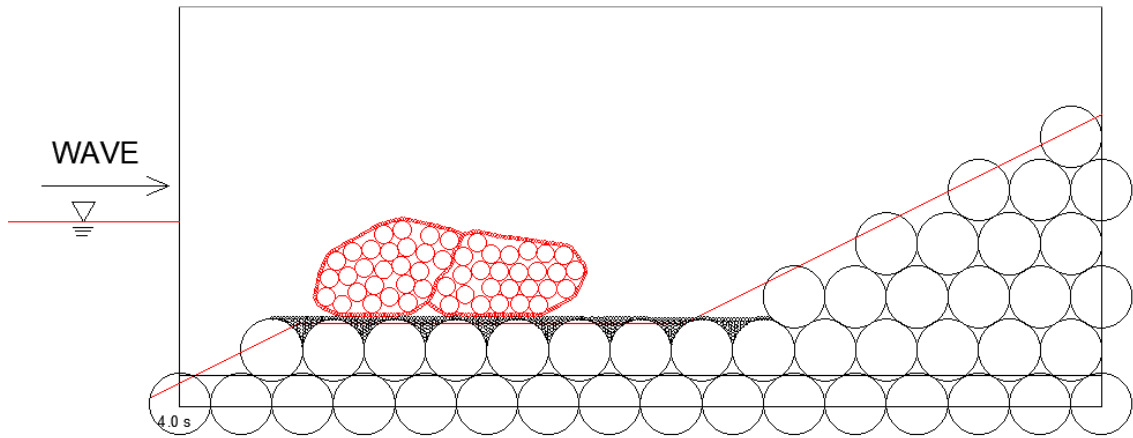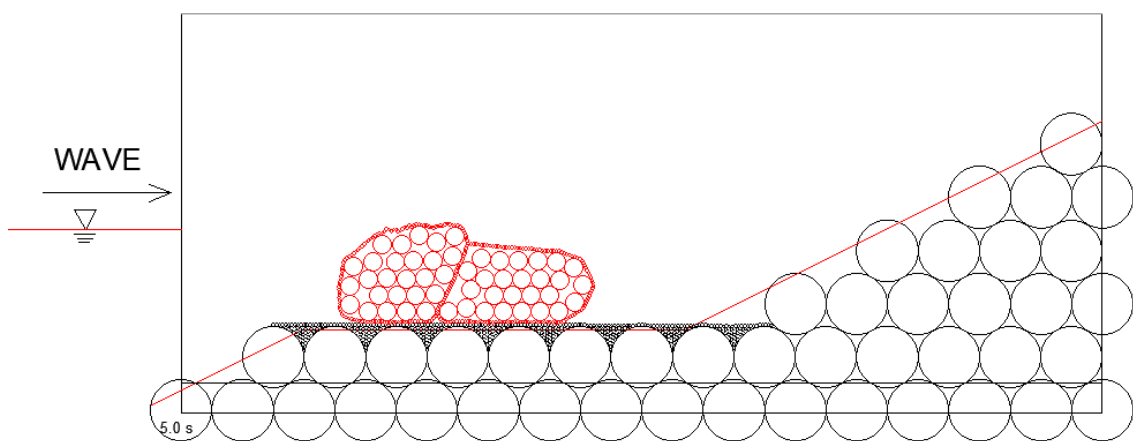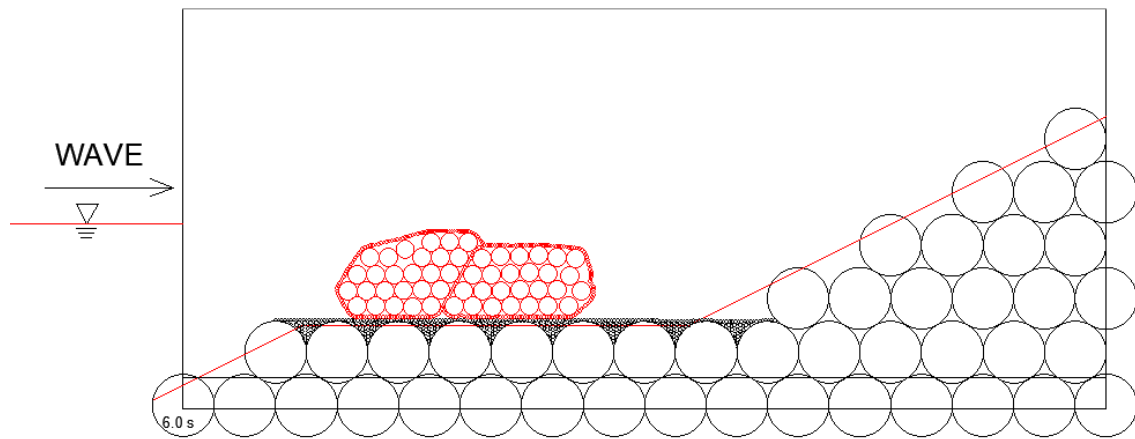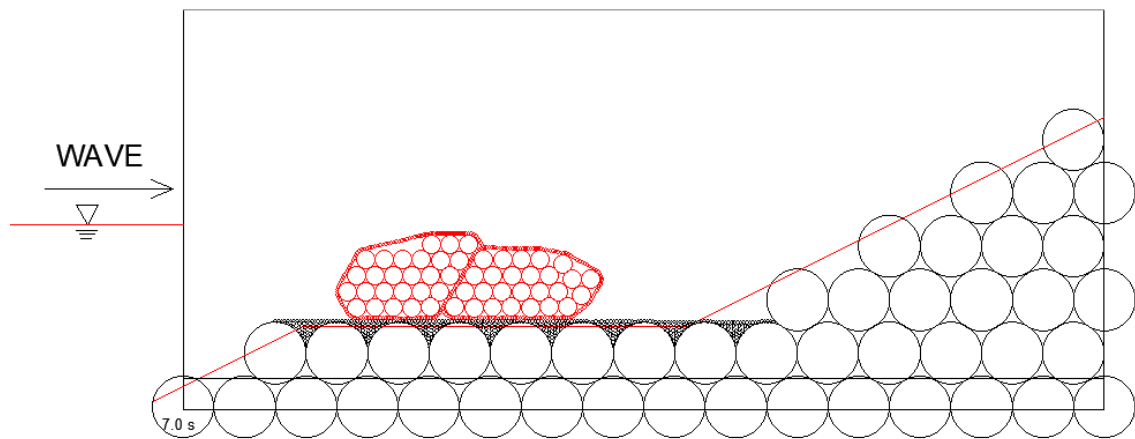(e) Model-I after 4.0 sec (case 1-1)

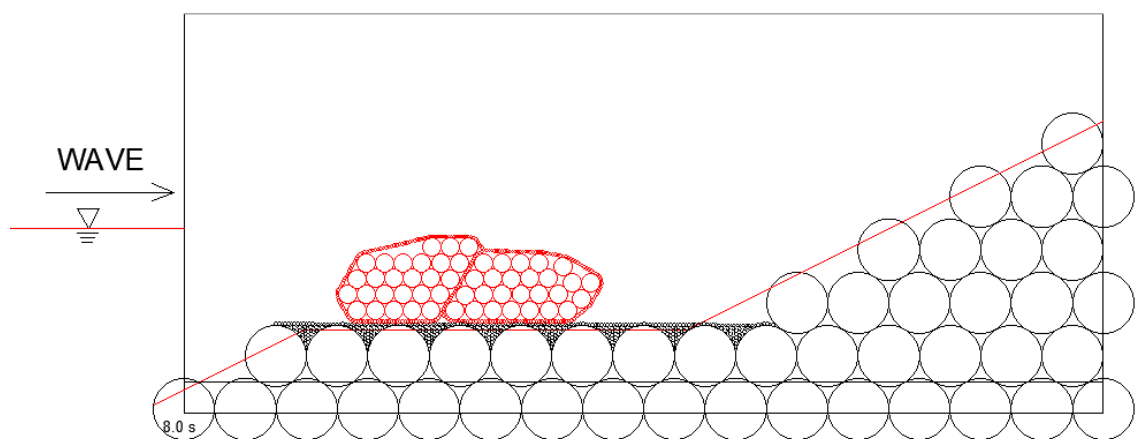
(f) Model-I after 5.0 sec (case 1-1)

(g) Model-I after 6.0 sec (case 1-1)

(h) Model-I after 7.0 sec (case 1-1)

(i) Model-I after 8.0 sec (case 1-1)

(j) Model-I after 9.0 sec (case 1-1)

(k) Model-I after 10.0 sec (case 1-1)

Figure 4. 6 Computed deformations of Model-I (case 1-1)

(a) Initial condition of Model-II (case 1-2)

(b) Model-II after 1.0 sec (case 1-2)

(c) Model-II after 2.0 sec (case 1-2)

(d) Model-II after 3.0 sec (case 1-2)

(e) Model-II after 4.0 sec (case 1-2)

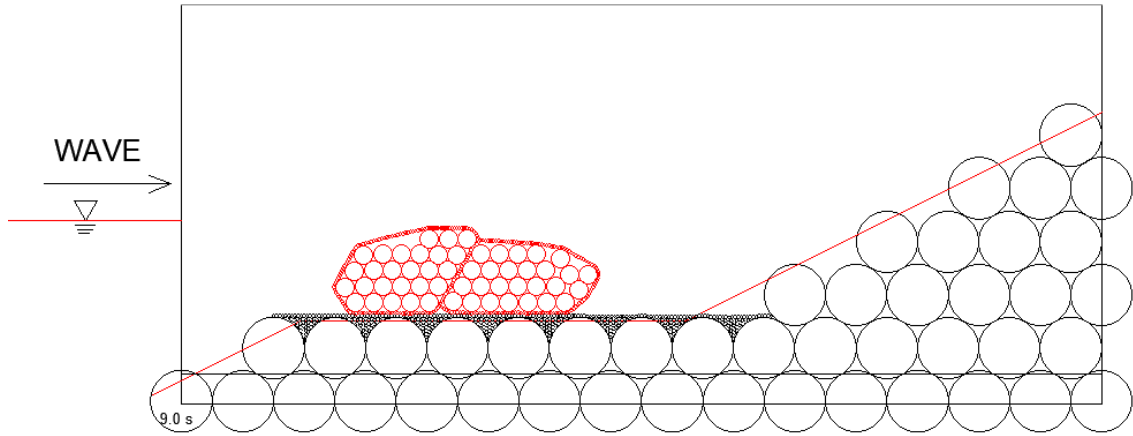(f) Model-II after 5.0 sec (case 1-2)
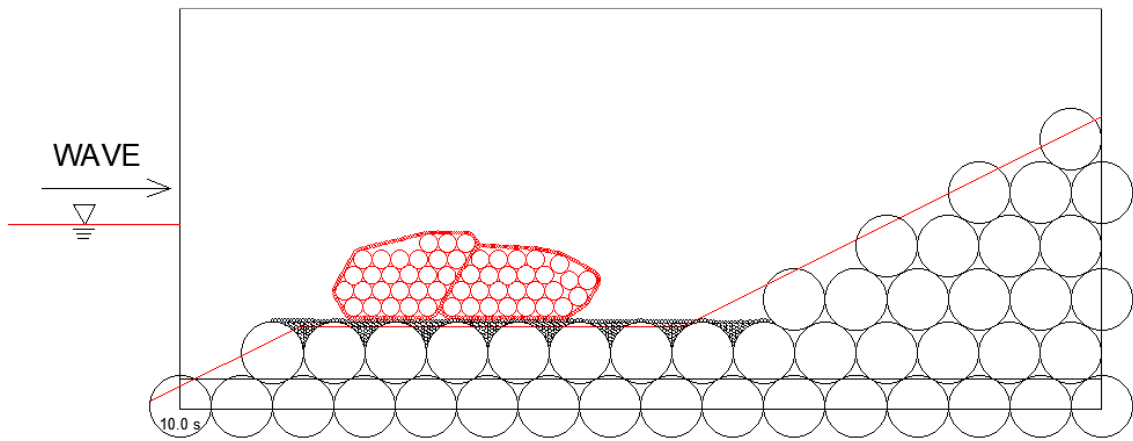
(g) Model-II after 6.0 sec (case 1-2)

(h) Model-II after 7.0 sec (case 1-2)

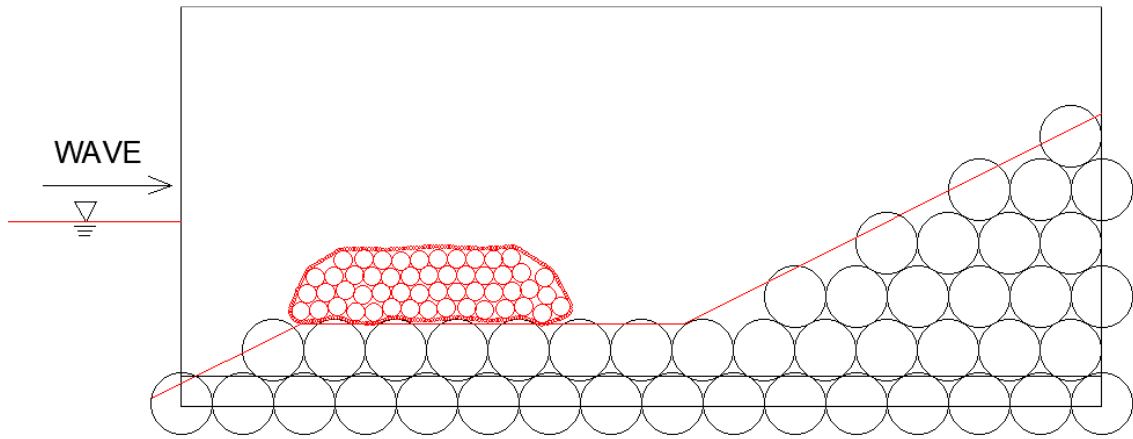
(i) Model-II after 8.0 sec (case 1-2)

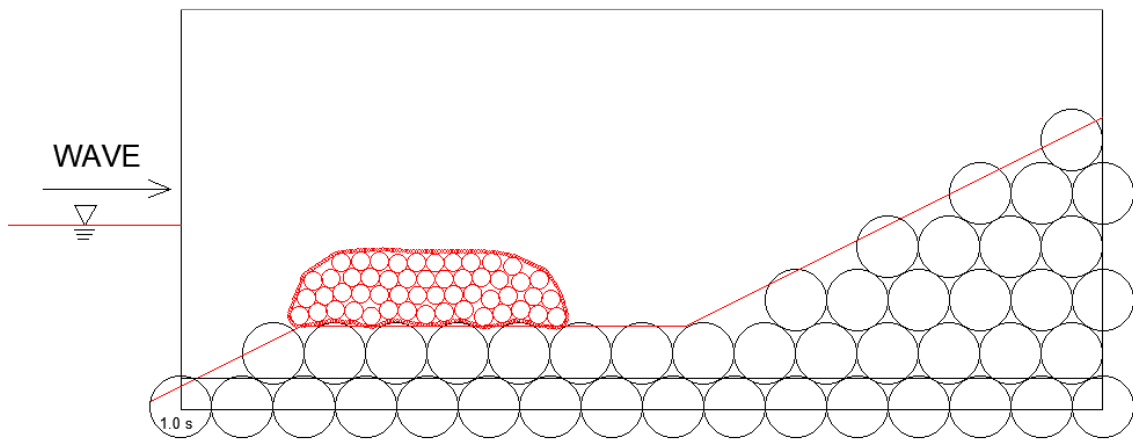(j) Model-II after 9.0 sec (case 1-2)

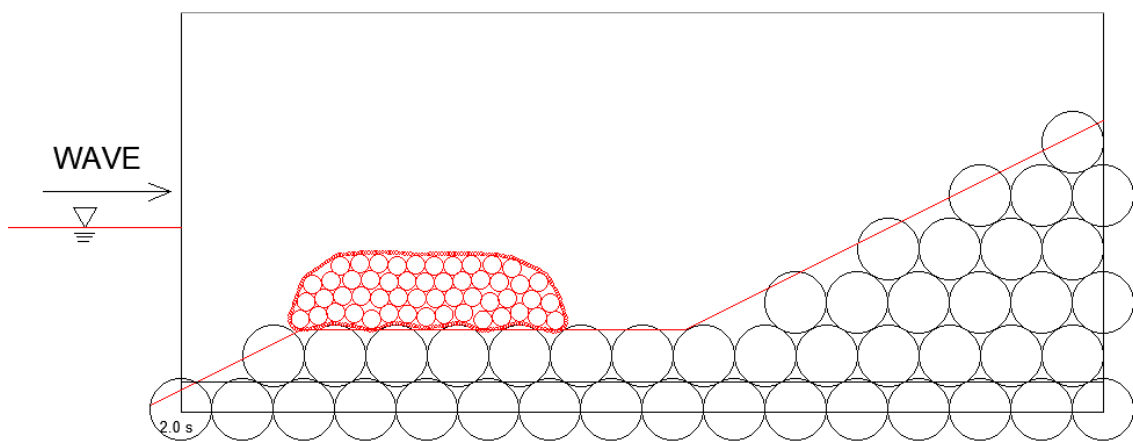(k) Model-II after 10.0 sec (case 1-2)

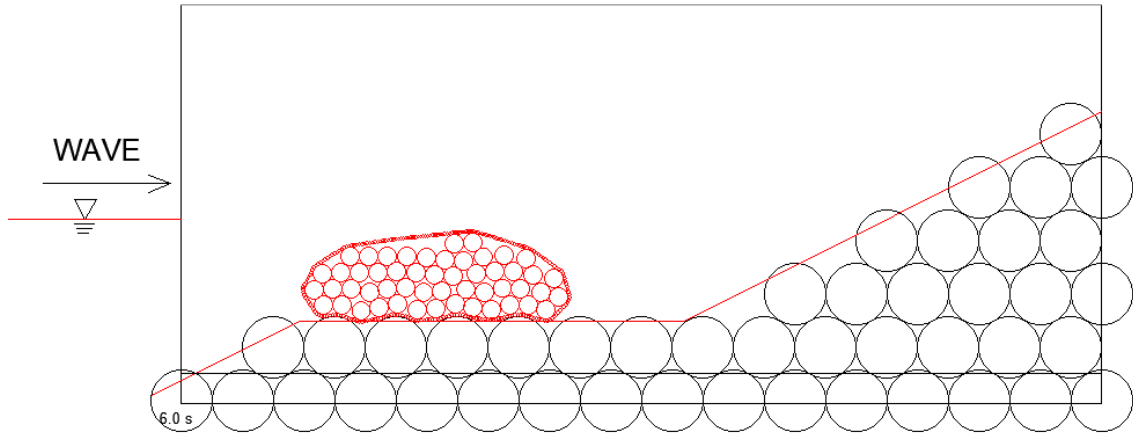Figure 4. 7 Computed deformations of Model-II (case 1-2)

(a) Initial condition of Model-I (case 2-1)

(b) Model-I after 1.0 sec (case 2-1)

(c) Model-I after 2.0 sec (case 2-1)

(d) Model-I after 3.0 sec (case 2-1)

(e) Model-I after 4.0 sec (case 2-1)

(f) Model-I after 5.0 sec (case 2-1)

(g) Model-I after 6.0 sec (case 2-1)

(h) Model-I after 7.0 sec (case 2-1)

(i) Model-I after 8.0 sec (case 2-1)

96

(j) Model-I after 9.0 sec (case 2-1)

(k) Model-I after 10.0 sec (case 2-1)

Figure 4. 8 Computed deformations of Model-I (case 2-1)

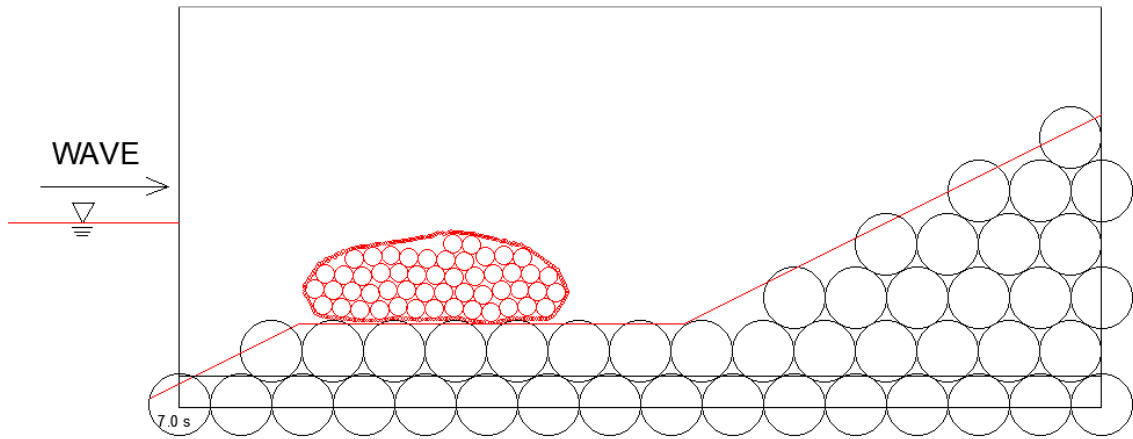(a) Initial condition of Model-II (case 2-2)

(b) Model-II after 1.0 sec (case 2-2)

(c) Model-II after 2.0 sec (case 2-2)

(d) Model-II after 3.0 sec (case 2-2)

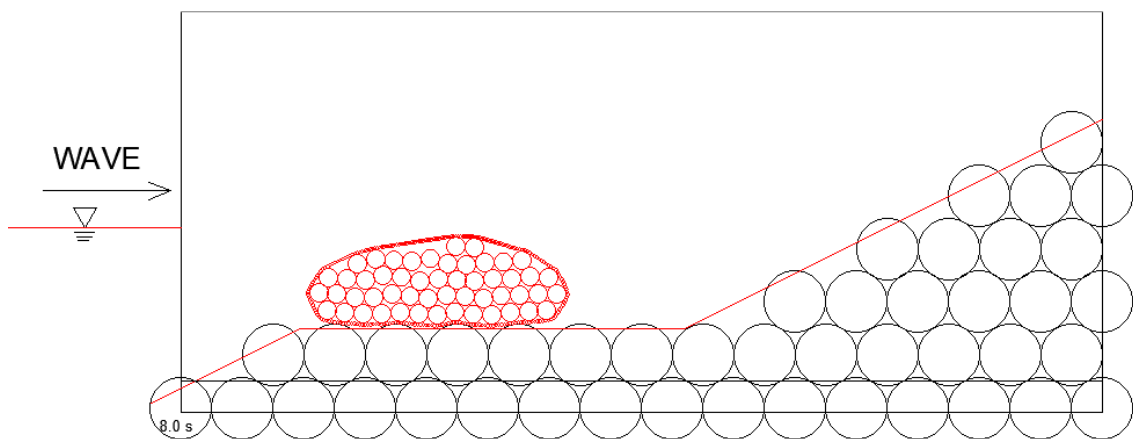(e) Model-II after 4.0 sec (case 2-2)

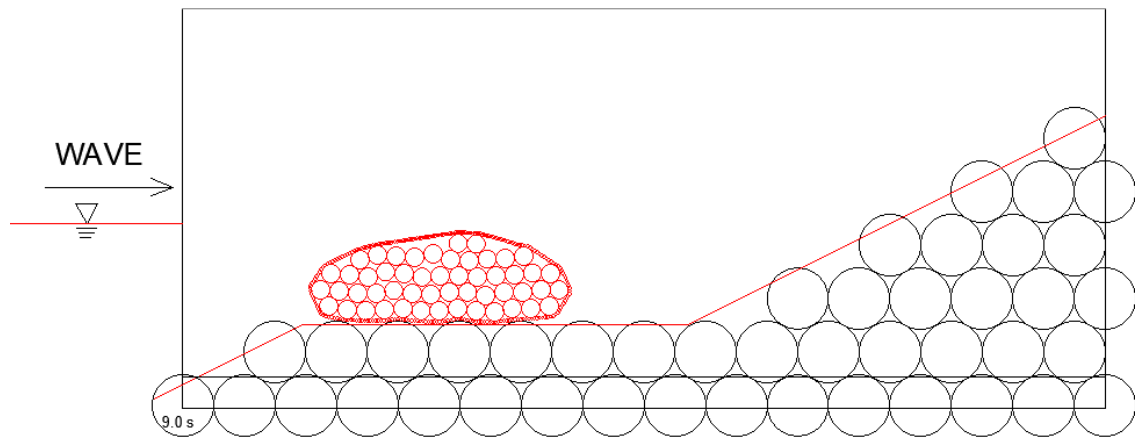(f) Model-II after 5.0 sec (case 2-2)

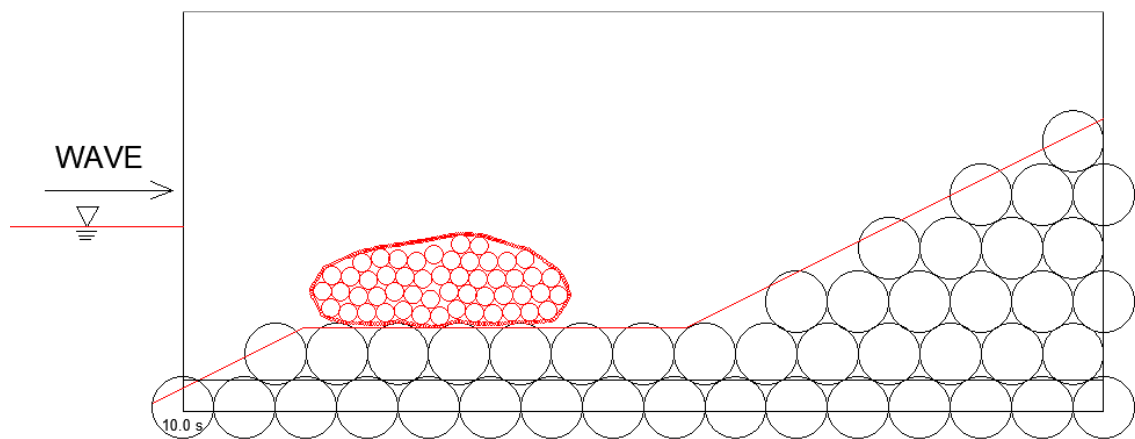(g) Model-II after 6.0 sec (case 2-2)

(h) Model-II after 7.0 sec (case 2-2)
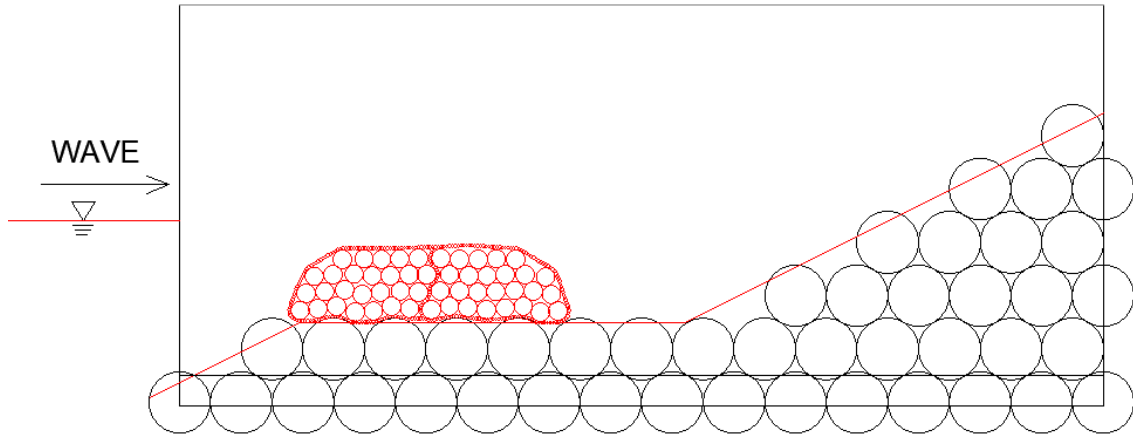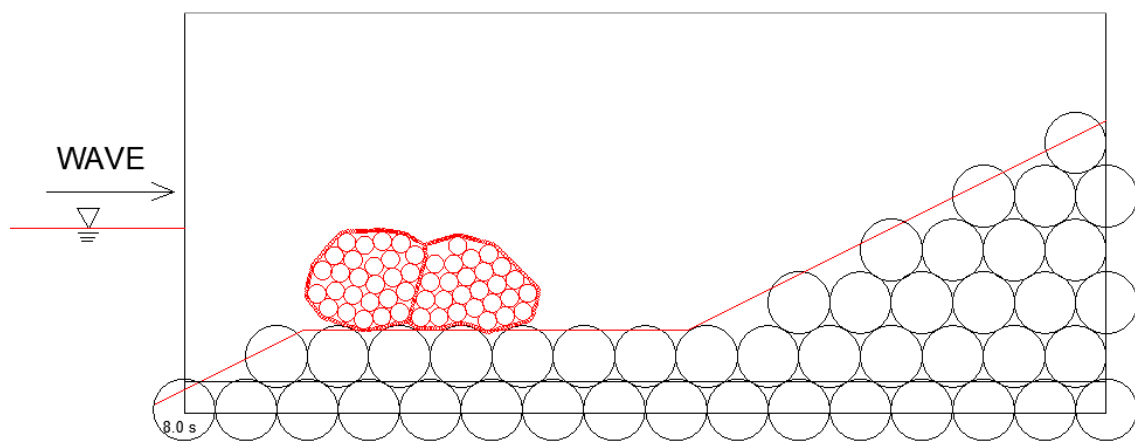

(i) Model-II after 8.0 sec (case 2-2)
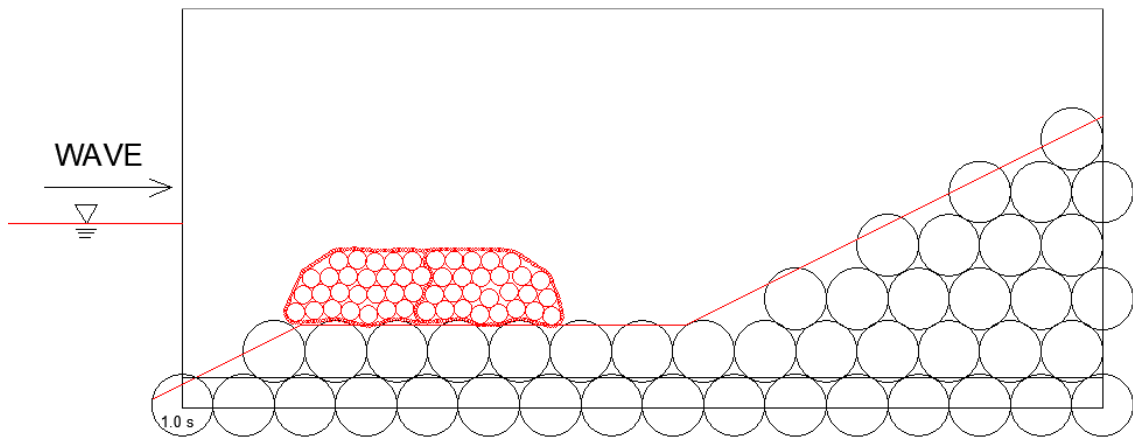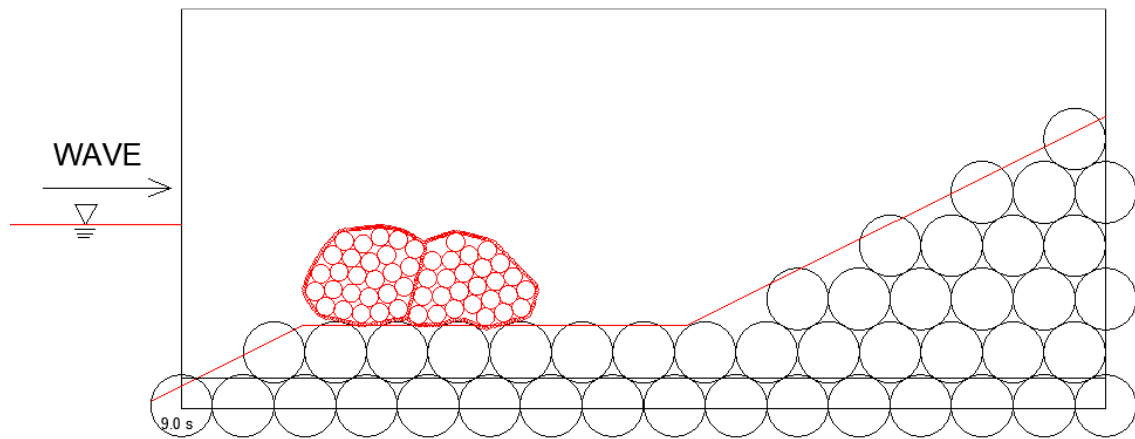
(j) Model-II after 9.0 sec (case 2-2)
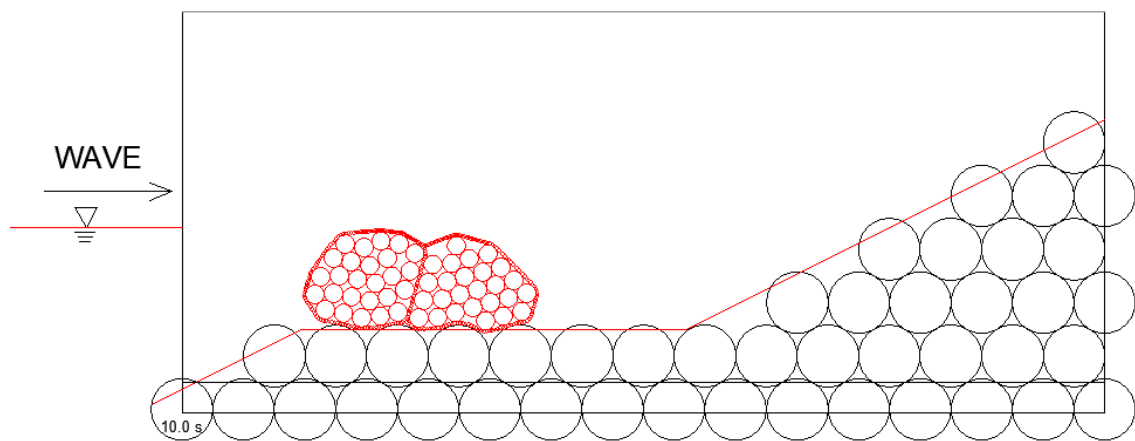
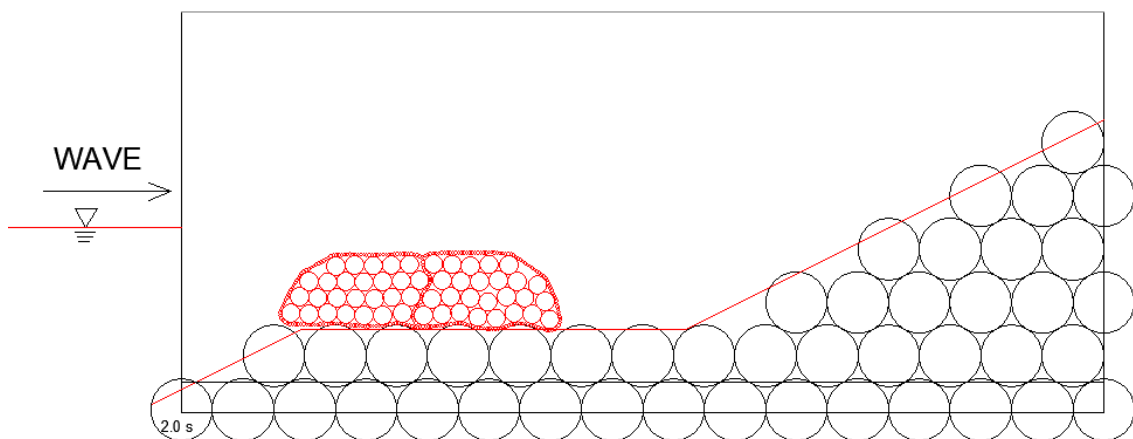
(k) Model-II after 10.0 sec (case 2-2)
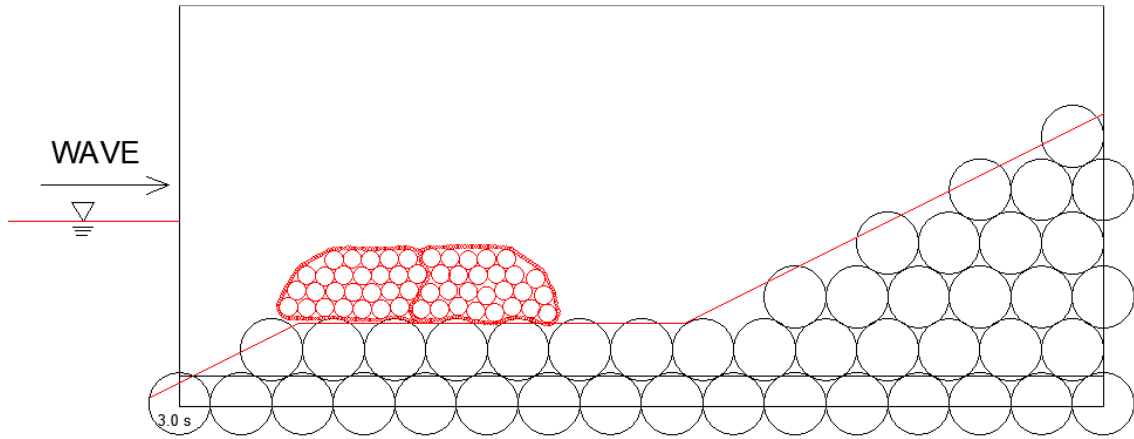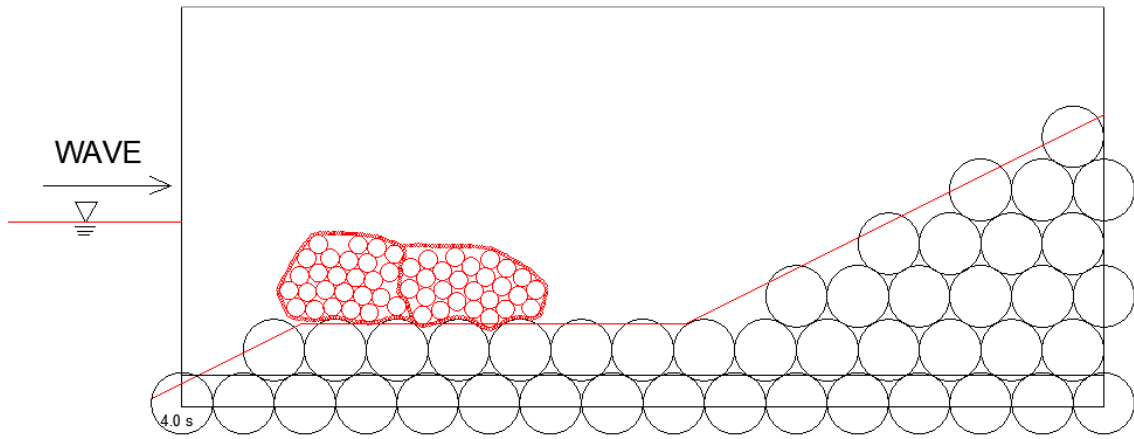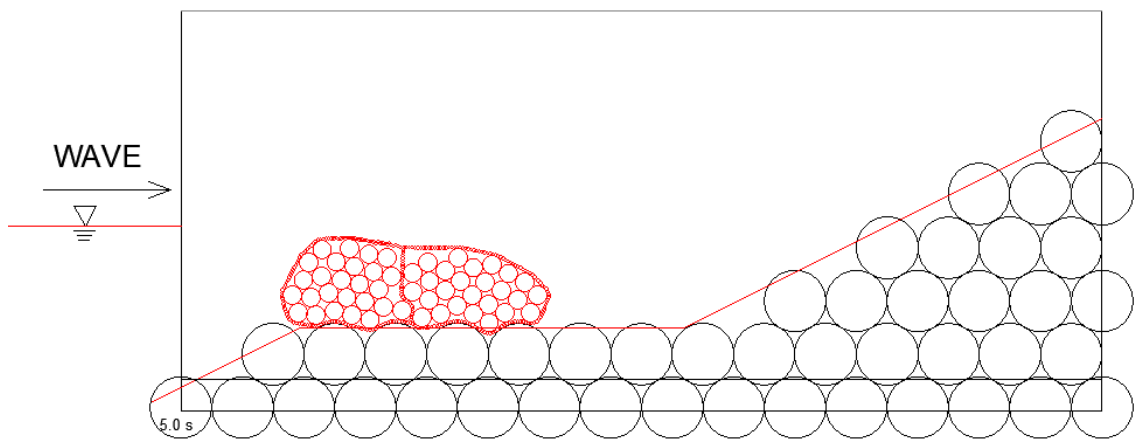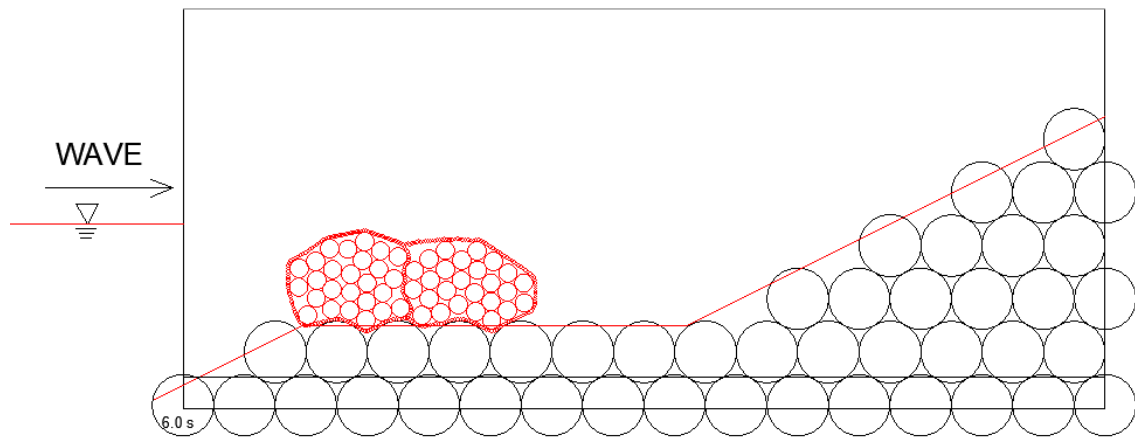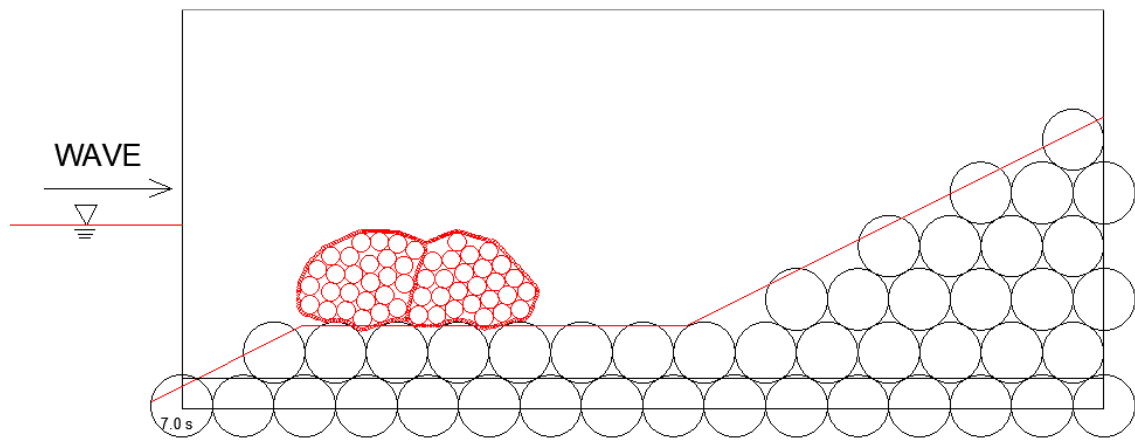
Figure 4. 9 Computed deformations of Model-II (case 2-2)

Figure 4. 8 shows the computed deformation patterns of the Model-I on rubble mound model without leveling the surface with small rubbles at every one-second wave motion attack (case 2-1). Similar to the case 1-1, the displacement of the model to the lee side of the mound was observed causing a deformation during the wave attack.

The deformation patterns of the Model-II computed after every one second of the striking waves are illustrated in Figure 4. 9 (case 2-2), where the Model-II deformed slightly, and only a very small displacement of the model occurred similar to the case 1-2. The constraining rope fiber particles controlled the movement of the rubbles by waves which could lead to the model displacement in an effective way. This numerical result was similar to that of the FU model experiments, presented in Chapter 3.

In comparison of Figure 4. 6(k) and Figure 4. 8(k) which show the final condition of the Model-I on different surfaces, the model on smooth surface moved faster than that on rough surface, to the lee side of the rubble mound. Similarly, the Model-II placed on smooth surface showed a notable displacement to the onshore side when compared to the model movement on rough rubble surface (Figures 4. 7(k) & 4. 9(k)).

In the experimental FU models, the volume of filter bag was greater than that of filling rubble stones to an extent (Tables 3. 2 & 3. 3). The stability of the models depends on the volume ratio (of fiber bag/filling stones) and also on the constraining rope length inside the bag. However, in this numerical investigation, these volume ratio and rope length were not focused yet.

CHAPTER 5

Chapter 5

CONCLUSIONS

OUTLINE

Chapter 5 aims to summarize the conclusions of overall studies. Firstly, conclusions of experimental observations that are given in Chapter 3 are discussed. Then numerical investigation work which is shown in Chapter 4 is discussed, and lastly some remarks based on the study are described.

5.1 CONCLUSIONS OF CHAPTER 3

The influence of constraint degree and volume ratio (filter net/filling stones) of an S-type FU on its hydraulic stability is investigated. The FU models, having different constraining rope lengths and different volume ratios, were considered first. The FU models were then tested under regular waves, and the experiment for each FU model was repeated three times in this study. The results of Single-FU experiment were reasonable for a certain extent compared to Multiple-FU experimental results from the view point of damage behavior. In Multiple-FU experiment, the FU damage was analyzed thoroughly by evaluating the number of FUs moved as well as by measuring the uncovered area ratio after each wave attack, and the stability number was also estimated.

The stability of the FUs used in these experiments could not be compared with the stability of the FUs in previous researches because of the new FU damage definition. In the previous studies, the FU damage was estimated by examining the FUs movement. Although the number of FUs which moved from its initial position due to wave attacks increased in some experimental cases, the FUs still protected the rubble mound surface without major damage. Therefore, defining the FU damage mechanism by considering "uncovered area" would be beneficial.

The experimental results in this experimental study could be summarized as follows.

From the first experiments, FU-A3/B2 type and FU-A2 type were the most effective

104

FU structure types in hydraulic stability on the rubble mound. It can be concluded that the stability of an S-type FU as an armor unit on rubble mound structure changes depending on the volume ratio and the constraint degree.

Regarding the FU damage by comparing the average values of uncovered area ratios, for (1.0 sec) short period waves, A2-type showed better stability than A3/B2-type within the wave height range generated in these tests. However, for (2.0 sec) long wave period cases, most of the FUs moved by sliding and A3/B2-type was more stable than A2-type. In the cases of 1.5-sec wave period similar to the 1.0-sec cases, A2-type was better than A3/B2-type in stability, although the first run and second run of A3/B2-type resulted in significantly different DR_U.

Generally, the FUs' damage rate was severe when they were attacked by long period waves. In comparison, a slight increase in DR_U was observed, but DR_M increased considerably with longer wave periods. Moreover, the FU models below the shoreline were mostly damaged during the wave attack.

5.2 CONCLUSIONS OF CHAPTER 4

The 2D numerical models for reproducing the FU deformation on the surface of rubble mound under regular waves were proposed in this study. The study focused only on the numerical FU models, and thus modelled the rubble mound with fixed circular particles. The movements of the numerical FU models under wave action were investigated using CS2D and DEM separately. The governing equations for the estimation of the FU model movement were achieved by adding a parallel bond model to the typical DEM model widely used for estimation of rubble mound deformation.

This 2D numerical model was capable of simulating the flexible deformation of the experimental FU models in general. Model-I representing N-type FU model, followed the deformation patterns of the experimental FU models in some way. Model-II (S-type FU model) was more stable than the Model-I (N-type FU model) in the numerical results similar to the experimental finding.

The model input parameters for the DEM calculation were optimized according to the experimental observations, relevant researches, material properties available and computation

time, however these parameters need to be calibrated effectively and need to be validated adequately. The wave train data resulted from the CS2D was sufficiently similar to the experimental waves. The applied wave forces in these simulations were evaluated using Morison-type equation, however these wave forces had not been validated yet.

5.3 FINAL REMARKS

According to the experimental results from Chapter 3, the stability of a S-type FU model varies depending on its volume ratio (of bag/stuffing stones) and constraining rope length. However, there has been no theoretical formula to estimate the volume ratio (of bag/stuffing stones) and constraining rope length of the FU. Therefore, future research should address an applicable definition for these parameters of the FUs and should identify optimal values by taking account of the elongation properties of the fiber as well as of the advantages and disadvantages of high and low values of the volume ratio and constraining rope length.

In order to assess the reliability of these numerical models to validate with the experiments, the models still need to be modified such as building up with particles having non-uniform diameters and the models have to be studied under various wave conditions taking account of fluid-structure interaction based on the efficiency of calculation time.

REFERENCES

Akiyama, S, Ikeya, T, Kondo, H, Takahashi, S, Ishikawa, Y (2001). "The Stability of the Mild Slope Revetment Armored by Filter-Units against Wave Attack," Proc Civil Eng in the Ocean, Vol. 17, 405-410, https://doi.org/10.2208/prooe.17.405 (in Japanese).

Araki, S, Nagatani, E, Deguchi, I (2007). "Stability of Wave Dissipating Blocks as Armor Units for Low Crested Breakwater," Asian and Pacific Coasts, pp. 1539-1548.

Araki, S, Fujiwara, Y, Miyazaki, T, Deguchi, I (2001). "Numerical Calculation on Deformations of Submerged Breakwaters with Discrete Element Method," Asian and Pacific Coastal Eng, China, 630-639.

Araki, S, Kotake, Y, Kanazawa, T, Matsumura, A, Deguchi, I (2002). "Development of Numerical Simulation Method for Predicting Deformation of Rubble Mound Seawall with VOF Method and DEM," Proc 28th Int Conf on Coastal Eng, Cardiff, Wales, 1485-1497.

Araki, S, Deguchi, I (2011). "Numerical Simulation on Displacement of Armor Block on Submerged Breakwater with 3-dimensional DEM," Proc 21st Int Ocean and Polar Eng Conf, ISOPE, Maui, Hawaii, USA, 1152-1157.

Burcharth, H.F, Lin, Z (1993-1995). "Rubble Mound Breakwater Failure Modes," Hydraulic Engineering Report.

CDIT (Coastal Development Institute of Technology) (2001). "Research and development of numerical wave channel (CADMAS-SURF)," Coastal Development of Institute of Technology, CDIT Library. No. 12 (in Japanese).

Coastal Engineering Manual (CEM), 2002, EM 1110-2-1100. U.S Army Engineer Waterways Experiment Station, U.S. Government Printing Office, Washington, DC., (6 volumes).

Cundall, P. A. and Strack, O. D. L. (1979). "A Discrete Numerical Model for Granular Assemblies," Géotechnique 29, No. 1, 47-65.

Ertas, B, Topal, T (2008). "Quality and durability assessments of the armourstones for two

rubble mound breakwaters," Environ Geol, 53, 1235-1247.

Fukumizu, K, Sakai, D, Kanazawa, T, Araki, S (2018). "Development of Effective Technique on Rubble Mound Seawall in Artificial Island under Construction," Proc 28th Int Ocean and Polar Eng Conf, Sapporo, Japan, 1197-1202.

Goda, Y. and Suzuki, Y. (1976). "Estimation of Incident and Reflected Waves in Random Wave Experiments," Proc 15th Int Conf on Coastal Eng, ASCE, 828-845.

Isobe, M. (2013). "Evolution of Basic Equations for Nearshore Wave Field," Proc. Jpn. Acad., Ser. B 89, 34-50, doi: 10.2183/pjab.89.34.

Itoh, K, Higuchi, Y, Toue, T, Katsui, H (2002). "Numerical Simulation of Deformation of Rubble Structures by DEM and VOF," Proc 12th Int Offshore and Polar Eng Conf, ISOPE, Kitakyushu, Japan, 714-721.

Jafari, E, Namin, M.M, Badiei, P (2021). "Numerical Simulation of Wave Interaction with Porous Structures," Applied Ocean Research 108, doi.org/10.1016/j.apor. 2020.102522.

Kamali, B, Hashim, R (2009). "Recent Advances in Stability Formulae and Damage Description of Breakwater Armour Layer," Australian J Basic and Applied Sciences, 2817-2827.

Kiyama, H, Fujimura, H (1983). "Application of Cundall's Discrete Block Method to Gravity Flow Analysis of Rock-like Granular Materials," J Hydraulic, Coastal and Environmental Eng, Vol. 333, 137-146 (in Japanese).

Kubota, S, Matsumoto, A, Hanzawa, M, Shinomura, Y, Oike, N, Ikeya, T, Shimosako, K (2003). "袋型根固め材を用いた混成堤マウンド被覆材の耐波設計法," Proc Coastal Engineering, Vol. 50, 776-780.

Kubota, S, Matsumoto, A, Hanzawa, M, Shinomura, Y, Oike, N, Ikeya, T, Akiyama, S and Shimosako, K (2007). "Stability and Durability of Filter Unit for Protecting Rubble Mound of Composite Breakwater." Coastal Structures 2007, 128-139.

Kyowa – https://www.kyowa-inc.co.jp/en/.

Maeno, S, Michioku, K, Kase, E, Kikuchi, K (2005). "Failure Prediction of a Rubble Mound Weir Using Distinct Element Method," J Hydraulic Eng, Vol. 49, 787-792 (in Japanese).

Maeno, S, Bierawski, LG, Magda, W, Ogawa, M (2009). "VOF-DEM-FEM Combined Model of the Reef Breakwater Collapse," Coastal Eng Journal, Vol. 51, No. 3, 223-242.

Miyata, M, Mustoe, Graham G.W, Nakagawa, M, Sugano, T (2002). "Study of Force Support Systems of Particulate Media using Discrete Element Method," Technical Note of National Institute for Land and Infrastructure Management, No. 33.

Mizutani, N, Shimabukuroi, H and Koyama, H (2007). "Study on a Wave Force Acting on a Filter Unit on Sloping Breakwater and Its Stability," Proc 17th Int Offshore and Polar Eng Conf, ISOPE, 2575-2581.

Mon, A. N, Aoki, S, Koyama, H, Kinoshita, M, Kajiwara, K, Kawamura, H (2020). "An Experimental Study on the Stability of Filter Units on Rubble Mound Breakwater," Proc 30th Int Ocean and Polar Eng Conf, ISOPE, 2757-2763.

Mon, A. N, Aoki, S, Araki, S (2022). "Numerical Investigation of Filter Unit Deformation on Rubble Mound under Wave Action," Proc 32nd Int Ocean and Polar Eng Conf, ISOPE, 2790-2797.

Muttray, M, Reedijk, B (2008). "Design of Concrete Armour Layers," Hansa Int Maritime J, vol 6, 111-118.

Nakamura, T, Mizutani, N, Shinoda, Y, Koyama, H (2011). "Three-dimensional Numerical Analysis of Jet-induced Local Scouring in Front of Quay Walls and its Countermeasure using Filter Units," Coastal Eng J, Vol. 53, No. 1, 41-62.

Potyondy, D. O., Cundall, P. A. (2004). "A Bonded-Particle Model for Rock," Int J Rock Mechanics & Mining Sciences, 41, 1329-1364.

Rojek, J, Oñate, E, Labra, C, Kargl, H (2011). "Discrete Element Simulation of Rock Cutting,"

Int J Rock Mechanics & Mining Sciences, 48, 996-1010.

Sadek M. A. (2013). "Modeling Biofibre (Hemp) Processing using the Discrete Element Method (DEM)," Ph.D. thesis, University of Manitoba, Canada.

Saito, Y (2017). "The Stability of Filter Units on a Slope of Composite Breakwater," Thesis of Master Degree, Osaka University, Japan (in Japanese).

Shin, E. C, Kim, S. H, Hakam, A, Istijono, B (2019). "Erosion problems of shore line and counter measurement by various geomaterials," MATEC Web of Conferences 265, 01010, doi.org/10.1051/matecconf/201926501010.

Shore Protection Manual (1984), Vol. II, No. 7, pp. 202-244

Sigurdur, S, Van der Meer, J (2017). "Armourstone for Berm Breakwaters," Coasts, Marine Structures and Breakwaters, 917-927.

Suzuki, T (2011). "Wave Dissipation over Vegetation Fields," Ph.D. thesis, Delft University of Technology.

Van der Meer, JW (1987). "Stability of Breakwater Armour Layers – Design Formulae," Coastal Engineering, Vol. 11, pp. 219-239.

Yoshimi Goda, Random Seas and Design of Maritime Structures (1985), Chapter 2, pp. 11-39.